

Downloaded from https://academic.oup.com/mnras/article-abstract/478/3/2851/4995927 by MIT Libraries user on 17 July 2019

Simulating galactic dust grain evolution on a moving mesh

Ryan McKinnon,^{1*} Mark Vogelsberger,¹† Paul Torrey,¹‡ Federico Marinacci¹ and Rahul Kannan^{1,2}§

¹Department of Physics and Kavli Institute for Astrophysics and Space Research, Massachusetts Institute of Technology, Cambridge, MA 02139, USA

Accepted 2018 May 10. Received 2018 May 9; in original form 2018 March 6

ABSTRACT

Interstellar dust is an important component of the galactic ecosystem, playing a key role in multiple galaxy formation processes. We present a novel numerical framework for the dynamics and size evolution of dust grains implemented in the moving-mesh hydrodynamics code AREPO suited for cosmological galaxy formation simulations. We employ a particle-based method for dust subject to dynamical forces including drag and gravity. The drag force is implemented using a second-order semi-implicit integrator and validated using several dusthydrodynamical test problems. Each dust particle has a grain-size distribution, describing the local abundance of grains of different sizes. The grain-size distribution is discretized with a second-order piecewise linear method and evolves in time according to various dust physical processes, including accretion, sputtering, shattering, and coagulation. We present a novel scheme for stochastically forming dust during stellar evolution and new methods for sub-cycling of dust physics time-steps. Using this model, we simulate an isolated disc galaxy to study the impact of dust physical processes that shape the interstellar grain-size distribution. We demonstrate, for example, how dust shattering shifts the grain-size distribution to smaller sizes, resulting in a significant rise of radiation extinction from optical to nearultraviolet wavelengths. Our framework for simulating dust and gas mixtures can readily be extended to account for other dynamical processes relevant in galaxy formation, like magnetohydrodynamics, radiation pressure, and thermochemical processes.

Key words: methods: numerical – dust, extinction – galaxies: evolution – galaxies: ISM.

1 INTRODUCTION

Interstellar dust is a crucial ingredient for the formation and evolution of galaxies, which is produced through condensation of metals expelled into the interstellar medium (ISM) by supernovae (SNe) and stellar winds. About 30–50 per cent of the metals condense into the dust component (Draine et al. 2007). Within the ISM dust plays an important role for multiple physical processes. For example, dust grains provide a source of opacity to radiation from sources like active galactic nuclei (AGNs) and massive stars. Radiation pressure acting on dust grains can inject momentum in the ISM and help drive galactic winds (Murray, Quataert & Thompson 2005; Novak, Ostriker & Ciotti 2012; Zahid et al. 2013; Ishibashi & Fabian 2015; Thompson et al. 2015). Dust grain surfaces also aid the formation of molecular hydrogen (Hollenbach & Salpeter 1971;

Cazaux & Tielens 2004) and contribute to photoelectric heating of gas (Bakes & Tielens 1994; Weingartner & Draine 2001b), which both affect star formation in galaxies. Dust grains can also develop electric charge (Feuerbacher, Willis & Fitton 1973; Burke & Silk 1974; Draine & Sutin 1987; Weingartner & Draine 2001b) and are therefore affected by magnetic fields, which alters the dynamics of dust in a turbulent ISM (Lazarian & Yan 2002; Yan, Lazarian & Draine 2004).

Besides influencing interstellar chemistry and galaxy physics, importantly dust also affects the detectability and observed properties of galaxies. Dust grains absorb ultraviolet (UV) light and re-emit the radiation at infrared (IR) wavelengths (Draine & Lee 1984; Mathis 1990; Tielens 2005). Especially at high redshifts, where many surveys are executed in the UV rest frame, the measured properties of galaxies critically depend on dust extinction. Dust has such a strong effect on galaxy properties despite the dust-to-gas ratio in galaxies being a few per cent at most (Draine et al. 2007; Rémy-Ruyer et al. 2014). Emission from dust is an important foreground not only for observation of galaxies but also for the cosmic microwave background (Planck Collaboration XI 2014).

²Harvard-Smithsonian Center for Astrophysics, Cambridge, MA 02138, USA

^{*} E-mail: ryanmck@mit.edu

[†] Alfred P. Sloan Fellow.

[#] Hubble Fellow.

[§] Einstein Fellow.

2852 R. McKinnon et al.

Over the last decade, observations from *Herschel* (Pilbratt et al. 2010) have yielded several dust scaling relations tying dust to fundamental ISM properties. For example, there are observed relations between dust mass and gas mass (Corbelli et al. 2012), dust-to-stellar mass ratio and gas fraction (Cortese et al. 2012), and dust-to-stellar flux and mass ratios (Skibba et al. 2011). Data at high redshift is less abundant, but dust has recently been detected in reionization-era galaxies using the Very Large Telescope and the Atacama Large Millimetre Array (Watson et al. 2015; Laporte et al. 2017), challenging models to explain the production of dust at such early times. The importance of addressing high-redshift dust is likely to increase, given the upcoming *James Webb Space Telescope* mission and its capability to witness the formation of galaxies.

Studying the abundance, distribution, and impact of dust in galaxies requires detailed models that are capable of evolving the dust population of a galaxy along with a plethora of other galaxy formation processes. The specific impact of dust can only be quantified by understanding its spatial and grain-size distribution. This grain-size distribution evolves over time within a galaxy. Dust is produced as stars return metals to the ISM (Todini & Ferrara 2001; Nozawa et al. 2003; Ferrarotti & Gail 2006; Bianchi & Schneider 2007; Zhukovska, Gail & Trieloff 2008; Schneider et al. 2014), setting the initial size distribution for a population of dust grains. The grainsize distribution is then subject to processes that conserve grain number but grow or destroy dust mass. For example, grain sizes grow through accretion of gas-phase metals (Liffman & Clayton 1989; Draine 1990; Dwek 1998; Michałowski et al. 2010; Asano et al. 2013a) but shrink through sputtering (Ostriker & Silk 1973; Burke & Silk 1974; Barlow 1978; Draine & Salpeter 1979; Dwek & Arendt 1992; Tielens et al. 1994) and SN shocks (Nozawa, Kozasa & Habe 2006; Bianchi & Schneider 2007; Nozawa et al. 2007). Other physical processes conserve total dust mass but shape the interstellar size distribution by increasing or decreasing the number of grains: these include dust-dust collisional processes like shattering (O'Donnell & Mathis 1997; Hirashita & Yan 2009; Asano et al. 2013b; Mattsson 2016) and coagulation (Chokshi, Tielens & Hollenbach 1993; Jones, Tielens & Hollenbach 1996; Dominik & Tielens 1997; Hirashita & Yan 2009; Mattsson 2016).

Without a detailed knowledge of the grain-size distribution and the overall arrangement of dust in galaxies, the modelling of dust physical processes remains uncertain. Studying, for example, the interplay of radiation and dust as a feedback mechanism within galaxies requires very detailed knowledge about both the radiation fields and dust content. Simplified feedback prescriptions motivated by radiation pressure coupling to dust grains have been included in some cosmological simulations (e.g. Hopkins et al. 2014; Roškar et al. 2014; Agertz & Kravtsov 2015). However, none of these studies self-consistently model either the radiation field or the dust content. Other studies based on radiation-hydrodynamic simulations improve on those by coupling self-consistent radiation fields to dust but without evolving the dust component self-consistently (e.g. Rosdahl et al. 2015; Costa et al. 2018). Overall, most modern cosmological simulations of large-scale structure (Vogelsberger et al. 2014a,b; Schaye et al. 2015; Khandai et al. 2015) do not directly treat dust within galaxies, despite analysing statistics like the mass-metallicity relation (Torrey et al. 2017, 2018; De Rossi et al. 2017) and cluster metal distribution (Vogelsberger et al. 2018) that could be affected by depletion of metals onto dust. It is therefore highly desirable to have a self-consistent dust model coupled to a comprehensive galaxy formation model in combination with radiation-hydrodynamics to capture the impact of dust on galaxy formation more reliably.

Various numerical models have been developed to evolve the grain-size distribution of galaxies in time (e.g. Liffman & Clayton 1989; O'Donnell & Mathis 1997; Asano et al. 2013b; Hirashita et al. 2015). These models suggest, for example, that changes in the grain-size distribution can strongly affect the overall dust mass. For instance, the process of shattering may temporarily conserve dust mass but, by shifting grains to smaller sizes and increasing the total grain surface area, subsequently leads to rapid increases in dust mass through accretion (Asano et al. 2013b). However, these models are often 'one zone' in nature and focus only on the total size distribution, ignoring dust and gas dynamics because they lack spatial resolution within a galaxy. While many of these previous models are idealized in nature, recent galaxy formation simulations are beginning to evolve dust physics in more detail. These simulations attempt to predict the distribution of dust mass within and around galaxies, include the dynamical forces that impact dust motion, and model the processes that shape the grain-size distribution. Initial attempts have been made to track dust in non-cosmological smoothed particle hydrodynamic (SPH) simulations using 'live' dust particles that are subject to different dynamics (e.g. drag and radiation pressure) than gas particles (Bekki 2015). However, these simulations assume grains to be of fixed size and thus do not make predictions about the interstellar grain-size distribution. Recent simulations using the moving-mesh code AREPO (Springel 2010) have modelled the formation of dust in a fully cosmological context (McKinnon, Torrey & Vogelsberger 2016; McKinnon et al. 2017), albeit assuming perfect coupling between dust and gas and not tracking the grainsize distribution either. Cosmological simulations by Aoyama et al. (2018) model a simplified grain-size distribution, dividing grains into 'small' and 'large' sizes, but do not account for dynamical forces like drag or radiation pressure. Such cosmological results make predictions for the dust content of a diverse sample of galaxies and the distribution of dust on large scales. So far, no simulation has been able to perform cosmological galaxy formation simulations with a state-of-the-art galaxy formation model combined with a dust model that traces both the spatial distribution and full range of sizes of dust grains.

This paper aims to close this gap by presenting a novel dust framework, modelling aspects of grain dynamics and size evolution and implemented alongside the galaxy formation physics in the moving-mesh hydrodynamics code AREPO. Section 2 describes our implementation of the drag force that couples dust grains to hydrodynamical motion and a series of test problems. In Section 3, we discuss the modelling of the size distribution and evolution of dust grains. Section 4 details our implementation for stochastically producing dust during stellar evolution. Using the dust model, in Section 5 we perform simulations of isolated disc galaxies. Our conclusions are presented in Section 6.

2 DUST DYNAMICS AND DRAG

In this section, we first discuss the dynamics of dust particles as they interact with surrounding gas. Solid dust grains travelling through a gaseous medium experience a drag force that alters their dynamical behaviour (e.g. Baines, Williams & Asebiomo 1965; Draine & Salpeter 1979), and which effectively couples dust dynamics to gas dynamics. The strength of this drag force depends on both gas and grain properties and affects the distribution of dust within the ISM. For example, a grain-size dependent drag force impacts the grain-size distribution that results from SN shocks (e.g. Nozawa et al. 2006).

Various numerical works have studied two-fluid dust and gas mixtures using a particle-based SPH framework (Monaghan & Kocharyan 1995; Monaghan 1997; Laibe & Price 2011, 2012a,b; Bekki 2015; Booth, Sijacki & Clarke 2015; Booth & Clarke 2016; Price et al. 2017). In the limit of a strong drag force, it can be advantageous to adopt a one-fluid approach and solve for the mixture's barycentric motion and dust-to-gas ratio (Barranco 2009; Laibe & Price 2014b, 2014c, 2014a; Price & Laibe 2015; Tricco, Price & Laibe 2017). Drag dynamics have also been studied using gridbased methods (Cuzzi, Dobrovolskis & Champney 1993; Balsara et al. 2009) and hybrid methods that combine grid techniques and particle approaches (Johansen, Klahr & Henning 2006; Balsara et al. 2009; Miniati 2010; Hopkins & Lee 2016). Also, the influence of grain size on drag forces has been explored in many ways. For example, Goodson et al. (2016) evolve dust particles of different grain sizes in an expanding Sedov-Taylor blast wave using a drag force and study the loss of grain mass due to sputtering. Other simulations treating drag adopt one fixed grain size (Saito 2002; Saito, Marumoto & Takayama 2003; Miniati 2010; Laibe & Price 2012a: Hopkins & Lee 2016). Newer work accounts for drag acting on multiple dust phases simultaneously when following barycentric motion in the one-fluid approach (Hutchison, Price & Laibe 2018). Other models couple drag force strength to an evolving grain-size distribution in idealized SN studies (Bocchio et al. 2016).

In our work, we model dust with a particle-based framework that exists alongside moving-mesh hydrodynamical calculations. In AREPO (Springel 2010), a finite-volume scheme is used to solve hydrodynamics on a mesh generated by a Voronoi tessellation of space and allowed to move with the local fluid velocity. The mesh can consist of irregularly shaped gas cells and is (de-)refined so that gas cells have roughly equal mass (Vogelsberger et al. 2012).

We could treat dust as a property of each gas cell and model dust dynamics by transferring dust across cell interfaces. However, while gas exists throughout the computational domain, dust might only exist in more localized regions. Thus, it is advantageous to model dust using particles representing ensembles of individual dust grains, with particle motion unconstrained by mesh geometry. This parallels the treatment of collisionless star or black hole particles in AREPO (e.g. Vogelsberger et al. 2013). The formulation for drag below assumes dust is treated in this particle-based manner.

2.1 Drag force calculation

Our drag implementation follows the standard approach taken by Booth et al. (2015) and Hopkins & Lee (2016). The acceleration of a dust particle of mass m_d is given by

$$\frac{\mathrm{d}\boldsymbol{v}_{\mathrm{d}}}{\mathrm{d}t} = -\frac{K_{\mathrm{s}}(\boldsymbol{v}_{\mathrm{d}} - \boldsymbol{v}_{\mathrm{g}})}{m_{\mathrm{d}}} + \boldsymbol{a}_{\mathrm{d,ext}},\tag{1}$$

where K_s is a drag coefficient determined below, v_d and v_g are the dust and gas velocity, respectively, and $a_{d, ext}$ denotes external sources of acceleration (e.g. gravity, radiation pressure, or magnetic fields), while the backreaction on the gas is given by

$$\frac{\mathrm{d}\boldsymbol{v}_{\mathrm{g}}}{\mathrm{d}t} = -\frac{\nabla P}{\rho_{\mathrm{g}}} + \frac{\rho_{\mathrm{d}}K_{\mathrm{s}}(\boldsymbol{v}_{\mathrm{d}} - \boldsymbol{v}_{\mathrm{g}})}{\rho_{\mathrm{g}}m_{\mathrm{d}}} + \boldsymbol{a}_{\mathrm{g,ext}},\tag{2}$$

for gas pressure P, dust and gas densities ρ_d and ρ_g , respectively, and external gas acceleration $a_{g,\text{ext}}$. We assume the dust is pressureless. The drag force can be written in terms of relative velocity as

$$\frac{\mathrm{d}(\mathbf{v}_{\mathrm{d}} - \mathbf{v}_{\mathrm{g}})}{\mathrm{d}t} = -\frac{\mathbf{v}_{\mathrm{d}} - \mathbf{v}_{\mathrm{g}}}{t_{\mathrm{s}}},\tag{3}$$

using the stopping time-scale

$$t_{\rm s} = \frac{m_{\rm d}\rho_{\rm g}}{K_{\rm s}(\rho_{\rm g} + \rho_{\rm d})}.\tag{4}$$

Shorter stopping time-scales correspond to the high-drag regime in which relative velocities quickly decay. In this work, we focus on collisional drag and neglect Coulomb drag resulting from grain charge.

To lowest order, the aerodynamic drag force has magnitude

$$F_{\rm D} = \frac{1}{2} C_{\rm D} \pi a^2 \rho_{\rm g} |\boldsymbol{v}_{\rm d} - \boldsymbol{v}_{\rm g}|^2, \tag{5}$$

the product of a drag parameter $C_{\rm D}$, grain cross-section, and ram pressure. A typical interstellar grain of radius a satisfies $a < 9\lambda/4$, where λ is the gas mean free path. This corresponds to the Epstein drag regime (Epstein 1924; Weidenschilling 1977; Stepinski & Valageas 1996), in which drag effects build up through collisions with individual gas atoms. This is in contrast to the Stokes limit, $a > 9\lambda/4$, in which the gas behaves as a fluid and the drag force depends on the Reynolds number of the flow. In the Epstein limit, the drag parameter is given by

$$C_{\rm D} = \frac{16\sqrt{2}c_{\rm s}}{3\sqrt{\pi\gamma}|\boldsymbol{v}_{\rm d} - \boldsymbol{v}_{\rm g}|},\tag{6}$$

where c_s is the local sound speed and γ is the adiabatic index. In this regime, the drag force is therefore linear in the relative velocity. The drag coefficient entering into the acceleration equations is

$$K_{\rm s} = \frac{1}{2} C_{\rm D} \pi a^2 \rho_{\rm g} |\mathbf{v}_{\rm d} - \mathbf{v}_{\rm g}| = \frac{8\sqrt{2\pi}c_{\rm s}a^2 \rho_{\rm g}}{3\sqrt{\gamma}}. \tag{7}$$

Furthermore, for ISM studies with $\rho_d/\rho_g \ll 1$, we can ignore the drag force in the gas equation of motion; i.e. we solve equation (1) for dust motion including the drag force but solve gas motion using equation (2) neglecting the backreaction of dust dynamics on the gas. Inclusion of the backreaction of drag on gas will be necessary in future studies of radiation-driven outflows.

Assuming spherical grains with mass $m_d = 4\pi a^3 \rho_{gr}/3$, this implies a stopping time-scale of

$$t_{\rm s} = \frac{m_{\rm d}}{K_{\rm s}} = \frac{\sqrt{\pi \gamma} a \rho_{\rm gr}}{2\sqrt{2}\rho_{\rm g} c_{\rm s}},\tag{8}$$

where $\rho_{\rm gr}$ is the internal density of a dust grain. The derivation of equation (8) implicitly assumed subsonic relative dust-gas velocities. Supersonic relative motion requires a further correction factor for the stopping time-scale (Kwok 1975; Draine & Salpeter 1979; Paardekooper & Mellema 2006; Price et al. 2017), which is approximated by the following fit

$$t_{\rm s} = \frac{\sqrt{\pi \gamma} a \rho_{\rm gr}}{2\sqrt{2}\rho_{\rm g} c_{\rm s}} \left(1 + \frac{9\pi}{128} \left| \frac{\mathbf{v}_{\rm d} - \mathbf{v}_{\rm g}}{c_{\rm s}} \right|^2 \right)^{-1/2}. \tag{9}$$

To remain consistent with previous works, we calculate all stopping time-scales using equation (9) and take the internal density to be $\rho_{\rm gr} \approx 2.4\,{\rm g\,cm^{-3}}$ (Draine 2003). A stopping time-scale of this form is valid for supersonic dust-gas relative velocity and has been used in turbulent giant molecular cloud simulations reaching Mach numbers $\mathcal{M} > 10$ (Hopkins & Lee 2016; Lee, Hopkins & Squire 2017). We note that in the subsonic limit, this reduces to the form of stopping time-scale from equation (8) above, similar to that used in Booth et al. (2015).

Since we apply drag acceleration only to dust in the $\rho_{\rm d}/\rho_{\rm g}\ll 1$ limit, we only need to interpolate $\rho_{\rm g},\,{\bf v}_{\rm g},$ and $c_{\rm s}$ to the position of

a dust particle in order to calculate its stopping time-scale. To this end, we perform a kernel-smoothing around a given dust particle at position $r_{\rm d}$. We first iteratively solve for its smoothing length $h_{\rm d}$ using

$$N_{\rm ngb} = \frac{4\pi h_{\rm d}^3}{3} \sum_{i}^{\rm gas} W(|{\bm r}_i - {\bm r}_{\rm d}|, h_{\rm d}),$$
 (10)

where N_{ngb} is the desired number of gas neighbours and the cubic spline kernel is given by

$$W(r,h) = \frac{8}{\pi h^3} \begin{cases} 1 - 6\left(\frac{r}{h}\right)^2 + 6\left(\frac{r}{h}\right)^3, & 0 \le \frac{r}{h} \le \frac{1}{2}, \\ 2\left(1 - \frac{r}{h}\right)^3, & \frac{1}{2} < \frac{r}{h} \le 1, \\ 0, & \frac{r}{h} > 1. \end{cases}$$
(11)

Then we can estimate

$$\rho_{g}(\mathbf{r}_{d}) = \sum_{i=1}^{N_{\text{ngb}}} m_{i} \operatorname{W}(|\mathbf{r}_{i} - \mathbf{r}_{d}|, h_{d}), \tag{12}$$

and

$$\mathbf{v}_{g}(\mathbf{r}_{d}) = \frac{\sum_{i=1}^{N_{ngb}} m_{i} \mathbf{v}_{i} \, \mathbf{W}(|\mathbf{r}_{i} - \mathbf{r}_{d}|, h_{d})}{\sum_{i=1}^{N_{ngb}} m_{i} \, \mathbf{W}(|\mathbf{r}_{i} - \mathbf{r}_{d}|, h_{d})}, \tag{13}$$

which amounts to a mass-weighted gas velocity calculation. Throughout our work, we perform all kernel smoothings in a similar manner. The kernel framework above is written for three spatial dimensions but can also be generalized to one or two dimensions.

2.2 Time integration

An explicit drag integrator requires us to resolve $\Delta t < t_s$ for dust particles, meaning drag time-steps may be more restrictive than hydrodynamical or gravitational time-steps. To get an idea of typical stopping time-scales, we can use equation (9) to write

$$t_{\rm s} \approx 6.2 \,\mathrm{Myr} \, \left(\frac{a}{0.1 \,\mu\mathrm{m}}\right) \left(\frac{\rho_{\rm gr}}{2.4 \,\mathrm{g\,cm^{-3}}}\right) \\ \times \left(\frac{\rho_{\rm g}}{10^{-24} \,\mathrm{g\,cm^{-3}}}\right)^{-1} \left(\frac{c_{\rm s}}{1 \,\mathrm{km\,s^{-1}}}\right)^{-1}, \tag{14}$$

where we assume $\gamma=5/3$ and neglect the higher-order stopping time-scale correction for supersonic relative gas-dust velocity. As noted by Laibe & Price (2012a), resolving stopping time-scales is most prohibitive when gas and dust are highly coupled and thus show little relative motion. In essence, we require high temporal resolution only to find that dust and gas move as one. Worse yet, if dust is not treated in the test-particle limit (where we assumed $\rho_{\rm d}/\rho_{\rm g}\ll 1$) and backreaction on the gas is included, a high spatial resolution is also needed to avoid artificial overdissipation of kinetic energy when dust-gas dephasing is not resolved (Laibe & Price 2012a).

One alternative approach eschews the two-fluid formalism in favour of a one-fluid method following the gas-dust barycentre (Laibe & Price 2014b, 2014c). In the limit of small dust-to-gas ratio, this simply treats dust as a passive scalar perfectly coupled to gas motion. Another alternative approach, valid in the test-particle limit, maintains the two-fluid formalism from Section 2 and employs semi-implicit integrators to avoid the need for prohibitively small drag time-steps. Here we therefore follow the semi-implicit time-stepping approaches detailed in previous works (Monaghan 1997; Laibe & Price 2012b; Lorén-Aguilar & Bate 2014; Booth et al. 2015; Lorén-Aguilar & Bate 2015) that make use of the analytical solution of equation (3) in the case of constant stopping time-scale.

In practice, we employ the $\rho_{\rm d}/\rho_{\rm g}\ll 1$ limit of Lorén-Aguilar & Bate (2015), whose semi-implicit, split-update method is well-suited to the time integration routine in AREPO. The method presented in Lorén-Aguilar & Bate (2015) fixes the limitations of the method in Lorén-Aguilar & Bate (2014) pointed out by Booth et al. (2015), namely the incorrect behaviour of relative velocity in cases of a net dust-gas relative acceleration from external sources. We note that equation (17) in Lorén-Aguilar & Bate (2015), the basis for our drag kicks, can be recast in the form of equation (16) in Booth et al. (2015), which is shown to be a second-order scheme. However, Booth et al. (2015) suggest that a simpler first-order scheme may be acceptable for general use. We refer the reader to Lorén-Aguilar & Bate (2014) for discussion on the stability of semi-implicit drag integrators.

Our semi-implicit second-order time integration is implemented in the following way. Suppose the system is at time t and a dust particle's velocity is being updated over time-step Δt . Let $\tilde{v}_{\rm d}(t+\Delta t)$ and $\tilde{v}_{\rm g}(t+\Delta t)$ denote the dust particle's velocity and SPH-averaged gas velocity at time $t+\Delta t$ after non-drag (e.g. gravity) kicks are applied, but before drag acts on velocities. Then, we update the dust particle's velocity to

$$\mathbf{v}_{d}(t + \Delta t) = \tilde{\mathbf{v}}_{d}(t + \Delta t) - \xi \left[\tilde{\mathbf{v}}_{d}(t + \Delta t) - \tilde{\mathbf{v}}_{g}(t + \Delta t) \right] + \left[(\Delta t + t_{s})\xi - \Delta t \right] \left[\mathbf{a}_{d,\text{ext}}(t) - \mathbf{a}_{g,\text{ext}}(t) + \frac{\nabla P}{\rho_{g}} \right], (15)$$

where we define $\xi \equiv 1 - \exp{(-\Delta t/t_s)}$. To maintain consistency with equation (2), our notation differs slightly from that used in Lorén-Aguilar & Bate (2015), where $-\nabla P/\rho_g$ is folded into $a_{g,\text{ext}}$. While we adopt this semi-implicit approach and use it in most cases, we also implement an explicit first-order time-stepping framework for comparison purposes.

Dust particles are dynamically assigned individual time-steps in the following manner. For each dust particle, we first calculate the minimum hydrodynamical time-step for gas cells within the smoothing kernel radius h_d , which we denote $\Delta t_{g,ngb}$. Next, we determine a Courant-Friedrichs-Lewy (CFL) type time-step using

$$\Delta t_{\text{CFL}} \equiv \frac{C_{\text{CFL}} h_{\text{d}}}{\sqrt{c_{\text{s}}^2 + |\mathbf{v}_{\text{g}} - \mathbf{v}_{\text{d}}|^2}},\tag{16}$$

where $C_{\text{CFL}} \sim 0.3$ and c_s is the kernel-averaged gas sound speed. In the case of the explicit integrator, we also calculate a time-step using $\Delta t_{\text{stop}} \equiv \beta_{\text{stop}} t_s$, where β_{stop} controls what fraction of the stopping time-scale must be resolved. Typically, β_{stop} is a factor of order 0.1, although in practice we do not use the explicit drag integrator beyond a simple test problem. Using these time-step values, the dust particle time-step is chosen to satisfy all of these constraints via

$$\Delta t_{\rm d} = \min(\Delta t_{\rm g,ngb}, \Delta t_{\rm CFL}, \Delta t_{\rm stop}), \tag{17}$$

where the final term involving $\Delta t_{\rm stop}$ only applies if using an explicit integrator (i.e. the term is not included when using equation 15). In addition, gravitational time-steps for dust particles are calculated in the same manner as for dark matter, stars, and other collisionless particles in AREPO.

In the following, we will present test problems to demonstrate the performance of our dust integrator.

2.3 Drag in uniform gas flow

We start with a first simple test by simulating a periodic, threedimensional box of volume $(1 \text{ kpc})^3$ using 16^3 gas cells and 16^3 dust particles, arranged in a body-centred configuration. Dust is

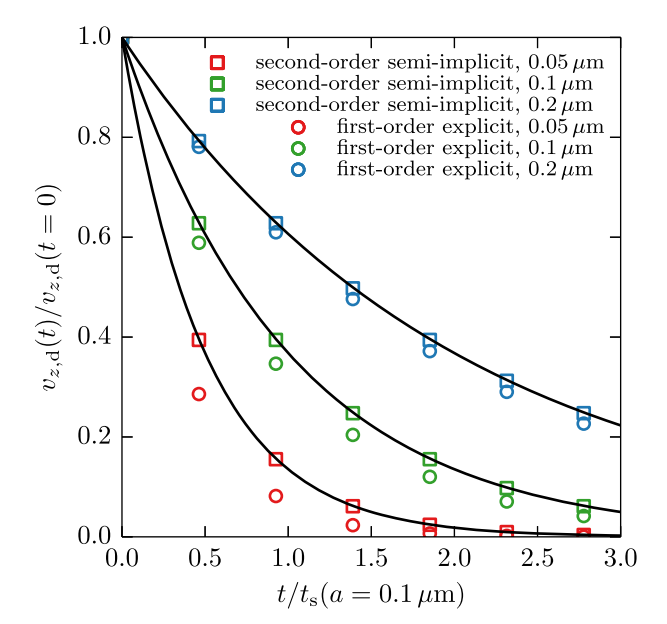


Figure 1. Mean velocity evolution for dust particles travelling with initial velocity $v_{z,d}(t=0)=1\,\mathrm{km\,s^{-1}}$ in a box where gas is at rest. Circles denote velocities calculated using the explicit first-order integrator for fixed grain sizes $a=0.05,\,0.1,\,\mathrm{and}\,0.2\,\mu\mathrm{m}$, while squares indicate velocities from the semi-implicit method of equation (15). Black lines show analytic results. Times are normalized to the stopping time-scale for the run with $a=0.1\,\mu\mathrm{m}$. For the explicit method, we require $\Delta t < t_{\mathrm{s}}$, while the semi-implicit method can adopt time-steps independent of stopping time-scale. The accuracy of the explicit method could be improved by adopting smaller time-steps at the expense of computational cost.

given an initial velocity $v_{\rm d}=1\,{\rm km\,s^{-1}}\,\hat{z}$, and gas has uniform density $\rho_{\rm g}=2\times10^7\,{\rm M_{\odot}\,kpc^{-3}}$, corresponding to an ISM-like number density $n\sim1\,{\rm cm^{-3}}$. The uniform dust density is taken to be $\rho_{\rm d}=\rho_{\rm g}/100$, and grains are assumed to have a fixed radius a. We perform runs with a=0.05,0.1, and $0.2\,{\rm \mu m}$.

We turn off self-gravity, so that only hydrodynamic forces act. Since there is no drag backreaction on gas cells, their velocities remain unchanged as the system evolves. We integrate these dust particles over several stopping times, using the two integrators: the explicit first-order method (requiring $\Delta t < t_{\rm s}$) and the semi-implicit second-order method given by equation (15). Fig. 1 shows the evolution of dust velocity as a function of time. We note again that in general the semi-implicit integrator chooses dust time-steps independent of stopping time-scale, but for this test, we force it to use the same time-steps as the explicit first-order integrator. Both integrators yield exponential velocity decay, but the explicit first-order method overdamps the dust velocity when resolving the stopping time-scale. By contrast, the second-order semi-implicit drag integrator offers much better agreement with the analytically calculated expected velocity evolution tracks.

Our initial analysis of the benefits of semi-implicit drag integrators agrees with findings from earlier two-fluid studies (Monaghan 1997; Laibe & Price 2012a,b; Booth et al. 2015). The conclusion of the test in Fig. 1 is *not* that an explicit integrator is unsuitable for gas-dust drag in theory, but rather that high-accuracy solutions may require prohibitively small time-steps. This is especially the case in highly coupled flows, where the stopping time-scale can be much smaller than the hydrodynamical time-scale. We investigate the convergence properties of these integrators in more detail in the following section.

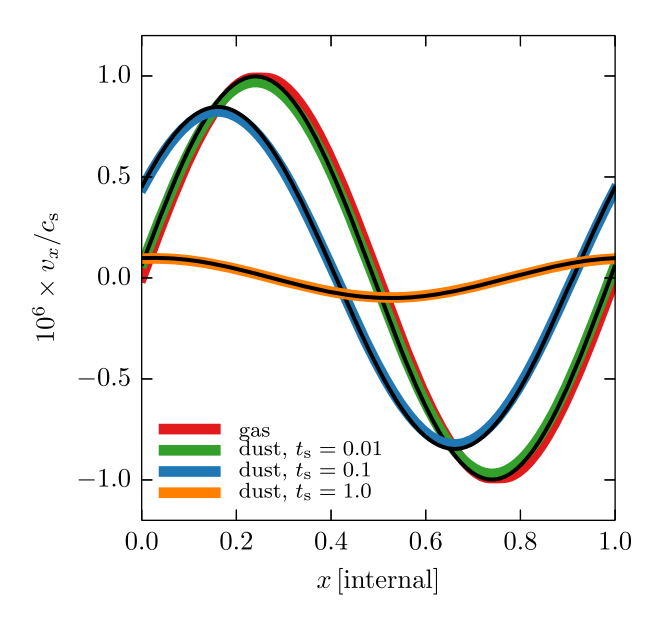


Figure 2. Velocity profiles in the dusty travelling wave test at t = 1 after one wave crossing. Coloured points show velocities for gas (red) and dust using various stopping time-scales: $t_s = 0.01$ (green), $t_s = 0.1$ (blue), and $t_s = 1.0$ (orange). Black lines show numerically integrated dust velocity profiles. Dust most closely follows the gas when the stopping time-scale is short, corresponding to high drag.

2.4 Dusty travelling wave

The propagation of linear sound waves that transport dust is a well-studied test problem (Laibe & Price 2011, 2012a; Booth et al. 2015) that we explore next. We perform the travelling wave test in one dimension, where in internal units the periodic domain has length 1 and sound speed $c_s = 1$. At equilibrium, gas and dust are at rest, with the gas having density $\rho_g = 1$ and adiabatic index $\gamma = 5/3$. To produce a linear wave, we add sinusoidal perturbations to the gas density and velocity with amplitudes $\Delta \rho_g/\rho_g = \Delta v_g/c_s = 10^{-6}$. As this wave propagates, it accelerates the dust via the drag force. We use various fixed stopping time-scales to test our implementation.

Fig. 2 shows the velocity structure of the wave at t=1, after one full period. While the gas wave returns to its original state, the behaviour of the dust is more complex. When the stopping timescale is small ($t_s=0.01$), the drag force acts quickly and produces a dust wave closely mirroring the gas wave. However, when the stopping time-scale is large ($t_s=1.0$), dust is not strongly coupled to the gas and experiences velocity amplitudes roughly one-tenth of the gas velocity. Furthermore, as the drag strength decreases, there is a clear phase offset between the gas and dust waves. A run with medium stopping time-scale ($t_s=0.1$) displays a hybrid of these two limiting cases.

We next study how the test results are affected by changes in time-step. We use the parameter N to indicate how many time-steps fit into one stopping time-scale: that is, we enforce $\Delta t < t_s/N$. In this test, we fix $t_s = 0.1$. To focus strictly on the accuracy of the drag integrator, we do not use kernel smoothing to estimate the local gas velocity in performing drag updates but instead use the known analytic gas solution. As in Fig. 2, we let the wave propagate for one full period. We estimate the error after one period using the L1 norm

$$L1 = \frac{1}{N_{d}} \sum_{i} |v_{i} - v_{d}(x_{i})|, \tag{18}$$

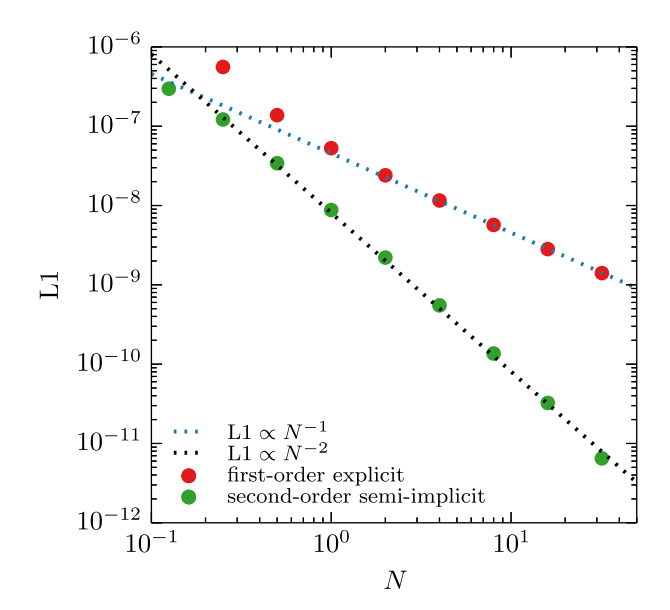


Figure 3. Convergence results for the dusty travelling wave test, plotting L1 error in dust velocity at t = 1 after one gas wave-crossing for a constant stopping time-scale of $t_s = 0.1$. Here, N controls time-step resolution via the constraint $\Delta t < t_s/N$, and we show results for explicit, forward Euler (red) and semi-implicit (green) drag updates. We hard-code the analytic gas velocity when computing dust drag forces to avoid interpolation noise. Dotted lines show first-order (blue) and second-order (black) scalings. The semi-implicit velocity update given by equation (15) produces a second-order drag solver.

where $N_d = 256$ is the number of dust particles, x_i and v_i are the position and velocity of the dust particle i and, following Booth et al. (2015), $v_d(x_i)$ is the dust velocity at t=1 computed using a high-resolution numerical integrator.

Fig. 3 shows the L1 error for dust after one wave-crossing as the fineness of the time-steps (given by the parameter N) is increased. As expected we find that the first-order explicit scheme has an error scaling as N^{-1} , while the second-order semi-implicit method converges faster with an error proportional to N^{-2} . In all subsequent tests and simulations, we only use the second-order semi-implicit scheme.

2.5 Hydrodynamical shock in a dusty medium

Next, we test the dynamics of dust particles in a Sod (1978) shock tube, which has been studied both for high dust-to-gas ratio (Paardekooper & Mellema 2006; Laibe & Price 2012a,b) and in the test-particle limit (Booth et al. 2015).

We use an elongated box of dimensions $1.25 \times 0.15625 \times 0.15625$ in code units, with $512 \times 64 \times 64$ equally spaced gas cells and dust particles initially at rest and arranged in a body-centred lattice with reflective boundary conditions. Following Booth et al. (2015), gas cells have $\rho_{\rm g}=1$ and P=1 for x<0 and $\rho_{\rm g}=0.25$ and P=0.1795 for $x\geq 0$. The adiabatic index is $\gamma=5/3$. The dust-to-gas ratio is set to $\rho_{\rm d}/\rho_{\rm g}=0.01$. As a result of this configuration, gas cells and dust particles across the jump have unequal mass.

Fig. 4 shows the density and velocity profiles obtained in this shock tube at t = 0.2 for two choices of fixed stopping time-scale, $t_s = 0.1$ (low drag) and $t_s = 0.01$ (high drag). Fixing the stopping time-scale enables comparison with analytic dust profiles for particles satisfying x > 0 at t = 0 (see equations (20 and 21) in Booth

et al. 2015). The density of a gas cell is obtained directly from the hydrodynamics solver in AREPO, while we calculate the dust density via kernel smoothing using an equivalent version of equation (12). Smoothing lengths are calculated to ensure dust particles have $N_{\rm ngb} = 64 \pm 8$ neighbours.

Qualitatively, the dust profiles show good agreement with the analytic predictions and are more similar to those of the gas for shorter stopping time-scale. However, while the gas density profiles show two discontinuities, corresponding to the contact discontinuity and shock, the dust density has only one discontinuity. We note that AREPO robustly captures the expected gas dynamics, and this in turn improves the accuracy of our drag calculations. In contrast, the shock test presented in fig. 5 of Booth et al. (2015) displays gas velocity ringing near the contact discontinuity (i.e. gas velocity dispersions of roughly 5–10 per cent of the sound speed). This leads to numerical noise when integrating dust particles, although to some degree this problem is ameliorated by smoothing over the velocities of many gas neighbours. This test demonstrates that accurate dust dynamics in part requires accurate gas dynamics.

2.6 Drag acceleration in an expanding Sedov blast wave

The Sedov blast wave test studies the dynamics of dust in a standard three-dimensional Sedov (1959) blast wave. There exist analytical solutions for the gas dynamics in the purely hydrodynamical case (e.g. Landau & Lifshitz 1959), and these are still valid in the dust test-particle limit.

This dust test has been introduced in Laibe & Price (2012a), and we largely parallel that set-up. We simulate a periodic, cubic volume of unit side length with 128^3 gas cells and dust particles. The initial gas cells are determined by choosing random mesh-generating points and relaxing the mesh using Lloyd's algorithm (Lloyd 1982), while dust particles are superimposed using a Cartesian lattice. In code units, the initially uniform gas and dust densities are $\rho_g = 1$ and $\rho_d = 0.01$, respectively. We inject a total energy E = 1 into the gas cell at the volume centre. For comparison, Laibe & Price (2012a) spreads this blast energy over multiple gas particles using kernel-smoothing. Outside of this blast cell, we assign the gas pressure such that the sound speed $c_s = 2 \times 10^{-5}$. The gas has adiabatic index $\gamma = 5/3$. For this test, we fix the stopping time-scale at $t_s = 0.04$.

We note that our test focuses strictly on grain dynamics and ignores high-temperature sputtering (Ostriker & Silk 1973; Burke & Silk 1974; Barlow 1978; Draine & Salpeter 1979; Dwek & Arendt 1992; Tielens et al. 1994), although hot blast waves are expected to modify the grain-size distribution (Nozawa, Kozasa & Habe 2006; Bianchi & Schneider 2007; Nath, Laskar & Shull 2008; Kozasa et al. 2009; Silvia, Smith & Shull 2010, 2012; Goodson et al. 2016). Evolution in the grain-size distribution would in turn affect the strength of dust-gas drag. The purpose of this test is not to realistically model an SN remnant but to assess grain motion in a well-known hydrodynamical problem.

Fig. 5 shows the resulting density and velocity profiles at t= 0.06 for both gas and dust. We compare against analytic gas profiles predicted by the Sedov solution and dust profiles predicted by numerically integrating the dust drag equation of motion. Here, we see that dust shows qualitatively different features: the density and velocity profiles peak before the radius of the blast wave and do not show discontinuities. Because gas and dust are decoupled and interact only through the drag force, dust lags behind the gas and experiences smaller-amplitude increases in density and velocity. The simulated dust profiles show good agreement with the numerical

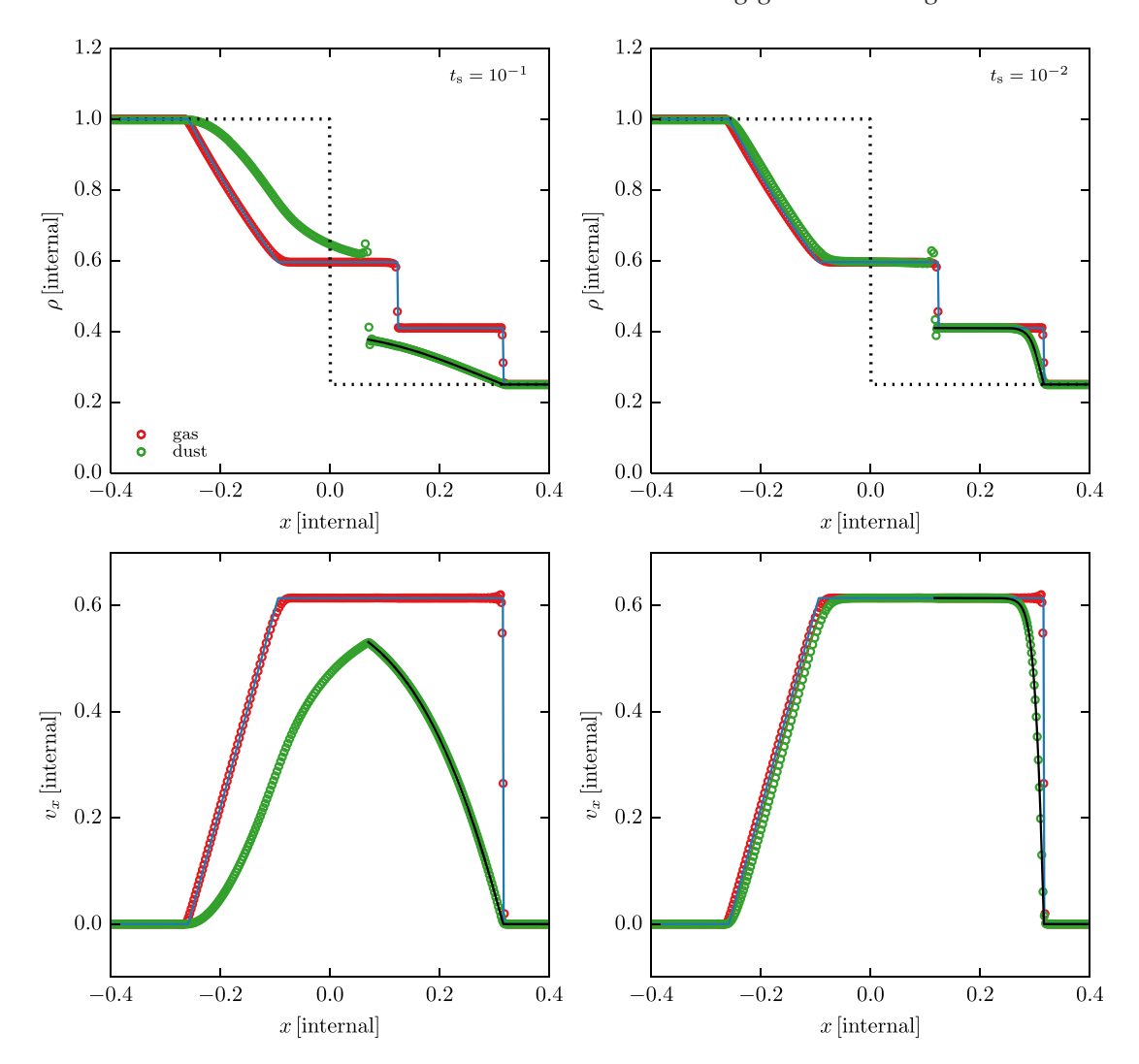


Figure 4. Density (top) and velocity (bottom) profiles for gas (red) and dust (green) in the shock test at t = 0.2, using fixed stopping time-scales $t_s = 0.1$ (left) and $t_s = 0.01$ (right). Solid lines denote analytic profiles for gas (blue) and dust (black), while the dotted line in the top panels marks the initial density jump. The dust density profile is constructed using kernel interpolation at dust particle positions and is multiplied by the overall gas-to-dust ratio to enable comparison with gas density. The hydrodynamic methods from Springel (2010) prevent the spurious gas velocity ringing present in fig. 5 of Booth et al. (2015), leading to reduced noise in the dust velocity profiles. The dust profiles more closely follow the gas profiles in the high-drag case with shorter stopping time-scale.

predictions, although we note that the dust velocity near the blast wave tends to lie above its predicted value, exceeding the peak velocity by about 10 per cent.

Two-dimensional slices of the mesh are shown in Fig. 6. To improve the visibility of the mesh, this figure has been generated from a run using only 64^3 gas cells and dust particles and at t=0.08, when the blast has expanded to fill more of the volume than in Fig. 5. For each gas cell in this two-dimensional slice, we compute the local dust density by kernel interpolation in three dimensions over nearby dust particles, centring the interpolation about the cell centroid. The dust-to-gas ratio is then estimated by dividing the local dust density by the cell's known gas density.

Fig. 5 shows that the dust density increases radially outwards from the blast but peaks before reaching the radius of the blast wave. Because the drag force coupling dust to the hydrodynamical motion takes some time to act, dust appears to chase the expanding blast. This results in a clear negative radial gradient for the dust-to-gas ratio: the dust-to-gas ratio is highest near the centre of the blast, since dust is delayed in expanding outwards, and lowest at the blast

radius, since gas compresses to higher density more rapidly than the lagging dust. Simulations treating dust as perfectly coupled to the hydrodynamical motion would not resolve these dust-to-gas ratio variations.

2.7 Dust falling through gas under gravitational acceleration

Next, we study the dynamics of dust grains subject to an external gravitational acceleration in a gaseous medium in hydrostatic equilibrium (e.g. Monaghan 1997). We generate an equispaced lattice of 128^3 gas cells in a box of length 1 kpc centred on the origin and apply an external gravitational acceleration pointing to the box mid-plane, $\mathbf{g} = -2 \operatorname{sgn}(x) \hat{\mathbf{x}} \operatorname{km}^2 \operatorname{kpc}^{-1} \operatorname{s}^{-2}$, where sgn is the sign function. The gas has adiabatic index $\gamma = 5/3$ and initial density profile $\rho(x) = 10^8 \exp(-|x|/h) \operatorname{M}_{\odot} \operatorname{kpc}^{-3}$, where $h = 0.05 \operatorname{kpc}$ is a scale height. We assume an isothermal gas, and the choices for \mathbf{g} and $\rho(x)$ above determine the gas temperature needed for hydrostatic equilibrium. Thus, the gas has a pressure distribution that is also exponential and a uniform sound speed $c_{\rm s} = \sqrt{\gamma |g|h}$.

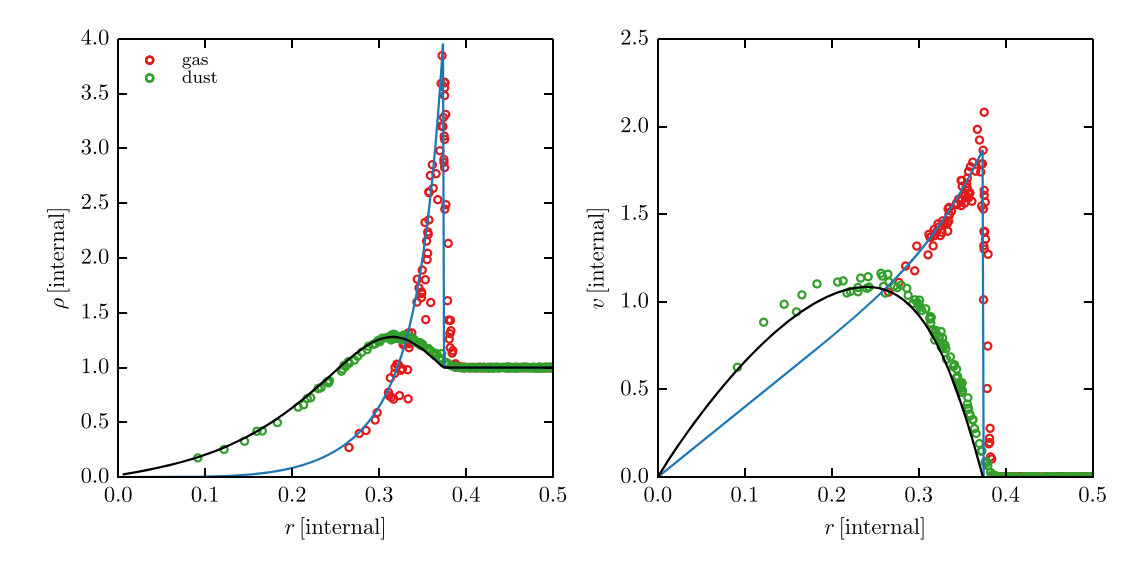


Figure 5. Density (left) and velocity (right) profiles for gas (red) and dust (green) in the Sedov dust test at t = 0.06. We multiply the dust density by the gas-to-dust ratio to compare densities on the same axes. The drag stopping time-scale is fixed to $t_s = 0.04$. Solid blue lines denote analytic gas profiles, and solid black lines indicate dust profiles predicted by numerically integrating the dust drag acceleration using the self-similar Sedov–Taylor solution. We randomly sub-sample gas cells and dust particles to improve readability. Dust lags behind the gas and does not display sharp peaks in density and velocity.

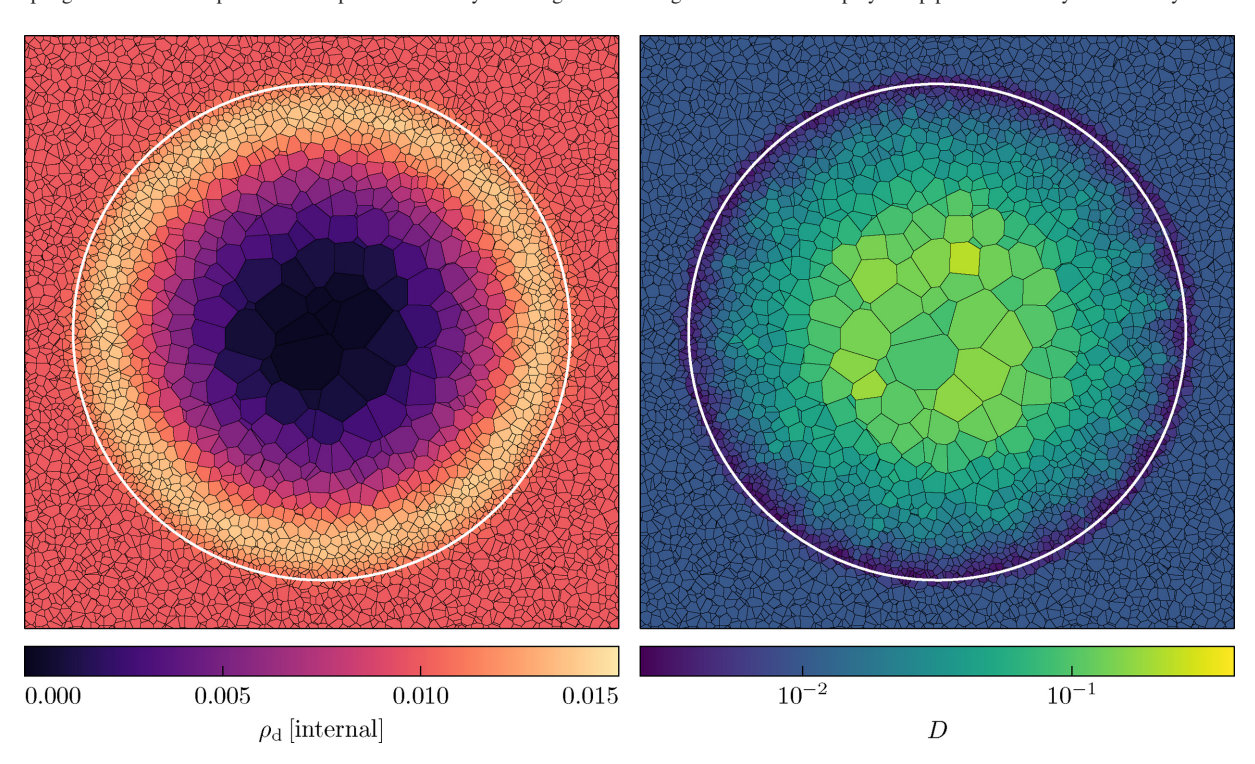


Figure 6. Two-dimensional slices of the mesh structure in the Sedov dust test at t = 0.08, where gas cells are coloured by the local dust density (left) and dust-to-gas ratio (right). These quantities are computed in a kernel-smoothed manner about the centroid of each two-dimensional cell. White circles denote the radius where gas density peaks, computed using the analytic self-similar solution. As in Fig. 5, the stopping time-scale is set to $t_s = 0.04$. Because dust is not perfectly coupled to the hydrodynamical motion, the dust density peaks at a smaller radius than the gas density. Thus, there is a drop in dust-to-gas ratio near the blast radius.

We place a dust particle at position $r=0.45\,\hat{x}$ kpc, such that gravity pushes the dust particle towards the box centre. The dust particle starts with zero initial velocity. We assume a fixed grain radius a, as described below, and an internal grain density $\rho_{\rm gr}=2.4\,{\rm g\,cm^{-3}}$. Note that because the gas density is not uniform, the stopping timescale given by equation (9) varies with position and is smallest near the box centre, where the gas is most dense. We include the velocity-

dependent correction factor in equation (9) in our test, although it does not qualitatively impact our results. Finally, we neglect self-gravity.

While the gas maintains its pressure gradient to counteract the external gravity and remain at rest, the dust particle is accelerated by gravity and begins to move. However, as the dust velocity increases, so too does the strength of the drag force opposing gravity. Fig. 7

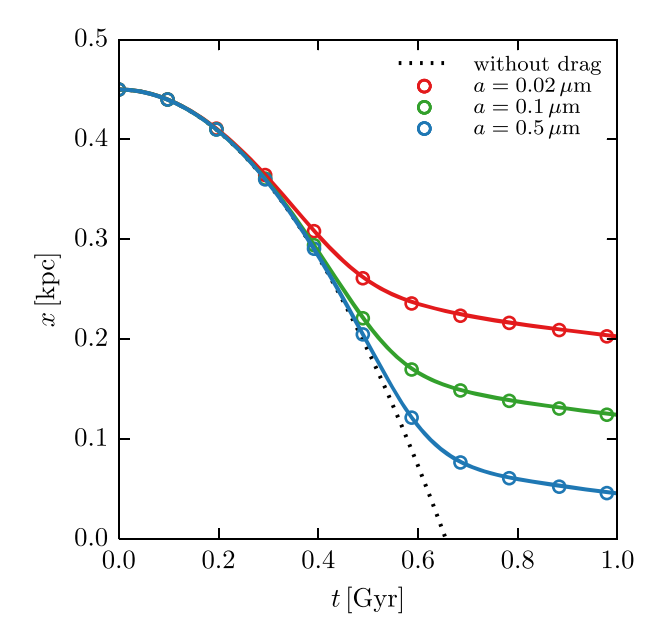


Figure 7. Position as a function of time for dust grains starting at rest in isothermal, hydrostatic gas with constant external gravity $g = -2\hat{x} \,\mathrm{km^2 \,kpc^{-1} \,s^{-2}}$. Coloured circles show simulation results for grains of different radii, while coloured lines show analytic predictions. Grains initially follow the parabolic profiles expected in the drag-free case (dotted black line), but eventually the magnitude of the drag force is sufficient to slow grain motion. Drag acts more quickly for small grains with shorter stopping time-scale.

shows the dust particle's position versus time, for three different choices of grain radius a: 0.5, 1.0, and 2.0 μ m. Initially, the dust particle follows the parabolic trajectory expected for drag-free motion in a uniform gravitational field. However, as the dust particle moves towards x=0 kpc, both its velocity and the local gas density increase. This results in a shorter stopping time-scale and thus a stronger drag acceleration. Around $t\approx0.5$ Gyr, the dust particle deviates from the drag-free motion. As expected, a smaller grain feels the effects of drag more quickly, since stopping time-scale varies linearly with grain radius.

In Fig. 7, we compare our simulation results with predictions obtained by numerically integrating the dust particle's position and velocity using a high-accuracy differential equations solver. The gravitational acceleration is constant, while the drag acceleration depends on the dust velocity and stopping time-scale. We compute the stopping time-scale as a function of position using the analytic gas density profile. Our simulations agree well with these expected profiles.

3 GRAIN-SIZE EVOLUTION

Dust grains injected into the ISM by stars experience a range of physical processes – accretion, sputtering, shattering, and coagulation, among others – that affect their size distribution, as illustrated in Fig. 8. In turn, the grain-size distribution affects the strength of dust-gas drag (e.g. see Section 2), interstellar extinction (e.g. Mathis, Rumpl & Nordsieck 1977; Weingartner & Draine 2001a), and other processes like radiation pressure. Thus, it is important to properly model the evolution of the grain-size distribution when using a two-fluid approach.

Many theoretical and computational dust studies either evolve a grain-size distribution but track only total dust mass (Liffman & Clayton 1989; O'Donnell & Mathis 1997; Hirashita et al. 2015), or evolve dust masses for various chemical elements but assume fixed grain radii (Zhukovska, Gail & Trieloff 2008; Bekki 2015; Popping, Somerville & Galametz 2017; McKinnon et al. 2017). Here, we wish to do both. However, to combine chemical element and grain-size distribution tracking without unwieldy complexity, we make several assumptions.

First, we distinguish between a dust grain (a single, physical object) and a dust particle (an element of our simulation consisting of an ensemble of dust grains). In this work, we always assume grains are spherical, so that a grain with radius a>0 has mass

$$m(a) \equiv \frac{4\pi \rho_{\rm gr} a^3}{3}.\tag{19}$$

To simplify notation later, define $m(a) \equiv 0$ for the unphysical case $a \leq 0$. In reality, dust grains have some degree of non-sphericity and internal voids (Mathis 1998; Draine 2003; Draine & Fraisse 2009), but this spherical, compact approximation is sufficient for our applications.

Secondly, we assume that a dust particle's grain-size distribution is agnostic as to the chemical composition of the grains. That is, we do not have separate grain-size distributions for grains of different composition (e.g. SiO₂ and MgSiO₃). This reduces computational complexity and also acknowledges the limitations of our galaxy formation model (Vogelsberger et al. 2013), which tracks mass for nine chemical elements: H, He, C, N, O, Ne, Mg, Si, and Fe. Because we track mass only for chemical elements as a whole and not individual chemical compounds, it would not be feasible to assign different grain-size distributions to different grain types. As in previous works (McKinnon et al. 2016, 2017), only C, O, Mg, Si, and Fe are allowed to condense into dust.

Although we do not track complex grain compositions, we do follow the mass of individual chemical elements locked in dust. When a dust particle is created, we store what fraction of the total dust mass came from each chemical element. The total dust mass can be calculated just from the grain-size distribution. When we add or subtract dust mass (e.g. grain growth or sputtering), we keep track of what masses of each element are being added from or returned to gas cells, and update the dust-mass fractions accordingly. In this manner, the total masses of individual chemical elements in gas and dust are conserved during a time-step. Thus, dust particles have one array of dust mass fractions describing chemical composition and one array describing the overall grain-size distribution.

In what follows, we begin with a generic, analytical description of grain-size evolution. Then, we describe the discretization used in our simulations and the various physical processes that modify our grain-size distribution. Our framework builds off of Dwek et al. (2008) and Hirashita & Yan (2009). Conceptually, our methods handle two sorts of processes: those that conserve grain number and those that conserve grain mass.

We first introduce methods to handle number-conserving processes that grow or shrink the radii of individual grains. A dust particle's grain-size distribution thus satisfies the continuity equation:

$$\frac{\partial}{\partial t} \left[\frac{\partial n(a,t)}{\partial a} \right] + \frac{\partial}{\partial a} \left(\frac{\partial n(a,t)}{\partial a} \times \frac{\mathrm{d}a}{\mathrm{d}t} \right) = 0, \tag{20}$$

where $\partial n(a,t)/\partial a \times da$ is the number of grains with radii in the interval [a,a+da] at time t for a given dust particle. This differs from the hydrodynamical continuity equation because the 'velocity' term da/dt for the grain-size distribution may be independent of a and only a function of gas quantities (see discussion of grain

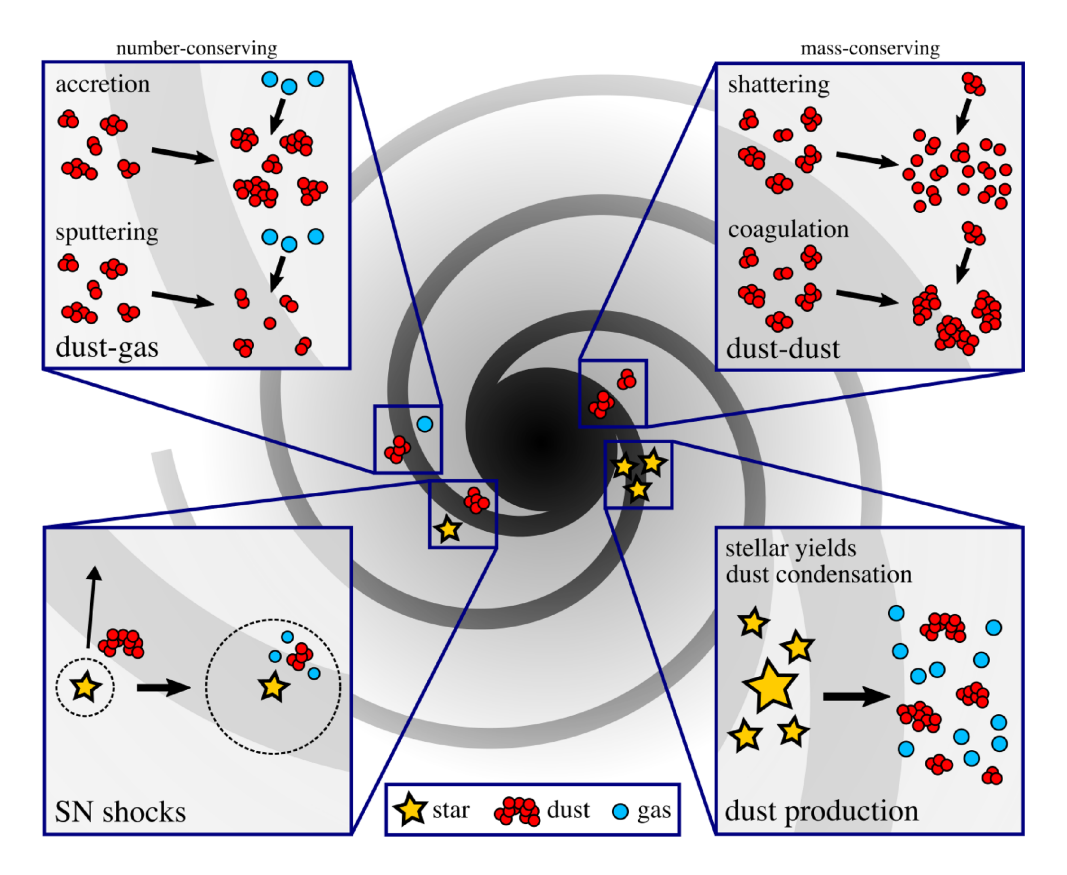


Figure 8. Schematic illustration of the lifecycle of dust within a galaxy. Graphics depict stars (yellow), dust grains (red), and gas-phase metals (blue) in the ISM. Dust grains are produced through stellar evolution, interact with other dust grains and gas-phase metals through collisional processes, and can be destroyed near SNe. Collisional processes are divided into those that conserve grain number (top left) and those that conserve grain mass (top right). Accretion and sputtering change total dust mass by growing or shrinking individual grains, while shattering and coagulation preserve overall mass but affect the number of grains.

growth and thermal sputtering in Sections 3.3 and 3.4, respectively). Thus, unlike the hydrodynamical case where changes in density lead to changes in velocity, shifting the grain-size distribution to smaller or larger radii does not directly affect da/dt. In the limit where da/dt is constant (e.g. small dust-to-gas ratios where the accretion of dust does not materially affect gas metallicities), the grain-size distribution would simply obey the solution $\partial n(a, t + \Delta t)/\partial a = \partial n(a - \dot{a}\Delta t, t)/\partial a$. In practice, although da/dt may not explicitly depend on grain size, shifts in the grain-size distribution lead to changes in dust and metal mass, which in turn can affect gas properties like metallicity and temperature. Thus, da/dt evolves as the gas evolves, and we develop methods to discretize this problem.

Secondly, we address mass-conserving processes like shattering and coagulation in a framework that accounts for grain-grain collisions. These processes do not conserve grain number (i.e. shattering one large grain produces many smaller grains) and do not involve mass transfer to or from gas cells. The underlying physics shares similarities to a wide class of population balance equations (Smoluchowski 1916; Vigil & Ziff 1989; Dubovskii, Galkin & Stewart 1992).

Our methods below discretize the grain-size distribution into N bins in a general way. The N=1 case models a fixed grain size, where changes in dust mass result only from changes in number of grains, not changes in grain radii. The N=2 case is similar to the simplified two-size grain distribution used in recent works (Hirashita 2015; Hou, Hirashita & Michałowski 2016; Hou et al. 2017; Chen et al. 2018).

3.1 Analytic formulation

We assume that grains can have radii in the interval $I_{\text{full}} \equiv [a_{\min}, a_{\max}]$. Define a differential grain-size distribution $\partial n(a, t)/\partial a$ over I_{full} such that $\partial n(a, t)/\partial a \times da$ denotes the number of grains with radii in the range [a, a + da] at time t.

Because we will later discretize this formulation, partition $I_{\rm full}$ into N bins with edges $(a_0^{\rm e}, a_1^{\rm e}, \dots, a_N^{\rm e})$, where $a_0^{\rm e} \equiv a_{\rm min}$ and $a_N^{\rm e} \equiv a_{\rm max}$. At this point, we do not make any assumptions about the spacing of these bins. Bin i covers the interval $I_i \equiv [a_i^{\rm e}, a_{i+1}^{\rm e}]$ with mid-point

$$a_i^{\rm c} \equiv \frac{a_i^{\rm e} + a_{i+1}^{\rm e}}{2}.\tag{21}$$

We write the number of grains in bin i at time t as

$$N_i(t) \equiv \int_{I_i} \frac{\partial n(a, t)}{\partial a} \, \mathrm{d}a, \tag{22}$$

and their mass as

$$M_i(t) \equiv \int_{I_i} m(a) \frac{\partial n(a, t)}{\partial a} \, \mathrm{d}a. \tag{23}$$

We discuss in later sections how various physical processes affect the time-evolution of grain radius. For now we assume that we have a known form of $\dot{a}(a,t) \equiv \mathrm{d}a/\mathrm{d}t$. This may, in principle, be a function of radius and time (the latter because, e.g. if grain radius is changing through collisions with gas atoms, gas properties like density and temperature may evolve in time).

We next consider the time evolution by a small time-step Δt . We can rewrite the number of grains in bin j at time $t + \Delta t$ as the number of grains in any bin at time t that evolve over the time-step to lie in bin t, using

$$N_{j}(t + \Delta t) = \int_{I_{j}} \frac{\partial n(a, t + \Delta t)}{\partial a} da$$

$$= \int_{I_{n, 0}} \mathbb{1}_{j}(a, \dot{a}, t) \frac{\partial n(a, t)}{\partial a} da,$$
(24)

where the indicator function is

$$\mathbb{1}_{j}(a,\dot{a},t) \equiv \begin{cases} 1, & \text{if } a + \dot{a}(a,t)\Delta t \in I_{j}, \\ 0, & \text{else.} \end{cases}$$
 (25)

Using the partition of I_{full}

$$N_j(t + \Delta t) = \sum_{i=0}^{N-1} \int_{I_i} \mathbb{1}_j(a, \dot{a}, t) \frac{\partial n(a, t)}{\partial a} \, \mathrm{d}a. \tag{26}$$

In general, the form of $\dot{a}(a,t)$ determines where the integrands are non-zero. If $\dot{a}(a,t) = \dot{a}(t)$, suitable for collisional processes like grain accretion (e.g. Hirashita & Kuo 2011) or thermal sputtering (e.g. Draine & Salpeter 1979), equation (26) can be simplified as

$$N_j(t + \Delta t) = \sum_{i=0}^{N-1} \int_{I_i \cap (I_j - \dot{a}\Delta t)} \frac{\partial n(a, t)}{\partial a} \, \mathrm{d}a,\tag{27}$$

where we use the shorthand $I_j - \dot{a}\Delta t \equiv [a_j^e - \dot{a}(t)\Delta t, a_{j+1}^e - \dot{a}(t)\Delta t]$ to indicate the range of grain radii at time t that later evolve to fall in bin j at time $t + \Delta t$. This expresses the number of grains in each bin at time $t + \Delta t$ as a summation of integrals of the time t grain-size distribution over overlapping intervals. In many cases, $I_i \cap (I_j - \dot{a}\Delta t)$ may trivially be the empty set: for example, in handling grain growth with $\dot{a} > 0$, this overlap is non-empty only for $\dot{t} \leq \dot{t}$ since grains in bins $\dot{t} = 1$ and above will not shrink.

To this point, we have neglected boundary conditions that enforce $a_{\min} \leq a \leq a_{\max}$ in the grain-size distribution. However, grains may erode or grow such that $a + \dot{a} \Delta t < a_{\min}$ or $a + \dot{a} \Delta t > a_{\max}$ and thus require rebinning. For notational convenience, we define 'bin -1' and 'bin N' as the intervals $I_{-1} \equiv (-\infty, a_{\min}]$ and $I_N \equiv [a_{\max}, \infty)$, respectively. With these definitions, equation (27) can be extended to bins -1 and N, where $N_{-1}(t + \Delta t)$ and $N_N(t + \Delta t)$ represent the number of grains whose radius evolves below a_{\min} or above a_{\max} , respectively. This formulation conserves total grain number, i.e. $N(t + \Delta t) = N(t)$.

While total grain number is conserved, total mass evolves. Paralleling equation (27), the mass in bin j at time $t + \Delta t$ is given by

$$M_{j}(t + \Delta t) \equiv \sum_{i=0}^{N-1} \int_{I_{i} \cap (I_{j} - \dot{a} \Delta t)} m(a + \dot{a} \Delta t) \frac{\partial n(a, t)}{\partial a} da, \qquad (28)$$

where integrals are over the time t grain-size distribution but use the mass $m(a + \dot{a}\Delta t)$ to account for mass at time $t + \Delta t$. Using the definitions of I_{-1} and I_N above and $m(a + \dot{a}\Delta t) \equiv 0$ for $a + \dot{a}\Delta t \leq 0$, equation (28) is valid for $-1 \leq j \leq N$. We note that that if $\dot{a} < 0$ (e.g. thermal sputtering) and $\Delta t \to \infty$, $m(a + \dot{a}\Delta t) \to 0$, implying that all grain mass is destroyed.

An overall grain-size distribution update from time t to $t + \Delta t$ takes place as follows. First, the numbers of grains in bins $0, 1, \ldots, N-1$ at time $t + \Delta t$ are updated using equation (27) and the time t grain-size distribution. Then, $M_j(t + \Delta t)$ is calculated using equation (28) for $-1 \le j \le N$. The change in mass $\Delta m_{\rm d} \equiv m_{\rm d}(t + \Delta t) - m_{\rm d}(t)$

for the dust particle over this time-step is

$$\Delta m_{\rm d} = \sum_{j=-1}^{N} M_j(t + \Delta t) - \sum_{j=0}^{N-1} M_j(t).$$
 (29)

Our rebinning procedure places mass $M_{-1}(t+\Delta t)$ back into bin 0 and mass $M_N(t+\Delta t)$ into bin N-1. This rebinning process conserves the grain mass calculated at time $t+\Delta t$ (and thus $\Delta m_{\rm d}$) but does not conserve total grain number. For example, if $\dot{a}>0$ and $M_N(t+\Delta t)>0$, rebinning will cause the number of grains to increase since grains in bin N-1 are less massive than those in bin N. In the case of a continuous grain-size distribution, there are various ways the grain-size distributions in bins 0 and N-1 can be modified to increase the bin mass. In the following section, we describe how to discretize the grain-size distribution using a piecewise linear approximation.

3.2 Discrete formulation

3.2.1 Evolution of dust mass between grain-size bins

Following Hirashita & Yan (2009), we discretize the grain-size distribution into N log-spaced bins in the following manner. Using the minimum and maximum grain sizes a_{\min} and a_{\max} , respectively, we define the logarithmic bin width

$$\log \delta \equiv \frac{\log a_{\text{max}} - \log a_{\text{min}}}{N}.$$
 (30)

The edges of the N bins are then $(a_0^{\rm e}, a_1^{\rm e}, \ldots, a_N^{\rm e})$, where $a_i^{\rm e} \equiv \delta^i a_{\rm min}$. This specifies the exact partition of $I_{\rm full}$ that we use in the formulation from Section 3.1.

We then assume that the differential grain-size distribution in bin i at time t takes the linear form

$$\frac{\partial n(a,t)}{\partial a} = \frac{N_i(t)}{a_{i+1}^{\rm e} - a_i^{\rm e}} + s_i(t)(a - a_i^{\rm c}),\tag{31}$$

where a_i^c is the mid-point of the bin and $s_i(t)$ denotes the slope. We note that the number of grains in bin i is determined only by the first term, since the second term integrates to zero over the bin's interval. The piecewise linear grain-size distribution at time t is fully determined by the set of $N_i(t)$ and $s_i(t)$ values for all bins. Fig. 9 shows a schematic of this discretization and its evolution in time, which is described below in detail.

Discretizing equation (27), the number of grains in $\sin j$ at time

$$N_{j}(t + \Delta t) = \sum_{i=0}^{N-1} \int_{I_{i,i}} \left(\frac{N_{i}(t)}{a_{i+1}^{e} - a_{i}^{e}} + s_{i}(t)(a - a_{i}^{c}) \right) da,$$
 (32)

where $I_{i,j} \equiv I_i \cap (I_j - \dot{a}\Delta t)$ denotes the portion of bin i that ends up in bin j after the time-step. To help determine whether the intersection of these two intervals I_i and $I_j - \dot{a}\Delta t$ is non-empty, we first set $x_1(i,j) \equiv \max(a_i^{\rm e}, a_j^{\rm e} - \dot{a}\Delta t)$, the maximum of the intervals' left edges, and $x_2(i,j) \equiv \min(a_{i+1}^{\rm e}, a_{j+1}^{\rm e} - \dot{a}\Delta t)$, the minimum of the intervals' right edges. Then, $I_i \cap (I_j - \dot{a}\Delta t) \neq \emptyset$ if and only if $x_2(i,j) \geq x_1(i,j)$, in which case the intersection interval is $[x_1(i,j), x_2(i,j)]$. We define the indicator function

$$\mathbb{1}_{x_2 \ge x_1}(i, j) = \begin{cases} 1, & \text{if } x_2(i, j) \ge x_1(i, j), \\ 0, & \text{else,} \end{cases}$$
 (33)

which is unity when any portion of bin i evolves into bin j over the time-step. To improve readability below, we will often label $x_1(i, j)$ and $x_2(i, j)$ without their implied arguments i and j. Simplifying

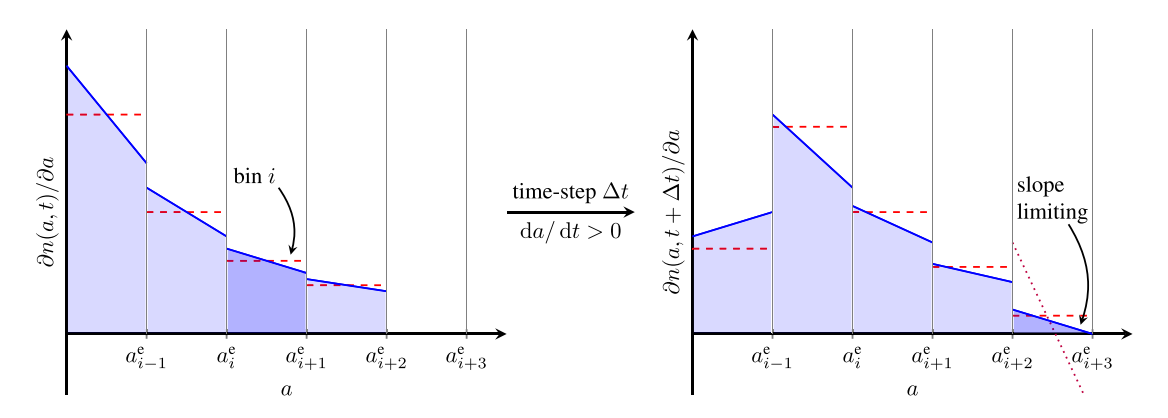


Figure 9. Schematic illustration of a piecewise linear grain-size distribution evolving from time t (left) to $t + \Delta t$ (right). We assume that da/dt > 0 during the time-step, although the opposite case is similar. Solid blue lines mark the piecewise linear discretization, with the shaded region in each bin giving the number of grains. Dashed red lines show a possible piecewise constant discretization. At time t, we assume the piecewise linear and constant methods yield the same number of grains in a given bin (i.e. dashed red lines pass through the mid-points of the solid blue lines). By the end of the time-step, this property is not maintained (e.g. here, the piecewise constant method overestimates the number of grains leaving the leftmost bin). At time $t + \Delta t$, the rightmost bin is subject to slope limiting: if the mass and number of grains entering this bin yield a grain-size distribution that drops below zero (dotted purple line), the slope is limited to remove this unphysical behaviour. Slope limiting preserves a bin's total grain mass. To improve readability, this figure adopts linearly spaced bins. In practice, the formulation outlined in Section 3.2 uses log-spaced bins.

equation (32) yields

$$N_{j}(t + \Delta t) = \sum_{i=0}^{N-1} \mathbb{1}_{x_{2} \ge x_{1}}(i, j) \int_{x_{1}}^{x_{2}} \left(\frac{N_{i}(t)}{a_{i+1}^{e} - a_{i}^{e}} + s_{i}(t)(a - a_{i}^{c}) \right) da$$

$$= \sum_{i=0}^{N-1} \mathbb{1}_{x_{2} \ge x_{1}}(i, j) \left[\frac{N_{i}(t)a}{a_{i+1}^{e} - a_{i}^{e}} + s_{i}(t) \left(\frac{a^{2}}{2} - a_{i}^{c} a \right) \right]_{a=x_{1}}^{a=x_{2}}. \quad (34)$$

This reduces the calculation of the number of grains in bin j at time $t + \Delta t$ to a sum over factors involving the time t grain-size distribution. Similarly, the mass in bin j at time $t + \Delta t$ comes from discretizing equation (28) as

$$M_{j}(t + \Delta t) = \sum_{i=0}^{N-1} \mathbb{1}_{x_{2} \ge x_{1}}(i, j) M_{i \to j}(t, \Delta t), \tag{35}$$

where

$$M_{i \to j} \equiv \int_{x_1}^{x_2} m(a + \dot{a} \Delta t) \left(\frac{N_i(t)}{a_{i+1}^{e} - a_i^{e}} + s_i(t)(a - a_i^{c}) \right) da, \quad (36)$$

denoting mass transfer from bin i to j. Then,

$$M_{j}(t + \Delta t) = \frac{4\pi \rho_{gr}}{3} \sum_{i=0}^{N-1} \mathbb{1}_{x_{2} \ge x_{1}}(i, j) \left[\frac{N_{i}(t)(a + \dot{a}\Delta t)^{4}}{4(a_{i+1}^{e} - a_{i}^{e})} + s_{i}(t) f_{i}^{M}(a, \dot{a}, \Delta t) \right]_{a=1}^{a=x_{2}},$$
(37)

where we use equation (19) to evaluate $m(a + \dot{a}\Delta t)$ and define

$$f_i^M(a, \dot{a}, \Delta t) \equiv \frac{a^5}{5} + (3\dot{a}\Delta t - a_i^c)\frac{a^4}{4} + \dot{a}\Delta t(\dot{a}\Delta t - a_i^c)a^3 + (\dot{a}\Delta t)^2(\dot{a}\Delta t - 3a_i^c)\frac{a^2}{2} - \dot{a}^3\Delta t^3a_i^ca.$$
(38)

Equation (37) also holds for the two boundary bins with j=-1 and j=N, although the case j=-1 requires a small modification. Since bin -1 covers the interval $I_{-1}=(-\infty,a_{\min}]$ and m(a)=0 for $a\leq 0$, we need to ensure we only integrate over grain sizes a with $a+\dot{a}\Delta t>0$. To do this, define $a^*\equiv -\dot{a}\Delta t$ so that a>a* implies $a+\dot{a}\Delta t>0$. Then, for the boundary bin j=-1 only, modify the integrals in equation (37) to be over the intervals $[x_1,x_2]\cap [a*,\infty)$.

Alternatively, if the number of grains $N_j(t + \Delta t)$ and slope $s_j(t + \Delta t)$ are known, the mass in bin j at time $t + \Delta t$ can be expressed as

$$\begin{split} M_{j}(t+\Delta t) \\ &= \int_{a_{j}^{e}}^{a_{j+1}^{e}} \frac{4\pi \rho_{\text{gr}} a^{3}}{3} \left(\frac{N_{j}(t+\Delta t)}{a_{j+1}^{e} - a_{j}^{e}} + s_{j}(t+\Delta t)(a-a_{j}^{c}) \right) da \\ &= \frac{4\pi \rho_{\text{gr}}}{3} \left[\frac{N_{j}(t+\Delta t) a^{4}}{4(a_{j+1}^{e} - a_{j}^{e})} + s_{j}(t+\Delta t) \left(\frac{a^{5}}{5} - \frac{a_{j}^{c} a^{4}}{4} \right) \right]_{a_{j}^{e}}^{a_{j+1}^{e}} (39) \end{split}$$

One can think of $M_j(t + \Delta t)$ not as an explicit function of time but as a function of $N_j(t + \Delta t)$ and $s_j(t + \Delta t)$. We summarize how to update the grain-size distribution in bin j from t to $t + \Delta t$. First, apply equations (34) and (37) to the grain-size distribution at time t to calculate the number and mass of grains at time $t + \Delta t$. Then, use equation (39) to solve for the slope in bin j, $s_j(t + \Delta t)$. This choice of slope ensures bin j has the expected mass of grains.

However, this procedure may result in a slope $s_j(t + \Delta t)$ whose magnitude is so large that the grain-size distribution becomes negative at one of the edges of bin j. Since this is unphysical, we introduce the following slope limiting step. We therefore calculate

$$\left. \frac{\partial n(a,t+\Delta t)}{\partial a} \right|_{a_i^{\rm e}} \equiv \left. \frac{N_j(t+\Delta t)}{a_{j+1}^{\rm e} - a_j^{\rm e}} + s_j(t+\Delta t)(a_j^{\rm e} - a_j^{\rm e}),\right. \tag{40}$$

and

$$\left. \frac{\partial n(a, t + \Delta t)}{\partial a} \right|_{a_{j+1}^{\text{e}}} \equiv \frac{N_j(t + \Delta t)}{a_{j+1}^{\text{e}} - a_j^{\text{e}}} + s_j(t + \Delta t)(a_{j+1}^{\text{e}} - a_j^{\text{c}}). \tag{41}$$

If both of these values are non-negative, no slope limiting is necessary. Furthermore, since the grain-size distribution is piecewise linear and the number of grains $N_j(t+\Delta t)>0$, at most one of these values could be negative. Without loss of generality, we assume $\partial n(a,t+\Delta t)/\partial a|_{a=a_{j+1}^e}<0$, so that $s_j(t+\Delta t)<0$. Let $M_j(t+\Delta t)$ be the mass in bin j computed using equation (37). We will find a new number of grains $\tilde{N}_j(t+\Delta t)$ and slope $\tilde{s}_j(t+\Delta t)$ so that the grain-size distribution at edge a_{j+1}^e is zero (thus ensuring the grain-size distribution is non-negative everywhere in bin j), while keeping the mass in bin j is unchanged. To do this, we use equation (39)

and the unlimited $N_j(t + \Delta t)$ and $s_j(t + \Delta t)$ values to simultaneously solve the linear system

$$M_i(\tilde{N}_i(t+\Delta t), \tilde{s}_i(t+\Delta t)) = M_i(N_i(t+\Delta t), s_i(t+\Delta t)), \quad (42)$$

and

$$\frac{\tilde{N}_{j}(t+\Delta t)}{a_{j+1}^{e}-a_{j}^{e}}+\tilde{s}_{j}(t+\Delta t)(a_{j+1}^{e}-a_{j}^{c})=0,$$
(43)

where the unknowns are $\tilde{N}_j(t+\Delta t)$ and $\tilde{s}_j(t+\Delta t)$. This procedure keeps the slope negative but limits its magnitude. Flattening the bin's slope causes the number of grains in the bin to drop, since the average grain mass increases and mass is conserved. We employ a similar procedure when $\partial n(a,t+\Delta t)/\partial a|_{a=a_j^e}<0$, an alternative case that causes the number of grains to increase as the positive slope is flattened. In both cases, this slope limiting preserves the mass in the bin, at the cost of changing the number of grains away from the value predicted by equation (34). Afterwards, we omit the tildes and assume that $N_j(t+\Delta t)$ and $s_j(t+\Delta t)$ refer to the possibly slope limited values in bin j.

3.2.2 Rebinning dust mass to obey grain-size limits

In order to complete the time-step update, we need to address grains whose radii grow above $a_{\rm max}$ or shrink below $a_{\rm min}$. There are several approaches one could take. In this work, we move grains that evolve beyond the allowed size limits back into the closest grain size bin in a mass-conserving manner. Alternatively, we could assume that grains whose radii evolve below $a_{\rm min}$ are destroyed and set their mass to zero. However, for the galaxy simulations presented in Section 5, we have found that these two approaches yield similar results.

Below, we describe our procedure for rebinning grains that become too large or too small. Our steps are given for bin N-1, which contains the largest grains. The steps for bin 0 are similar. As in the case of slope limiting, tildes indicate quantities after rebinning.

Before any rebinning, the average grain size in bin N-1 is

$$\langle a \rangle_{N-1}(t + \Delta t) = \frac{1}{N_{N-1}} \int_{a_{N-1}^{e}}^{a_{N}^{e}} a \left(\frac{N_{N-1}}{a_{N}^{e} - a_{N-1}^{e}} + s_{N-1}(a - a_{N-1}^{c}) \right) da$$

$$= \left[\frac{a^{2}/2}{a_{N}^{e} - a_{N-1}^{e}} + \frac{s_{N-1}}{N_{N-1}} \left(\frac{a^{3}}{3} - \frac{a_{N-1}^{c} a^{2}}{2} \right) \right]_{a=a_{N-1}^{e}}^{a=a_{N-1}^{e}}, \tag{44}$$

where on the right we drop the arguments of $N_{N-1}(t+\Delta t)$ and $s_{N-1}(t+\Delta t)$ for brevity. The mass $M_N(t+\Delta t)$ to be added to bin N-1 consists of grains with radii larger than $a_N^{\rm e}$, the maximum radius allowed in bin N-1. During rebinning, let us suppose we shrink these grains to have radius $a_N^{\rm e}$, so that $N_{N-1}^{\rm rebin}(t+\Delta t)=M_N(t+\Delta t)/(4\pi\rho_{\rm gr}a_N^{\rm e})^3/3$ denotes the equivalent number of grains. Then, by rebinning this excess mass at the maximum possible radius, the average grain size in bin N-1 increases to

$$\langle \tilde{a} \rangle_{N-1}(t + \Delta t) = \frac{N_{N-1} \langle a \rangle_{N-1} + N_{N-1}^{\text{rebin}} a_N^e}{N_{N-1} + N_{N-1}^{\text{rebin}}},$$
(45)

where for readability we omit the argument $t + \Delta t$ in quantities on the right. We note that we can also rewrite equation (44) to express the average grain size after rebinning in terms of unknowns $\tilde{N}_{N-1}(t+\Delta t)$ and $\tilde{s}_{N-1}(t+\Delta t)$ that characterize the grain-size distribution in bin N-1 after rebinning. As in the case of slope

limiting, we enforce mass conservation, so that

$$M_{N-1}(\tilde{N}_{N-1}(t+\Delta t), \tilde{s}_{N-1}(t+\Delta t))$$

$$= M_{N-1}(N_{N-1}(t+\Delta t), s_{N-1}(t+\Delta t)) + M_N(t+\Delta t),$$
 (46)

where M_{N-1} is computed using equation (39) and M_N using equation (37). We perform the rebinning step by simultaneously solving for $\tilde{N}_{N-1}(t+\Delta t)$ and $\tilde{s}_{N-1}(t+\Delta t)$ from equations (45) and (46), which can be expressed as a linear system. This ensures that rebinning conserves mass and places rebinned grains at the largest possible grain radius. If necessary, we slope limit bin N-1 after rebinning. The procedure for bin 0 is essentially identical, with grains that evolve below the minimum grain radius $a_0^{\rm e}$ shifted back to this edge.

This converts the continuous grain-size distribution framework from Section 3.1 into a piecewise linear framework. In some of the tests below, we also simulate a piecewise constant grain-size distribution by forcing the slope in every bin to be zero. This considerably simplifies the number and mass updates in equations (34) and (39) and alleviates the need for slope limiting. We rebin boundary mass during a time-step by adding $M_N(t + \Delta t)/\langle m \rangle_{N-1}$ grains to bin N-1 and $M_{-1}(t+\Delta t)/\langle m \rangle_0$ grains to bin 0, where $\langle m \rangle_j$ is the average mass of a grain in bin j and is completely specified only by the edges of bins.

3.2.3 Transfer of mass between gas and dust

One additional complexity to discuss is the transfer of mass between gas and dust. Let us assume that, during a time-step, changes in the grain-size distribution cause a dust particle to change in mass by $\Delta m_{\rm d}$. We carry out this mass transfer over $N_{\rm ngb}$ neighbouring gas cells in a kernel-weighted fashion, similar to equation (13). If $\Delta m_{\rm d} > 0$, the dust particle expects to gain mass from gas cells, and there is a risk that those cells do not contain enough metals. We discuss this complication later.

As discussed at the start of Section 3, each dust particle and gas cell tracks what fraction f_k of its mass comes from each chemical element k. If $\Delta m_{\rm d} < 0$ and dust mass is being returned to gas cells, we choose to keep these dust mass fractions constant. For example, if a dust particle with mass fractions f_k is set to transfer mass $w_i \Delta m_d$ to gas cell i for some weight w_i , the gas cell gains mass $f_k w_i \Delta m_d$ in species k. Similarly, if $\Delta m_{\rm d} > 0$ and dust mass is being accreted from gas cells, we choose to keep constant the relative ratios of gas cell mass fractions corresponding to those chemical elements which can condense onto dust grains. We reiterate that only C, O, Mg, Si, and Fe can contribute to dust grains in our model. Using the notation above, suppose gas cell i has mass fractions f_k , and define $f_{\text{sum}} \equiv f_{\text{C}} + f_{\text{O}} + f_{\text{Mg}} + f_{\text{Si}} + f_{\text{Fe}} \le 1$. Let $\hat{f}_k \equiv f_k / f_{\text{sum}}$ for k $\in \{C, O, Mg, Si, Fe\}$. Then, the gas cell loses mass $\hat{f}_k w_i \Delta m_d$ in each of these five elements. Using these accreted masses, the dust particle's normalized mass fractions for each chemical element are recalculated. Regardless of the sign of $\Delta m_{\rm d}$, the mass fractions in affected gas cells are also recomputed.

This procedure assumes that gas cells always have enough metals for dust particles to accrete in a time-step. However, this may not be the case, particularly if a dust particle has already accreted many nearby metals and surrounding gas cells have low or zero metal mass. To account for this, we break the dust particle update into two steps. First, we perform the grain-size distribution calculations above to determine the new number of grains $N_j(t+\Delta t)$ and slope $s_j(t+\Delta t)$ in each bin j, assuming surrounding gas cells have enough metals to accrete the expected mass $\Delta m_d^{\rm exp}$ over the time-step. When

performing the mass transfer from gas cells to the dust particle, we keep track of the actual metal mass $\Delta m_{\rm d}^{\rm act}$ that gas cells are able to transfer. A gas cell i with kernel weight w_i transfers the minimum of $w_i \Delta m_{\rm d}^{\rm exp}$ and its available metal mass, so that summing over nearby gas cells gives $\Delta m_{\rm d}^{\rm act} \leq \Delta m_{\rm d}^{\rm exp}$. As the second step, once mass transfer is complete, we perform the grain-size distribution's time-step update by setting the number of grains in bin j at time $t+\Delta t$ to be $N_j(t)+\Delta m_{\rm d}^{\rm act}/\Delta m_{\rm d}^{\rm exp}\times (N_j(t+\Delta t)-N_j(t))$ and the slope to be $s_j(t)+\Delta m_{\rm d}^{\rm act}/\Delta m_{\rm d}^{\rm exp}\times (s_j(t+\Delta t)-s_j(t))$. This approach ensures that the change in dust particle mass equals $\Delta m_{\rm d}^{\rm act}$, the actual amount of accreted metals. The case of dust mass-loss is much simpler: we are always able to transfer all desired mass back to nearby gas cells (i.e. $\Delta m_{\rm d}^{\rm act}=\Delta m_{\rm d}^{\rm exp}$), and so no special handling is needed.

When transferring mass between gas cells and dust particles, we also update other conserved quantities like momentum. When a dust particle of mass $m_{\rm d}$ and velocity $v_{\rm d}$ transfers mass $\Delta m_{\rm d}$ to a surrounding gas cell of mass $m_{\rm g}$ and velocity $v_{\rm g}$, the dust particle and gas cell's momenta are updated to $m_{\rm d}v_{\rm d} - \Delta m_{\rm d}v_{\rm d}$ and $m_{\rm g}v_{\rm g} + \Delta m_{\rm d}v_{\rm d}$, respectively. We employ this exchange not only for $\Delta m_{\rm d} > 0$ but also for $\Delta m_{\rm d} < 0$, when dust accretes from surrounding gas. In general galaxy applications, the stopping time-scale (equation 14) is short enough that local gas and dust velocities are similar.

During mass transfer, we keep a gas cell's internal energy per unit mass constant. Using its updated mass and momentum, the gas cell's energy is then recomputed as the sum of thermal and kinetic components. More complicated momentum and energy exchanges based on detailed fluid–solid interactions are beyond the scope of this work.

3.2.4 Grain-size evolution test problems

Fig. 10 shows a test of the convergence properties of the piecewise linear and piecewise constant methods. Using various choices for number of bins N, we evolve the same initial grain-size distribution and compare with the expected analytic result. The limits of the grain-size distribution are $a_{\min} = 0.001 \, \mu \mathrm{m}$ and $a_{\max} = 1 \, \mu \mathrm{m}$, and the initial grain-size distribution $\partial n(a,t=0\,\mathrm{Gyr})/\partial a \propto \Pi_{a_{\min}}^{a_{\mathrm{cut}}}(a)$ is given in terms of the 'boxcar' function

$$\Pi_a^b(x) \equiv \begin{cases} 1, & \text{if } a \le x \le b, \\ 0, & \text{else.} \end{cases}$$
(47)

Here, $a_{\rm cut} \equiv a_{\rm min}(a_{\rm max}/a_{\rm min})^{1/4}$ lies one-quarter of the way between $a_{\rm min}$ and $a_{\rm max}$ on a logarithmic scale. We note that $\Pi_a^b(x) = H(x-a) - H(x-b)$, where H is the Heaviside step function. Thus, the initial grain-size distribution takes a constant, non-zero value over the interval $a_{\rm min}$ to $a_{\rm cut}$. The grain growth rate is fixed at $\dot{a}=0.005~\mu{\rm m\,Gyr}^{-1}$, and we calculate the fractional error in dust mass at $t=5~{\rm Gyr}$, after grains grow by $0.025~\mu{\rm m}$. The analytic grain-size distribution is simply $\partial n(a,t)/\partial a \propto \Pi_{a_{\rm cut}}^{a_{\rm cut}+\dot{a}t}(a)$.

The piecewise constant method yields first-order accuracy, while the piecewise linear method largely displays second-order behaviour apart from a slight softening of the convergence rate for $N \gtrsim 512$. In this test, the fractional mass error for N=64 bins is roughly 40 per cent for the piecewise constant discretization and just 1 per cent for the piecewise linear one. In the tests and applications below, we use the piecewise linear method for its improved accuracy and convergence properties.

We next study the impact of the mass rebinning procedure given by equation (46) in order to highlight the fact that rebinning may

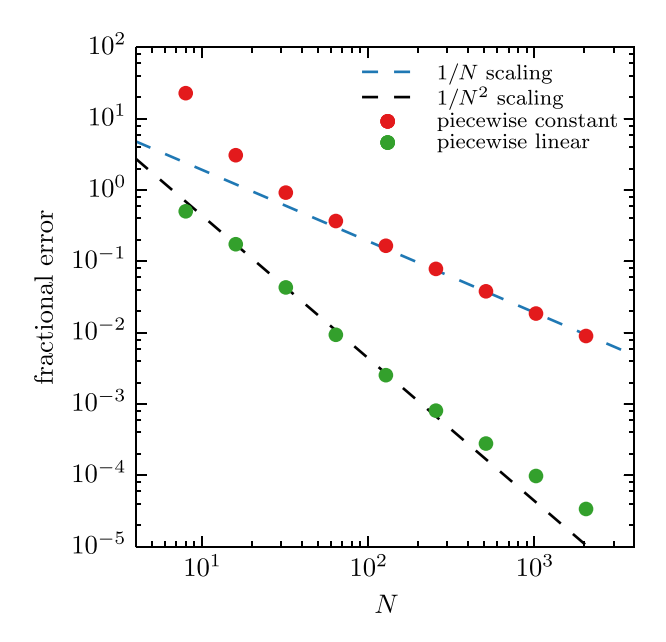


Figure 10. Convergence results for the grain growth test, plotting fractional dust mass error as a function of number of grain bins N. We evolve a single dust particle whose grain-size limits are $a_{\min} = 0.001 \, \mu m$ and $a_{\max} = 1 \, \mu m$ and whose initial grain-size distribution $\partial n(a,t=0 \, {\rm Gyr})/\partial a \propto \Pi_{a_{\min}}^{a_{\rm cut}}(a)$ is non-zero and uniform over the interval from a_{\min} to $a_{\rm cut} \equiv a_{\min}(a_{\max}/a_{\min})^{1/4}$. As a result, only a quarter of bins have a non-zero number of grains at $t=0 \, {\rm Gyr}$. We fix the grain radius growth rate $a=0.005 \, \mu m \, {\rm Gyr}^{-1}$. Results are shown at $t=5 \, {\rm Gyr}$ for the piecewise constant (red) and piecewise linear (green) discretizations. Dashed lines show 1/N (blue) and $1/N^2$ scalings (black). The piecewise constant discretization provides a first-order method, while the piecewise linear discretization deviates slightly from a second-order scaling only at large N.

conserve mass during each time-step but not yield the expected long-term behaviour. Fig. 11 shows the mass evolution of a dust particle whose initial grain-size distribution has minimum grain size $a_{\min} = 0.015625 \, \mu \text{m}$ and takes the form $\partial n(a,t=0)/\partial a \propto \Pi_{a_l}^{a_r}(a)$, where $a_l = a_{\min} \delta^{45}$, $a_r = 1 \, \mu \text{m}$, and

$$\log \delta = \frac{\log a_{\rm r} - \log a_{\rm min}}{60}.\tag{48}$$

Thus, a_1 lies three-quarters of the logarithmic distance between a_{\min} and a_r . As a result, the initial grain-size distribution is non-zero and uniform over $[a_1, a_r]$. We perform three runs, all of which use the same minimum grain size a_{\min} and bin-spacing factor δ but vary the number of bins N. The maximum grain size $a_{\max} = a_{\min} \delta^N$ for these runs is $1 \, \mu m$ (for $N = 60 \, \text{bins}$), $2 \, \mu m$ (N = 70), and $4 \, \mu m$ (N = 80). Since the initial grain-size distribution and bin spacing is the same across all three runs, this test allows us to determine the impact of the maximum allowable grain size and rebinning procedure on mass evolution while keeping resolution fixed. The grain growth rate is fixed to $\dot{a} = 0.3 \, \mu m \, \text{Gyr}^{-1}$.

The dust particle's mass most closely follows the analytic result when $a_{\rm max}$ is large and the effect of rebinning is small. Because the largest grains at t=0 Gyr are 1 $\mu{\rm m}$ in size, when $a_{\rm max}=1$ $\mu{\rm m}$ some grains are subject to rebinning starting on the very first timestep. In contrast, grains are rebinned less often for $a_{\rm max}=2$ $\mu{\rm m}$, whose profile displays better accuracy. Although the $a_{\rm max}=4$ $\mu{\rm m}$ test should not involve any rebinning in theory (even the largest grains that start at a=1 $\mu{\rm m}$ will not grow larger than $a_{\rm max}$), in practice the slope limiting procedure will introduce some diffusion that populates then largest grain-size bins over time. However, this

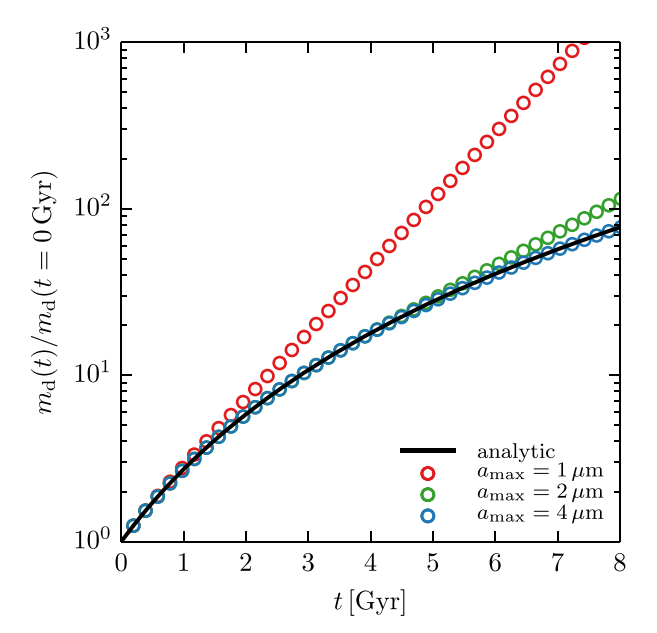


Figure 11. Mass evolution of a dust particle with a grain-size distribution that is uniform over a fixed range at t=0 Gyr and whose largest grains are 1 μ m in size. We perform three runs that share the same minimum grain size. These runs increase the maximum allowable grain size $a_{\rm max}$ but also increase the number of bins to keep the same bin-spacing factor δ from equation (30). We fix $\dot{a}=0.3$ μ m Gyr⁻¹ and evolve the dust particle until t=8 Gyr so that grains grow by 2.4 μ m. Coloured circles show the mass evolution of the dust particle, normalized to its initial mass, for these runs using the piecewise linear formulation with boundary mass rebinning. The black line denotes the expected analytic result. By increasing the maximum allowable grain size, we reduce inaccuracies from the rebinning procedure that artificially limits grain size.

effect is sufficiently small that the test with $a_{max} = 4 \mu m$ yields mass evolution visually indistinguishable from the analytic result.

This behaviour is easy to understand intuitively: consider a grain of radius $a=1~\mu m$ and time-steps such that $\dot{a}\,\Delta t=1~\mu m$. Over two time-steps without rebinning, the grain will grow to have radius $3~\mu m$. Next, suppose we adopt rebinning so that grains are not allowed to grow beyond $1~\mu m$: then, after the first time-step, the grain grows to radius $2~\mu m$ and is replaced with eight grains of radius $1~\mu m$. After the second time-step, this process repeats for each of these eight grains, so that at the end we have 64 grains of radius $1~\mu m$. The ratio of final mass with rebinning to final mass without rebinning is $64/3^3>1$: in this case, mass has artificially grown too quickly. Since mass scales non-linearly as radius cubed, artificially limiting grain radii can allow mass discrepancies to build up over time.

These results suggest rebinning mass is acceptable when the fraction of dust particle mass affected is small (as in the $a_{\rm max}=2~\mu{\rm m}$ run), not large (as in the $a_{\rm max}=1~\mu{\rm m}$ run). Rebinning is not guaranteed to provide the correct long-term behaviour, but it can preserve mass from time-step to time-step. In practice, we recommend using knowledge of typical time-scales and grain growth rates (e.g. in cosmological contexts, $t\sim14~{\rm Gyr}$) to estimate a rough maximum grain size and adopting this as $a_{\rm max}$. For example, interstellar grain-size distributions typically extend from $a_{\rm min}=0.001~\mu{\rm m}$ to $a_{\rm max}=1~\mu{\rm m}$ (Weingartner & Draine 2001a), but the size distribution for, say, protoplanetary applications would extend to much larger radii.

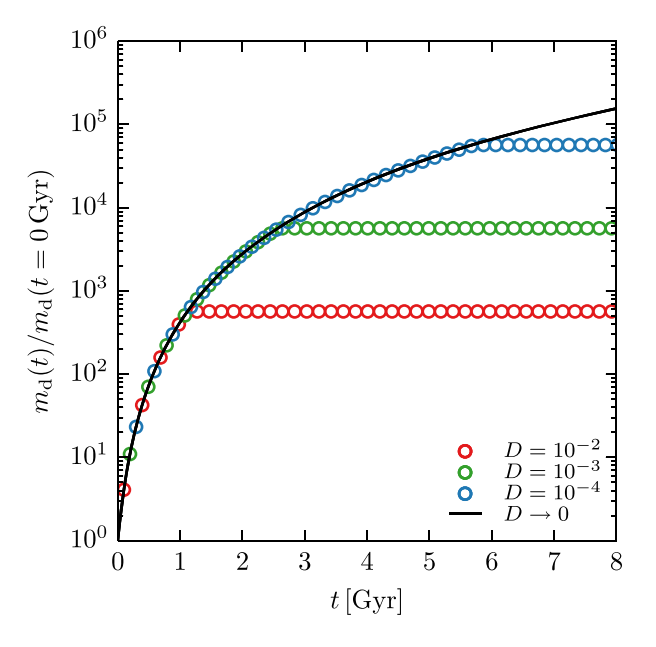


Figure 12. Demonstration of grain growth in gas with a fixed amount of metals. The grain growth rate is fixed at $\dot{a}=0.025~\mu m\, {\rm Gyr}^{-1}$, and the dust particle's smoothing length is chosen so that it encloses $N_{\rm ngb}=64\pm8$ neighbouring gas cells. Neighbouring gas cells are located on a uniform lattice with equal mass and have metallicity Z=0.1. The dust-to-gas ratio D is the initial mass ratio between the dust particle and a neighbouring gas cell. The dust particle increases its mass $m_{\rm d}(t)$ by a factor of $N_{\rm ngb}Z/D$ before the surrounding gas runs out of metals. The black line shows the expected analytic mass growth if the gas is treated as an infinite reservoir of metals.

Up to this point, we have considered cases where the gas surrounding a dust particle always contains enough metals to deplete onto grains. However, if the gas has a limited supply of metals, the growth of dust may deviate from the expected behaviour. Fig. 12 shows the mass evolution of a single dust particle surrounded by a uniform lattice of equal-mass gas cells. The ratio of initial dust particle mass to gas cell mass, D, is chosen to be 10^{-4} , 10^{-3} , or 10^{-2} , and the initial gas metallicity is Z = 0.1. We intentionally choose a large value of metallicity to provide a reservoir of metals for dust to deplete. The grain radius rate of growth is fixed to $\dot{a} = 0.025 \,\mu\text{m Gyr}^{-1}$. The dust particle is able to accrete metals in a kernel-weighted fashion from neighbouring gas cells within its smoothing length, determined using equation (10) and $N_{\rm ngb} = 64 \pm 8$. The limits and initial condition of the grain-size distribution are the same as those used in Fig. 10, although they do not affect this test.

As expected, the dust particle is able to grow its mass by a factor of $N_{\rm ngb}Z/D$, at which point neighbouring gas cells within the smoothing length run out of metals. Afterwards, the dust particle's mass is constant. Decreasing D increases the relative abundance of metals to dust and prolongs the point at which dust accretion stops. Of course, in a realistic setting it is possible for gas to be re-enriched with metals (e.g. through stellar evolution) and dust to resume its accretion.

Fig. 13 demonstrates how the piecewise constant and piecewise linear methods reproduce a grain-size distribution as it evolves under mass growth and mass-loss. We adopt $a_{\min} = 0.001 \,\mu\text{m}$ and $a_{\max} = 1 \,\mu\text{m}$ and use N = 128 bins. The initial grain-size distribution is non-zero and constant over the middle quarter of bins covering the interval $[a_{\min}\delta^{3N/8}, a_{\min}\delta^{5N/8}]$, where δ is the usual bin-spacing factor from equation (30). The grain growth rate \dot{a} is a

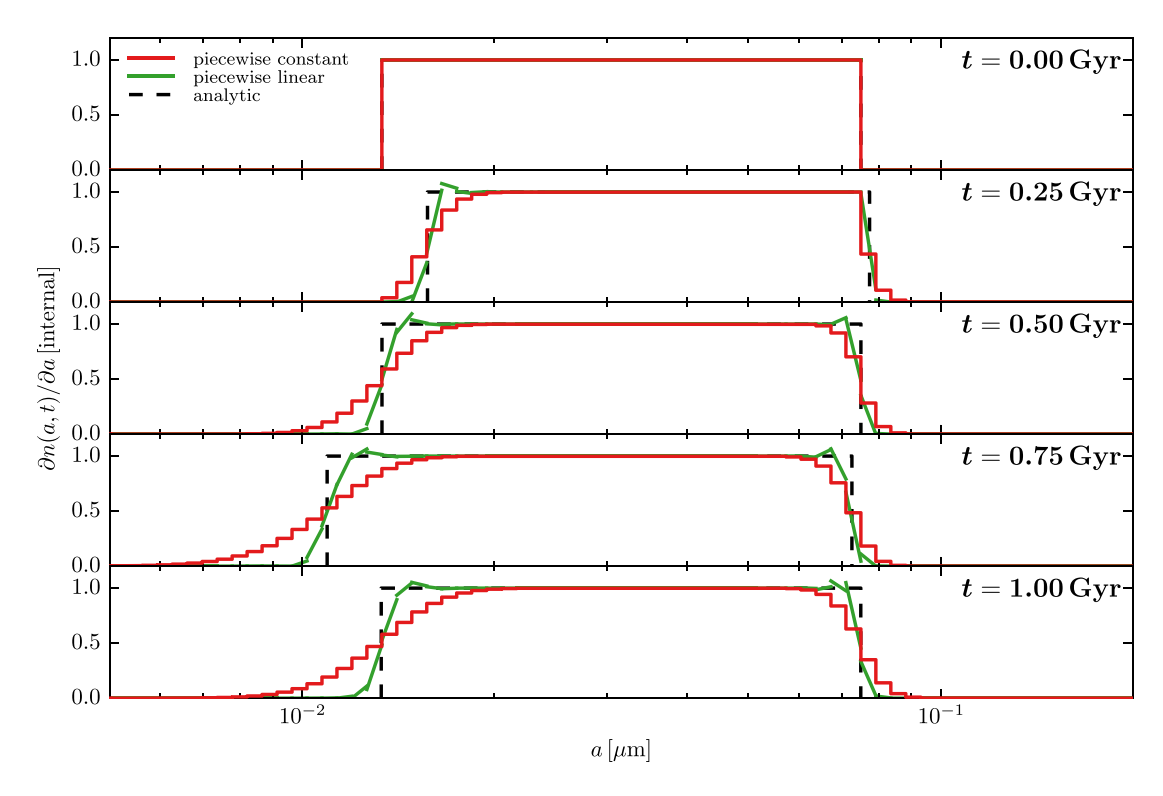


Figure 13. Grain-size evolution for dust where \dot{a} varies sinusoidally with amplitude 0.015 μ m Gyr⁻¹ and period 1 Gyr. We compare the piecewise constant (red) and piecewise linear (green) discretizations with the expected analytic solution (black). From top to bottom, we show the grain-size distribution as it evolves over quarter-periods. The piecewise linear method better captures discontinuities where the grain-size distribution jumps to zero.

sinusoid with amplitude $0.015~\mu m\, Gyr^{-1}$ and period 1 Gyr. Grainsize distribution boundary effects are unimportant for this choice of amplitude.

As the grain-size distribution evolves over one full period, the piecewise constant and piecewise linear discretizations experience some numerical diffusion in reproducing the jump discontinuities in the grain-size distribution. However, the piecewise linear method is better able to preserve the steepness of the discontinuity. After one period, the piecewise linear grain-size distribution takes an extra three bins beyond the left-most analytic discontinuity to become visually consistent with zero. In contrast, the piecewise constant method requires an extra nine bins. In a test like this, combining mass growth and mass-loss, the piecewise linear method does a far better job of reproducing the analytic result and reducing numerical diffusion

In the above tests, we used arbitrary choices for \dot{a} to enable comparison with analytic results. Below, we describe the form that \dot{a} takes for various physical processes.

3.3 Grain growth

Dust grains in the ISM can grow by accreting gas-phase metals (Draine 1990; Dwek 1998; Michałowski et al. 2010), and a number of accretion parametrizations have been used in models in recent years (e.g. Zhukovska et al. 2008; Hirashita & Kuo 2011; Hirashita 2012; Asano et al. 2013b; de Bennassuti et al. 2014; Hirashita & Voshchinnikov 2014; Popping et al. 2017). In this work, we follow equation 5 from Hirashita & Kuo (2011) and equations 19 and 20 from Hirashita & Voshchinnikov (2014). We calculate the growth

rate of a dust grain of radius a as

$$\frac{\mathrm{d}a}{\mathrm{d}t} \approx \left(\frac{Z}{Z_{\odot}}\right) \left(\frac{n_{\mathrm{H}}}{10^{3} \,\mathrm{cm}^{-3}}\right) \left(\frac{T}{10 \,\mathrm{K}}\right)^{1/2} \left(\frac{S_{\mathrm{acc}}}{0.3}\right) \,\mathrm{\mu m \, Gyr}^{-1}, \quad (49)$$

where $Z_{\odot}=0.0127$ is the solar metallicity, Z, $n_{\rm H}$, and T the local gas metallicity, hydrogen number density, and temperature, respectively, and $S_{\rm acc}$ the accretion sticking efficiency. As in equation (13), we determine Z, $n_{\rm H}$, and T by interpolating over neighbouring gas cells.

Although the sticking efficiency $S_{\rm acc}$ is expected to be a function of temperature and to vary in different ISM phases (e.g. Zhukovska et al. 2016), the mass resolution available in cosmological simulations is not sufficient to resolve detailed ISM structure. Thus, we adopt $S_{\rm acc}=0.3$, as in the analytic work of Hirashita & Kuo (2011). While this does not capture the temperature behaviour suggested by some chemisorption and physisorption works (Leitch-Devlin & Williams 1985; Grassi et al. 2011; Chaabouni et al. 2012), it avoids the assumption of unit sticking efficiency adopted in prior works (Asano et al. 2013b; McKinnon et al. 2017; Popping et al. 2017) that has been suggested to overdeplete metals (Zhukovska et al. 2016). Future work could improve on this assumption when more explicit ISM models are implemented.

3.4 Thermal sputtering

Dust grains can be eroded through collisions with thermally excited gas. A number of works have studied this thermal sputtering process in detail for various grain materials and compositions (Ostriker & Silk 1973; Burke & Silk 1974; Barlow 1978; Draine & Salpeter 1979; Dwek & Arendt 1992; Tielens et al. 1994). An analytic approximation to these detailed calculations was provided by equation

14 in Tsai & Mathews (1995), with the rate of erosion for a grain of size a given by

$$\frac{da}{dt} = -(3.2 \times 10^{-18} \,\text{cm}^4 \,\text{s}^{-1}) \left(\frac{\rho_g}{m_p}\right) \left[\left(\frac{T_{\text{sput}}}{T}\right)^{2.5} + 1\right]^{-1}, (50)$$

where $\rho_{\rm g}$ and T are the gas density and temperature, respectively, $m_{\rm p}$ is the proton mass, and $T_{\rm sput} \equiv 2 \times 10^6$ K. Thermal sputtering is strongest for $T \gtrsim 10^6$ K and can affect the size distribution in hot plasmas like the intracluster medium (Yahil & Ostriker 1973; McGee & Balogh 2010) and in interstellar SN shocks (Nozawa et al. 2006; Bianchi & Schneider 2007; Nath et al. 2008; Kozasa et al. 2009; Silvia et al. 2010, 2012).

The sub-resolution ISM model (Springel & Hernquist 2003) that we adopt treats dense, star-forming gas using an effective equation of state. The star-forming ISM typically does not resolve hot, $T > 10^6$ K gas surrounding SNe that could thermally sputter dust grains (see fig. 1 in Torrey et al. 2017, for an example gas-phase diagram). We therefore also require a sub-resolution scheme that accounts for the sputtering of grains by SNe in a star-forming ISM, which we introduce in the following section. Together, Sections 3.4 and 3.5 combine to model grain sputtering outside and inside the star-forming ISM, respectively. In the future, more explicit ISM models with better resolution could attempt to directly capture the multiphase structure of the ISM and avoid such sub-resolution prescriptions.

3.5 Supernova destruction

High-velocity shocks produced by SNe can also destroy dust grains and shift the grain-size distribution to smaller sizes (Nozawa et al. 2006; Bianchi & Schneider 2007; Nozawa et al. 2007; Nath et al. 2008; Silvia et al. 2010). Because we do not directly resolve individual SNe in our galaxy formation model, we account for the destruction of dust in SN shocks using the sub-resolution ISM model by tying the dust destruction rate to the local SN rate.

We parallel section 2.2.3 of Asano et al. (2013b), which applied the methods developed in Yamasawa et al. (2011) to determine the influence of SN shocks on the ISM grain-size distribution. These methods are parametrized in terms of a function $\xi(a_f, a_i)$ such that, for our bin discretization, $\xi(a_j^c, a_i^c) \times (a_{j+1}^e - a_j^e)$ denotes the fraction of grains starting in bin i that end up in bin j after one SN shock. Following the aforementioned works, we use the ξ values calculated by Nozawa et al. (2006) in detailed modelling of SN blasts.

Integrating equations 12 and 14 of Asano et al. (2013b) over the width of bin j, we obtain the rate of change of number of grains in bin j,

$$\frac{\mathrm{d}N_{j}}{\mathrm{d}t} = \frac{M_{\text{swept}}\gamma_{\text{SN}}}{M_{\text{ISM}}} \left(\sum_{i=0}^{N-1} \xi(a_{j}^{\text{c}}, a_{i}^{\text{c}})(a_{j+1}^{\text{e}} - a_{j}^{\text{e}})N_{i}(t) - N_{j}(t) \right),$$
(51)

and the rate of change of mass of grains in $\sin j$,

$$\frac{\mathrm{d}M_{j}}{\mathrm{d}t} = \frac{M_{\mathrm{swept}}\gamma_{\mathrm{SN}}}{M_{\mathrm{ISM}}} \times \left\{ \sum_{i=0}^{N-1} \left[\xi(a_{j}^{\mathrm{c}}, a_{i}^{\mathrm{c}}) N_{i}(t) \left(\frac{\pi \rho_{\mathrm{gr}} a^{4}}{3} \right) \right]_{a=a_{j}^{\mathrm{c}}}^{a=a_{j+1}^{\mathrm{c}}} - M_{j}(t) \right\}.$$
(52)

Here, γ_{SN}/M_{ISM} is the ratio of SN rate to mass in the ISM, and M_{swept} is the mass that an SN sweeps up. Following the fitting

function presented in equation 8 of Yamasawa et al. (2011), we use

$$\frac{M_{\text{swept}}}{M_{\odot}} \equiv 1535 \left(\frac{n}{1 \text{ cm}^{-3}}\right)^{-0.202} \left(\frac{Z}{Z_{\odot}} + 0.039\right)^{-0.289},\tag{53}$$

in terms of the local ISM density n and metallicity Z. We calculate the prefactor $M_{\rm swept} \gamma_{\rm SN}/M_{\rm ISM}$ by kernel-averaging over neighbouring gas cells, where $\gamma_{\rm SN}$ and $M_{\rm ISM}$ are the local SN rate and mass of each gas cell. The local SN rate in a gas cell is computed using the star formation rate predicted by the sub-resolution ISM model (Springel & Hernquist 2003) and the mass fraction of stars that explode as SNe II for a chosen initial mass function (IMF). After updating the number and mass of grains in each bin using equations (51) and (52), we then apply equation (39) to determine each bin's slope and slope limit as before if necessary.

3.6 Shattering

To this point, we have discussed physical processes that conserve grain number but not grain mass, with mass either gained from or returned to gas by growing or shrinking grain radii. However, it is important to also consider grain–grain collisional processes like shattering and coagulation that conserve total grain mass. In general, such processes could be treated as an inhomogeneous source term in the grain number continuity equation (see equation 20). However, it is numerically easier to separate the treatment of shattering and coagulation from the number-conserving methods in Section 3.2. This enables us to take advantage of formalisms developed to study particle population dynamics (e.g. Smoluchowski 1916).

Conceptually, shattering causes large grains to fragment and produces many smaller grains. Two grains can collisionally shatter when their relative velocity is above a threshold value. Suppose grains of size a_1 and a_2 have speeds $v(a_1)$ and $v(a_2)$, respectively. In principle, grain speeds can be influenced by local gas properties like density and temperature. When colliding, the grains have relative velocity $v_{\text{rel}}(a_1, a_2) = \sqrt{v(a_1)^2 + v(a_2)^2 - 2v(a_1)v(a_2)\cos\theta}$, where $\cos \theta$ accounts for impact angle. In this work, we follow Hirashita & Li (2013) and stochastically calculate relative velocities between two grains by drawing $\cos \theta$ values randomly from the interval [-1, 1]. Because of the limited resolution of our ISM model, we compute grain velocities as a function of grain size with a subresolution scheme, using the small-scale turbulent ISM models of Yan et al. (2004). In particular, Yan et al. (2004) studied the dynamics of different size grains in a variety of ISM phases, including the cold neutral medium (CNM) and warm ionized medium (WIM). Grain velocities as a function of grain size tabulated for these ISM phases and used in our work are shown in Fig. 14. Appendix A details how grain velocities in the CNM and WIM are combined with our equation of state model to estimate velocities for populations of grains in the ISM. These velocity curves allow us to calculate the relative velocities $v_{\rm rel}(a_1, a_2)$ that determine shattering rates, which have been studied in a variety of works (Voelk et al. 1980; Markiewicz, Mizuno & Voelk 1991; Cuzzi & Hogan 2003; Yan, Lazarian & Draine 2004; Ormel & Cuzzi 2007; Ormel et al. 2009; Hirashita & Li 2013; Paruta, Hendrix & Keppens 2016).

Because shattering and coagulation are mass-conserving and not number-conserving processes, it is useful to define a differential mass density

$$\frac{\partial \rho(a,t)}{\partial a} \equiv \left(\frac{m(a)}{V_{\rm d}}\right) \frac{\partial n(a,t)}{\partial a},\tag{54}$$

such that $\partial \rho(a, t)/\partial a \times da$ is the mass density of grains with radii in the interval [a, a + da] at time t. Here, $V_d \equiv m_d/\rho_d$ is the volume

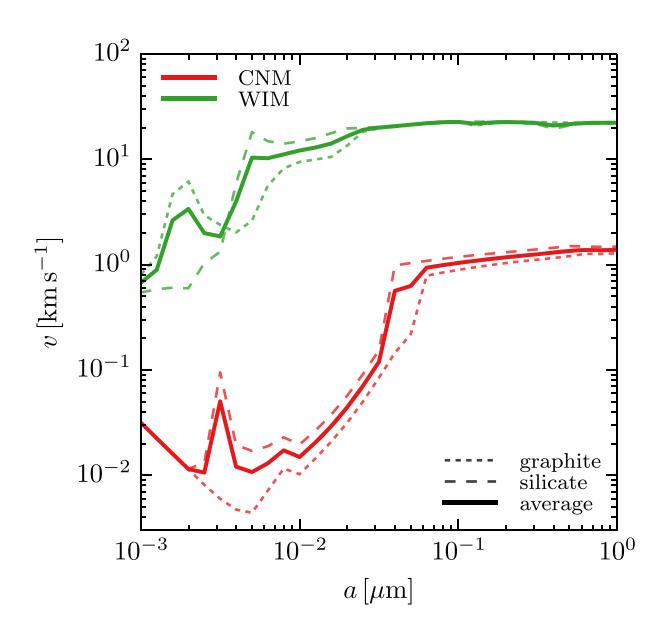


Figure 14. Grain velocities for the CNM and WIM phases of the turbulent ISM predicted by Yan et al. (2004). For each phase, velocity curves are shown for graphite grains (short dashed lines), silicate grains (long dashed lines), and an average of the two (solid lines). Bigger grains tend to have larger velocities, and velocities in the WIM exceed those of the CNM. Relative velocities between grains of different sizes are used to compute grain shattering and coagulation rates.

associated with a dust particle, where $m_{\rm d}$ is its known mass and $\rho_{\rm d}$ is a kernel-weighted dust density estimate using neighbouring dust particles. Because dust particles may vary in mass more than gas cells, when finding dust neighbours we use a smoothing length enclosing a desired amount of dust mass instead of a number of neighbours. Further details on this procedure are provided in Section 4.5.

Shattering has been studied numerically using piecewise constant discretizations (O'Donnell & Mathis 1997; Hirashita & Yan 2009) and analytically in the continuous case (Dubovskii et al. 1992; Asano et al. 2013b; Mattsson 2016). We parallel these implementations in adapting shattering to our piecewise linear discretization, noting that in Hirashita & Yan (2009) and Asano et al. (2013b), what we label $\partial \rho(a, t)/\partial a$ they denote $\rho(a, t)$. Following equation (23) of Asano et al. (2013b), shattering causes the mass density for grains of size a to evolve with the rate

$$\frac{\partial}{\partial t} \left[\frac{\partial \rho(a,t)}{\partial a} \right] = -m(a) \frac{\partial \rho(a,t)}{\partial a} \int_{a_{\min}}^{a_{\max}} \alpha(a,a_1) \frac{\partial \rho(a_1,t)}{\partial a_1} da_1
+ \frac{1}{2} \int_{a_{\min}}^{a_{\max}} \int_{a_{\min}}^{a_{\max}} \left[\alpha(a_1,a_2) \frac{\partial \rho(a_1,t)}{\partial a_1} \frac{\partial \rho(a_2,t)}{\partial a_2} \right]
\times m_{\text{shat}}(a,a_1,a_2) da_2 da_1,$$
(55)

where

$$\alpha(a_1, a_2) \equiv \begin{cases} \frac{\pi(a_1 + a_2)^2 v_{\text{rel}}(a_1, a_2)}{m(a_1) m(a_2)}, & v_{\text{rel}}(a_1, a_2) > v_{\text{shat}}, \\ 0, & v_{\text{rel}}(a_1, a_2) \leq v_{\text{shat}}, \end{cases}$$
(56)

is a function of effective cross-section, grain relative velocity, and grain masses that only allows collisions when relative velocities are above the shattering threshold $v_{\rm shat}$, and $m_{\rm shat}(a, a_1, a_2)\,{\rm d}a$ is the mass of grains in the size interval $[a, a+{\rm d}a]$ produced through shattering grains of sizes a_1 and a_2 . Apart from one test problem detailed later in this section, in all other applications we calculate $m_{\rm shat}(a, a_1,$

 a_2) following section 2.3 of Hirashita & Yan (2009), which allows grains to fully or partially fragment depending on the sizes of colliding grains. In equation (55), the first term accounts for the removal of grains of size a in collisions with grains of size a_1 , while the second term describes the injection of grains of size a in collisions with grains of sizes a_1 and a_2 . Because it is easier to work with, our definition of m_{shat} accounts for mass produced by both colliding grains and not just one of the grains, as in Hirashita & Yan (2009). This necessitates the factor of 1/2 in the second term in equation (55). For v_{shat} , Jones et al. (1996) uses 2.7 km s⁻¹ for silicate grains and $1.2\,\mathrm{km}\,\mathrm{s}^{-1}$ for graphite grains. Because we do not track detailed grain chemistry, we adopt $v_{\rm shat} \approx 2 \, {\rm km \, s^{-1}}$ for all grain populations. For simplicity, we use an indicator function to write $\alpha(a_1, a_2) \equiv$ $\pi(a_1 + a_2)^2 v_{\text{rel}}(a_1, a_2) \mathbb{1}_{v_{\text{rel}} > v_{\text{shat}}}(a_1, a_2) / (m(a_1)m(a_2))$. We show in Appendix A how these integrals can be discretized given a piecewise linear grain-size distribution and suitable approximations.

After discretizing and approximating, the mass evolution for bin i turns into

$$V_{\rm d} \frac{{\rm d}M_{i}}{{\rm d}t} = -\pi \sum_{k=0}^{N-1} v_{\rm rel}(a_{i}^{\rm c}, a_{k}^{\rm c}) \mathbb{1}_{v_{\rm rel} > v_{\rm shat}}(a_{i}^{\rm c}, a_{k}^{\rm c}) \langle m \rangle_{i} I^{i,k}$$

$$+ \frac{\pi}{2} \sum_{k=0}^{N-1} \sum_{j=0}^{N-1} v_{\rm rel}(a_{k}^{\rm c}, a_{j}^{\rm c}) \mathbb{1}_{v_{\rm rel} > v_{\rm shat}}(a_{k}^{\rm c}, a_{j}^{\rm c}) m_{\rm shat}^{k,j}(i) I^{k,j},$$
(57)

where $\langle m \rangle_i$ is the average mass of a grain in bin *i* computed using only the bin edges and

$$I^{k,j}(t) \equiv \int_{a_k^e}^{a_{k+1}^e} \int_{a_j^e}^{a_{j+1}^e} \left[\left(\frac{N_k(t)}{a_{k+1}^e - a_k^e} + s_k(t)(a_1 - a_k^c) \right) \right] \times \left(\frac{N_j(t)}{a_{j+1}^e - a_j^e} + s_j(t)(a_2 - a_j^c) \right) (a_1 + a_2)^2 da_1$$
(58)

is a polynomial function dependent on the grain-size distribution at time t. For brevity, we do not write its analytic form here. In the limit that bin slopes go to zero, equation (57) recovers the piecewise constant update from equation 4 of Hirashita & Yan (2009). Unlike the number-conserving processes in Section 3.2.2, the shattering update in equation (57) requires no rebinning of grains with radii below a_{\min} or above a_{\max} . Instead, we follow the steps in equations 14 through 19 of Hirashita & Yan (2009) to ensure all grains resulting from shattering have radii in the allowed size range.

Using the grain-size distribution at time t, for a time-step Δt we compute the change in mass in each bin using the simple first-order update $M_i(t+\Delta t)=M_i(t)+dM_i/dt\times\Delta t\equiv M_i(t)+\Delta M_i$, where ΔM_i is the change in dust mass in bin i. Because of the numerical approximation in equation (A4), it is possible for the change in dust particle mass $\Delta m_{\rm d} \equiv \sum_{i=0}^{N-1} \Delta M_i$ to deviate slightly from zero. In the limit $N\to\infty$, this approximation is exact and does not introduce any numerical error. To ensure $\Delta m_{\rm d}=0$ during the time-step, we use the following rescaling. When $\Delta m_{\rm d}>0$, we choose to limit the mass gain in those bins with $\Delta M_i>0$. More precisely, let

$$\Delta m_{\text{sub}} \equiv \sum_{i|\Delta M_i > 0} \Delta M_i \tag{59}$$

be the total change in mass from the subset of bins gaining mass. We then subtract $\Delta m_{\rm d} \times \Delta M_i / \Delta m_{\rm sub}$ from each bin i with $\Delta M_i > 0$, ensuring the new bins satisfy $\sum_{i=0}^{N-1} \Delta M_i = 0$. If instead $\Delta m_{\rm d} < 0$, we follow a similar procedure, this time reducing the magnitude of

 ΔM_i of those bins with $\Delta M_i < 0$. In the text below, we assume that ΔM_i values refer to changes in bin mass after ensuring $\Delta m_d = 0$.

Because the grain-size distribution is parametrized in terms of the number of grains and slope in each bin, we break the number-slope degeneracy by adding a heuristic modelling changes in average grain size. This mirrors the steps used to handle boundary mass rebinning in Section 3.2. Assuming shattered grains have the grain-size distribution $\partial n/\partial a \propto a^{-3.3}$ (Jones et al. 1996; Hirashita & Yan 2009), a shattered grain injected into bin i has average size $\langle a \rangle_i^{\text{shat}} \equiv 2.3/1.3 \times [(a_{i+1}^e)^{-1.3} - (a_i^e)^{-1.3}]/[(a_{i+1}^e)^{-2.3} - (a_i^e)^{-2.3}]$ and average mass $\langle m \rangle_i^{\text{shat}} \equiv 4\pi \rho_{\text{gr}}/3 \times -2.3/0.7 \times [(a_{i+1}^e)^{-0.7} - (a_i^e)^{0.7}]/[(a_{i+1}^e)^{-2.3} - (a_i^e)^{-2.3}]$. If shattering injects grains into bin i and causes it to gain mass $(\Delta M_i \geq 0)$, we approximate the new average grain size as a weighted average of sizes for grains already in the bin and those added to the bin. That is, we assume the new average grain size in bin i is

$$\langle a \rangle_i(t + \Delta t) = \frac{N_i(t) \times \langle a \rangle_i(t) + \Delta N_i \times \langle a \rangle_i^{\text{shat}}}{N_i(t) + \Delta N_i},$$
(60)

where $\Delta N_i \equiv \Delta M_i/\langle m \rangle_i^{\rm shat}$ estimates the number of shattered grains added to bin *i*. If bin *i* loses grain mass $(\Delta M_i < 0)$, we assume the leftover grains in bin *i* maintain their average grain size and set $\langle a \rangle_i (t + \Delta t) = \langle a \rangle_i (t)$. Using equations (39) and (44), we combine the expression for $\langle a \rangle_i (t + \Delta t)$ and

$$M_i(N_i(t + \Delta t), s_i(t + \Delta t)) = M_i(N_i(t), s_i(t)) + \Delta M_i, \tag{61}$$

and simultaneously solve for the new number of grains $N_i(t + \Delta t)$ and slope $s_i(t + \Delta t)$ in bin i. We slope limit as before if necessary. This finishes the time-step update due to shattering.

In addition to this piecewise linear discretization, we also implement a piecewise constant method. This follows directly from equation 4 of Hirashita & Yan (2009), or equivalently from equation (57) in this work by enforcing that slopes $s_i \rightarrow 0$ and evaluating quantities at bin mid-points. The development of these two discretizations for mass-conserving processes parallels our treatment of number-conserving methods in Section 3.2.

In the following test problem verifying the numerical implementation of shattering, we choose to adopt simplified forms of $v_{\rm rel}$ and $m_{\rm shat}^{k,j}(i)$ so that the grain-size distribution evolves in a more predictable way. All other applications – including the isolated galaxy simulations presented in Section 5 – use the grain velocity and shattering kernel functions detailed in Fig. 14 and equation (55), respectively. Solely for this test, we adopt

$$\frac{v_{\text{rel}}(a_k^{\text{c}}, a_j^{\text{c}})}{\text{km s}^{-1}} \equiv \begin{cases} 3, & a_k^{\text{c}} > 0.1 \,\mu\text{m and } a_j^{\text{c}} > 0.1 \,\mu\text{m}, \\ 0, & \text{else}, \end{cases}$$
(62)

so that only collisions between large grains cross the shattering threshold. In this test, we do not use the effective relative velocity interpolated between tabulated CNM and WIM grain velocities, since it introduces more complicated behaviour. Additionally, for this test only, we do not compute $m_{\rm shat}^{k,j}(i)$ using section 2.3 of Hirashita & Yan (2009), which allows for complex size dynamics (e.g. colliding grains can partially fragment and leave behind remnants, shatter over a small size range, etc.), and instead assume that all colliding grains fully fragment and produce shattered grains in the interval $[a_{\rm min}, a_{\rm max}]$ according to a size power law with index -3.3 (Jones et al. 1996). Thus, in a collision between grains in bins k and j, the resulting mass entering bin i is

$$m_{\text{shat}}^{k,j}(i) = (\langle m \rangle_k + \langle m \rangle_j) \times \left(\frac{(a_{i+1}^{\text{e}})^{0.7} - (a_i^{\text{e}})^{0.7}}{a_{\text{max}}^{0.7} - a_{\text{min}}^{0.7}} \right),$$
 (63)

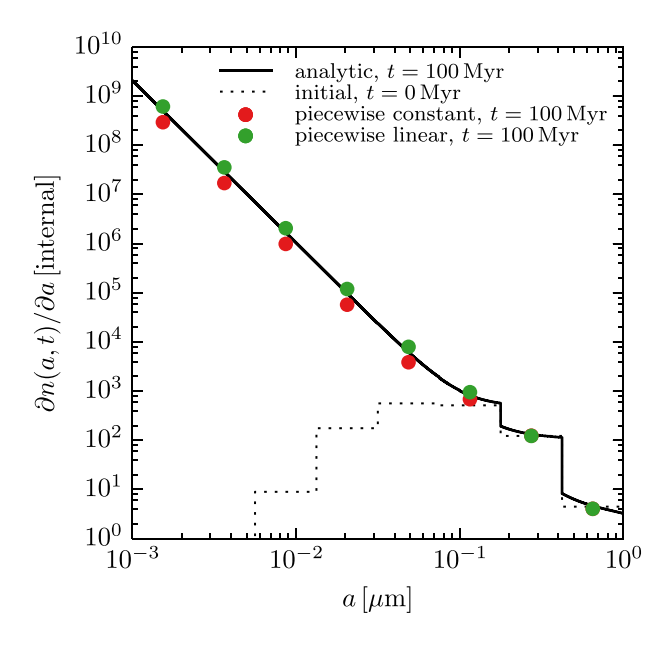


Figure 15. Influence of shattering on grain-size evolution for an initially lognormal size distribution (dotted black line), using a simplified set of grain velocity and mass fragment parameters as detailed in the text. Coloured circles show results at $t=100\,\mathrm{Myr}$ for the piecewise constant (red) and piecewise linear (green) discretizations using N=8 bins. We compare with the expected solution at $t=100\,\mathrm{Myr}$ (solid black line) computed using a high-precision differential equations solver. Shattering produces many small grains following the power-law $\partial n/\partial a \sim a^{-3.3}$, although most mass remains in the largest bins.

where $\langle m \rangle_k$ is the average mass of a grain in bin k computed for a constant size distribution, as in Section 3.2.

Paralleling a similar test in section 2.1 of Hirashita (2010), we initialize one dust particle with a lognormal grain-size distribution

$$\frac{\partial n(a, t = 0 \,\text{Myr})}{\partial a} = \frac{C}{a} \exp\left(-\frac{\ln^2(a/a_0)}{2\sigma^2}\right) \tag{64}$$

over the interval from $a_{\rm min}=0.001~\mu{\rm m}$ to $a_{\rm max}=1~\mu{\rm m}$, where $a_0=0.1~\mu{\rm m}$ and $\sigma=0.6$. The volume has a gas density corresponding to $n_{\rm H}\approx 0.4~{\rm cm}^{-3}$, and the normalization constant C is chosen so that the dust-to-gas ratio is $D=3.7\times 10^{-3}$, the average of values used in Hirashita (2010). We generate piecewise constant initial conditions, so that they can be used with both discretizations.

Fig. 15 demonstrates the evolution of the initially lognormal grain-size distribution under the influence of only shattering. We compare results at t=100 Myr using piecewise constant and piecewise linear discretizations. Both capture the formation of small grains following a $\partial n/\partial a \sim a^{-3.3}$ power law, although the piecewise linear method better reproduces the solution predicted by a high-accuracy numerical integrator. Despite shattering forming many small grains, we caution that most mass remains in large grains: for the piecewise linear discretization in this test, the fractions of mass in the smallest and largest bins are 1×10^{-3} and 5×10^{-1} , respectively. Although we directly computed these values, one can use $a^4 \times \partial n(a,t)/\partial a$ as a proxy for the mass-size distribution, given that $\partial n(a,t)/\partial a$ has dimensions of inverse length. Because shattering is a collisional process, it will more rapidly transfer mass to smaller grains in regions of higher dust density.

3.7 Coagulation

Although dust grains in high-velocity collisions can shatter, grains in low-velocity collisions can stick together and aggregate. This process of coagulation shifts the grain-size distribution to larger sizes, particularly in dense regions of the ISM (Chokshi et al. 1993; Jones et al. 1996; Dominik & Tielens 1997; Hirashita & Yan 2009; Mattsson 2016). The formalism of dust coagulation also shares many similarities with a wide class of population balance equations (Smoluchowski 1916; Vigil & Ziff 1989; Dubovskii et al. 1992; Krivitsky 1995; Lee 2001; Filbet & Laurençot 2004; Fournier & Laurençot 2005). A variety of methods have been used to numerically model dust coagulation, including a piecewise constant grainsize discretization (Hirashita & Yan 2009), a Monte Carlo-based collision evolution simulator (Ormel et al. 2009), direct numerical integration of the integro-differential coagulation equation (Asano et al. 2013b), a method of moments approach that does not explicitly evolve the grain-size distribution (Mattsson 2016), and a finite volume method applied to the conservative form of the coagulation equation (Paruta et al. 2016).

We explicitly include the effect of coagulation on the grain-size distribution by modifying the piecewise linear formalism developed in Section 3.6 for shattering. The governing equation for coagulation is the same as equation (57) for shattering, except that we replace $m_{\rm shat}^{k,j}(i)$ with the kernel

$$m_{\text{coag}}^{k,j}(i) \equiv \begin{cases} m_k + m_j, & a_i^{\text{e}3} \le \frac{m_k + m_j}{4\pi \rho_{\text{gr}}/3} < a_{i+1}^{\text{e}-3}, \\ 0, & \text{else.} \end{cases}$$
(65)

That is, when grains in bins k and j coagulate, they form a larger grain whose mass is the sum of the colliding masses. We also use velocity indicator functions of the form

$$\mathbb{1}_{v_{\text{rel}} < v_{\text{coag}}}(a_k^{\text{c}}, a_j^{\text{c}}) = \begin{cases} 1, & v_{\text{rel}}(a_k^{\text{c}}, a_j^{\text{c}}) < v_{\text{coag}}^{k,j}, \\ 0, & v_{\text{rel}}(a_k^{\text{c}}, a_j^{\text{c}}) \ge v_{\text{coag}}^{k,j}, \end{cases}$$
(66)

This ensures that grains in bins k and j coagulate only when their relative velocity is below the coagulation threshold velocity, which depends on the indices k and j and is calculated following equation 8 in Hirashita & Yan (2009). Given their high velocities, grains in the largest size bins do not coagulate (Hirashita & Yan 2009). As a result, the sizes of grains resulting from coagulation are less than the maximum allowed value of a_{max} and require no rebinning.

We calculate the mass transfer between grain-size bins from coagulation using equation (57) together with the coagulation mass kernel $m_{\rm coag}^{k,j}(i)$. In order to solve for number of grains, $N_i(t)$, and slope, $s_i(t)$, in each bin, we require a second constraint. For shattering, we utilized a heuristic about a bin's average grain radius, since the inclusion of shattering is expected to produce new grains following a roughly $\partial n/\partial a \propto a^{-3.3}$ size distribution. For coagulation, we do not have a similar analytic expression for the size distribution of new grains in a bin. As a result, we reuse the same form of equation (60) and solve in bin i for an estimated average grain size $\langle a \rangle_i (t + \Delta t)$ at the end of the time-step, where here ΔN_i denotes the number of grains entering a bin from coagulation. Since $\langle a \rangle_i (t)$ and $\langle a \rangle_i^{\rm shat}$ lie within bin i, so too will their weighted average $\langle a \rangle_i (t + \Delta t)$. We then solve for the number of grains and slope in each bin by simultaneously solving equations (60) and (61).

While this procedure does not take into account some physical intuition for the size distribution of grains within a bin that results from coagulation, it provides a second constraint that can be used together with the mass in a bin to solve for the post-coagulation bin state. As we demonstrate in Fig. 16, even this simplified procedure allows the grain-size distribution to track the effects of coagulation.

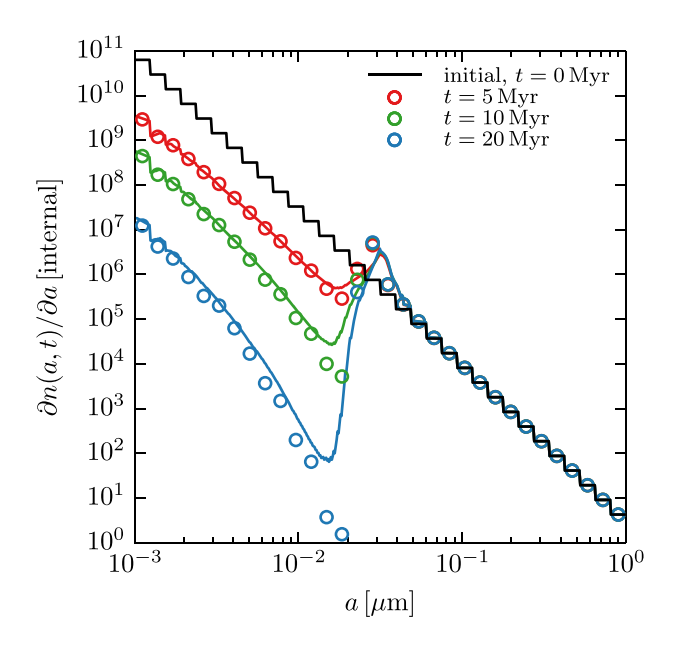


Figure 16. Evolution of an initial grain-size distribution $\partial n(a, t = 0 \, \mathrm{Myr})/\partial a \sim a^{-3.5}$ (black line) under the influence of coagulation. Grain-size distributions are computed at various times (coloured circles) using the piecewise linear discretization and N = 32 bins. Coloured lines show profiles predicted by a numerical differential equations integrator with many bins. Coagulation reduces the number of small grains and in this test produces grains near $a \approx 0.03 \, \mu\mathrm{m}$.

Fig. 16 demonstrates the effect of coagulation on an initial grainsize distribution $\partial n(a,t=0\,\mathrm{Myr})/\partial a\sim a^{-3.5}$. To avoid unnecessary complexity, in this test the velocities of grains in individual bins are not calculated by interpolating the tabulated grain velocities from Yan et al. (2004) but instead follow the form

$$v(a) = 1.1 \times 10^3 \left(\frac{a}{0.1 \,\mu\text{m}}\right)^{1/2} \,\text{cm}\,\text{s}^{-1} \tag{67}$$

from Hirashita & Li (2013). For this test only, we set the threshold velocity $v_{\rm coag}^{k,j}=1.1\times 10^3\,{\rm cm\,s^{-1}}$, independent of k and j. (That is, we do not use the more complicated expression in equation 4 of Hirashita & Li 2013, which depends on the radii of colliding grains.) We note that small grains will coagulate. For simplicity, we assume a fixed collision angle $\cos\theta=-1$ when calculating relative collision velocities. We adopt a gas density $n_{\rm H}\approx 10^5\,{\rm cm^{-3}}$ and dust-to-gas ratio D=0.01 and integrate for 20 Myr using the piecewise linear discretization with N=32 bins. We compare results with those predicted by a numerical integrator solving coupled ordinary differential equations, starting from the same initial conditions but using many times more bins.

In this test, coagulation shifts mass from small grains to medium-sized grains, producing a local peak in the grain-size distribution at $a \approx 0.03 \, \mu \text{m}$. Because mass is conserved, the number of small grains lost is greater than the number of medium-sized grains created, and so total grain number decreases. Since large grains have velocities exceeding the coagulation threshold, the grain-size distribution for $a \gtrsim 0.05 \, \mu \text{m}$ is largely unchanged from its initial state. We do not include shattering in this test, which would redistribute some of these large grains to smaller sizes. The results from the piecewise linear discretization with N=32 bins capture the qualitative behaviour predicted by the numerical differential equations integrator. Although there is some tension near $a \approx 0.02 \, \mu \text{m}$, where the grain-

size distribution experiences a sharp increase, results improve as more bins are added.

Together with Section 3.6, this demonstrates how shattering and coagulation can shift grains to smaller or larger grain sizes in a mass-conserving manner.

3.8 Time-step constraints and sub-cycling for grain-size evolution

We apply a time-step constraint to ensure that changes in a dust particle's grain-size distribution are resolved. When evolving a grain-size distribution over a time-step Δt to account for some grain size process (e.g. shattering), we calculate the effective time-scale

$$\tau_{\rm GSD} \equiv \min_{i} \frac{m_{\rm d}}{\Delta M_{i} / \Delta t},\tag{68}$$

where m_d is the particle mass, ΔM_i is the change in mass in bin i, and the minimization is over all grain-size bins.

We then update a grain-size distribution with a time-step obeying $\Delta t < \chi \tau_{\rm GSD}$, where χ is a CFL-like parameter less than unity. This restricts the change in mass in a grain-size bin to be at most a fraction χ of the total particle mass. We note that even processes that conserve overall dust particle mass (shattering and coagulation) may transfer mass between grain-size bins and thus impose a time-step constraint.

It is often the case that grain-size evolution takes place on shorter time-scales than those for gravity and drag. To improve computational efficiency, we use a sub-cycling procedure that resolves these time-scales for grain-size evolution without subjecting dynamical forces to such short time-steps. We introduce a parameter $\lambda \geq 1$ and require the particle time-step to resolve $\lambda \chi \tau_{GSD}$. This constraint is combined with the dynamical time-step requirements in equation (17) to determine a dust particle's overall time-step, during which dynamical forces like gravity and drag are applied and kernel estimates are calculated. Local grain-size distribution updates are then performed using approximately λ time-steps of smaller size $\Delta t < \chi \tau_{\rm GSD}$, using kernel estimates (e.g. gas density and dust density) computed at the start of the larger particle time-steps. While there is some flexibility in choosing values for χ and λ in simulations of isolated galaxies presented in Section 5, we adopt $\chi = 0.1$ and $\lambda = 2$.

This sub-cycling avoids the need for many tiny updates to a dust particle's position and velocity from gravity and drag forces when grain-size evolution takes place on time-scales much shorter than these dynamical forces.

3.9 Dust drag with evolving grain-size distributions

In Section 2, we implemented a dust drag force assuming grains had one fixed size. Here, we briefly extend that formulation to account for drag on dust particles with a grain-size distribution. Since the stopping time-scale for one grain depends linearly on grain size a (see equation 9), let $t_s \equiv \beta a$, where β accounts for all other dependences. The magnitude of the drag force on a dust particle with mass m_d is given by

$$F_{\rm d} = \int_{a_{\rm min}}^{a_{\rm max}} \left(\frac{\partial n}{\partial a}\right) \left(\frac{4\pi \rho_{\rm gr} a^3}{3}\right) \left(\frac{|\boldsymbol{v}_{\rm d} - \boldsymbol{v}_{\rm g}|}{\beta a}\right) \, {\rm d}a, \tag{69}$$

recalling that $\partial n/\partial a \times da$ gives the number of grains with radius in the interval [a, a+da]. We can alternatively write the drag force as $F_{\rm d}=m_{\rm d}|v_{\rm d}-v_{\rm g}|/t_{\rm s}^{\rm eff}$ in terms of an effective stopping time-scale $t_{\rm s}^{\rm eff}$. Equating these two expressions, applying the piecewise linear

grain-size discretization, and solving for the effective stopping timescale, we find

$$t_{s}^{\text{eff}} = \frac{3\beta m_{d}}{4\pi \rho_{gr}} \left[\sum_{i=0}^{N-1} \int_{a_{i}^{e}}^{a_{i+1}^{e}} \left(\frac{N_{i}}{a_{i+1}^{e} - a_{i}^{e}} + s_{i}(a - a_{i}^{c}) \right) a^{2} da \right]^{-1}$$

$$= \frac{3\beta m_{d}}{4\pi \rho_{gr}} \left\{ \sum_{i=0}^{N-1} \left[\frac{N_{i}a^{3}/3}{a_{i+1}^{e} - a_{i}^{e}} + s_{i} \left(\frac{a^{4}}{4} - \frac{a_{i}^{c}a^{3}}{3} \right) \right]_{a_{i}^{e}}^{a_{i+1}^{e}} \right\}^{-1}. (70)$$

In general, t_s^{eff} is a function of time, as the grain-size distribution (i.e. N_i and s_i values) will evolve in time. Going forwards, we use this calculation of effective stopping time-scale when applying drag kicks to dust particles with a full grain-size distribution.

We caution, however, that applying an effective force to an entire dust particle does not allow grains of different sizes to properly segregate when moving in one direction. In the isolated galaxy simulations presented in Section 5 without feedback, we neglect forces like radiation pressure or unresolved galactic winds that could drive outflows on large scales. However, Ferrara et al. (1991) suggest that radiation pressure can drive grains more than 100 kpc from the galactic centre, with grains of different sizes and compositions experiencing different strength forces. Future simulations including feedback should address the limitation of effective forces acting on dust particles.

4 DUST PRODUCTION

To this point, we have discussed how a dust particle's grain-size distribution evolves in time, but we have not yet specified how the initial grain-size distribution is set. In practice, dust is injected into the ISM by evolving stars (e.g. Todini & Ferrara 2001; Ferrarotti & Gail 2006), and stars of different types produce dust with different size distributions and chemical compositions. This production of solid dust happens simultaneously with the production of gas-phase metals.

In this section, we first describe a stochastic procedure for forming dust particles of a certain target mass as star particles evolve. Then, we describe the initial grain-size distributions assigned to these newly created dust particles. There are several competing trends to balance in deciding whether to form many, lower-mass dust particles or fewer, higher-mass dust particles. On the one hand, adopting a low-mass threshold for dust particles reduces the stochasticity of our particle creation scheme and better models continuous dust injection from stars. The more dust particles we create, the more finely we can sample from a star's initial grain-size distribution and see grains of different sizes segregate during drag kicks. On the other hand, creating many dust particles can make simulations computationally inefficient.

4.1 Dust particle creation

Star formation prescriptions in cosmological simulations often stochastically convert gas elements into star particles (e.g. Springel & Hernquist 2003; Vogelsberger et al. 2013; Hopkins et al. 2014; Schaye et al. 2015). Similarly, stochastic approaches have been used to model stellar evolution and convert star particles to back into gas particles in SPH simulations (Torrey et al. 2012). We parallel these methods to stochastically create dust particles.

It is important to draw a distinction between the return of gasphase metals from a star to the ISM and the return of dust. The galaxy formation physics in AREPO handles chemical enrichment of gas-phase metals into the ISM by spreading the metal mass derived from stellar nucleosynthetic yields over neighbouring gas cells using a kernel weighting. However, because dust is not tracked directly in gas cells but instead as a separate particle type, a separate procedure is needed for dust than for gas-phase metals.

During a time-step in which a star particle of mass m_* is expected to form mass $\Delta m_{\rm d}$ of dust, a new dust particle of mass $m_{\rm d}$ is created when a number chosen randomly between 0 and 1 is less than

$$p_{\rm d} = \frac{m_*}{m_{\rm d}} \left[1 - \exp\left(-\frac{\Delta m_{\rm d}}{m_*}\right) \right]. \tag{71}$$

Multiplying equation (71) by m_d , this states that during a timestep the expected dust mass formed equals the change in stellar mass owing to dust synthesis. Over the lifetime of a star particle, this ensures that the correct amount of dust mass is produced in expectation. We initialize a dust particle with the same phase space information as the star particle from which it was spawned.

The choice of desired dust particle mass $m_{\rm d}$ affects how often dust particles are spawned. A natural parametrization is $m_{\rm d}=\beta_{\rm d}m_{*}^{\rm init}$, where $\beta_{\rm d}$ is a constant and $m_{*}^{\rm init}$ is the initial mass of the star particle at birth. We note that $m_{*}^{\rm init}$ will typically be within a factor of a few of the mean gas cell mass used as a target mass in the (de)refinement scheme in AREPO (Vogelsberger et al. 2012). Thus, $\beta_{\rm d}$ controls what fraction of a star's initial mass is converted into dust during each spawn event. In Section 4.3, we show how $\beta_{\rm d}$ impacts the stochasticity of dust return.

Because chemical enrichment of gas-phase metals into surrounding gas cells does not involve the creation of new particles, it can be handled during every time-step in a continuous way. However, for computational reasons, it is sometimes advantageous to adopt a discrete chemical enrichment scheme that only periodically performs enrichment updates of accumulated mass in a deterministic manner. Such discrete enrichment schemes have been used for dust, too. For example, the chemical enrichment model in Bekki (2015) has a star particle creating dust particles only at three times in its evolution, corresponding to the typical lifetimes of SNe II, SNe Ia, and asymptotic giant branch (AGB) stars. While this method is deterministic, it introduces artificial delays in the return of dust to the ISM and does not model continuous enrichment. We restrict ourselves to stochastic dust production schemes in this work.

4.2 Initial grain-size distributions

Once the decision has been made to spawn a dust particle of mass m_d , we next initialize its grain-size distribution. The form of the grain-size distribution depends on the type of stars evolving off the main sequence during the time-step.

Hydrodynamical modelling of pulsating AGB stars predicts that newly created SiC grains obey a lognormal $a^4 \times \partial n/\partial a$ distribution, with mass concentrated in large grains (Yasuda & Kozasa 2012). Following Asano et al. (2013b), we assume that the initial grain-size distribution for all dust produced by AGB stars takes the form

$$\frac{\partial n}{\partial a} = \frac{C}{a^5} \exp\left(-\frac{\ln^2(a/a_{AGB})}{2\sigma_{AGB}^2}\right),\tag{72}$$

where $a_{AGB} = 0.1 \,\mu m$, $\sigma_{AGB} = 0.47$, and C is a normalization constant that determines the overall mass of the dust particle.

Small grains are destroyed in the reverse shocks of SNe due to sputtering (Bianchi & Schneider 2007; Nozawa et al. 2007), and the resulting mass of dust produced by SNe is expected to be biased towards large grains (Nozawa et al. 2007). The initial grain-size distribution used for dust produced by SNe II follows from fig. 6(b) in Nozawa et al. (2007), which presents the relative abundance of

dust grains at various discrete sizes for dust formed from a $20\,\mathrm{M}_\odot$ core-collapse SN in a gas of initial density $n_\mathrm{H}=1\,\mathrm{cm}^{-3}$. However, the discrete grain-size distribution from Nozawa et al. (2007) is not calculated at exactly the same sizes as the edges of our grain bins. To handle this, we calculate the grain-size distribution at each grain bin edge by logarithmically interpolating between neighbouring discrete $\partial n/\partial a$ values calculated in Nozawa et al. (2007). From the $\partial n/\partial a$ values at grain bin edges, we can calculate the number of grains and slope in each bin. Finally, like for AGB stars, we scale the initial grain-size distribution for dust particles produced by SNe II by a constant to ensure the total mass in the grain-size distribution equals the particle's mass.

The time-scale for dust grains supplied by AGB stars to be injected into the ISM is estimated as less than 10^5 yr (Mathews & Brighenti 1999), and for the purposes of this work, we assume no delay in transporting AGB dust into a dust particle in the surrounding gas. This is similar to the time-scale over which dust grains are subjected to reverse shocks in SNe (Bianchi & Schneider 2007). Since we employ the same stellar nucleosynthetic yields used by Illustris (Vogelsberger et al. 2013), AGB stars are assumed to have masses in the range $1-6\,\mathrm{M}_{\odot}$, while SNe II have masses in the range of $6-100\,\mathrm{M}_{\odot}$.

Because the grain-size distribution for dust produced by SNe Ia is uncertain, we assume that dust produced by SNe Ia follows the same size distribution as that from SNe II. However, the net amount of dust produced by SNe Ia is sub-dominant compared to that from SNe II and AGB stars (Nozawa et al. 2011), and some works choose to entirely ignore dust production from SNe Ia (e.g. Asano et al. 2013b). Because SNe Ia dust yields are so low, as discussed in Section 4.3, our choice for the initial size distribution of dust from SNe Ia thus does not meaningfully affect results.

When deciding to stochastically create total dust mass $m_{\rm d}$ with a corresponding grain-size distribution $\partial n/\partial a$, there are a few possible approaches. One approach is to break $\partial n/\partial a$ into several contiguous segments and create $N_{\rm d}$ dust particles of mass $m_{\rm d}/N_{\rm d}$, with each particle's initial grain-size distribution covering only a limited grain-size range. This approach is illustrated in Fig. 17. Summing over particles, this procedure gives the correct initial grain-size distribution, and it also allows for grains of different sizes to stratify under a strong drag force. However, splitting the initial grain-size distribution in this way increases the number of dust particles and computational cost. Additionally, over time the dust particles' initially narrow size distributions will shift to larger and smaller sizes as a result of the physical processes detailed in Section 3, reducing the advantages of creating multiple particles.

In the galactic simulations in this paper, we take the simplest approach and assign the full grain-size distribution to one dust particle. This has the benefit of treating a large range of grain sizes with just one particle, and effective drag updates can be applied using equation (70). This method has a downside: it does not effectively capture the separation of grains of different sizes via the drag force. If constituent grains cover three orders of magnitude in size and thus have drag accelerations varying by the same amount, moving the dust particle using an effective drag acceleration forces its grains to have the same drag acceleration. However, in galaxy applications where the drag stopping time-scale is short and dust is well-coupled to the gas, this is not a serious limitation.

4.3 Dust elemental yields

The probabilities used to stochastically create dust particles are set by the total dust mass Δm_d produced during a star's time-step. The

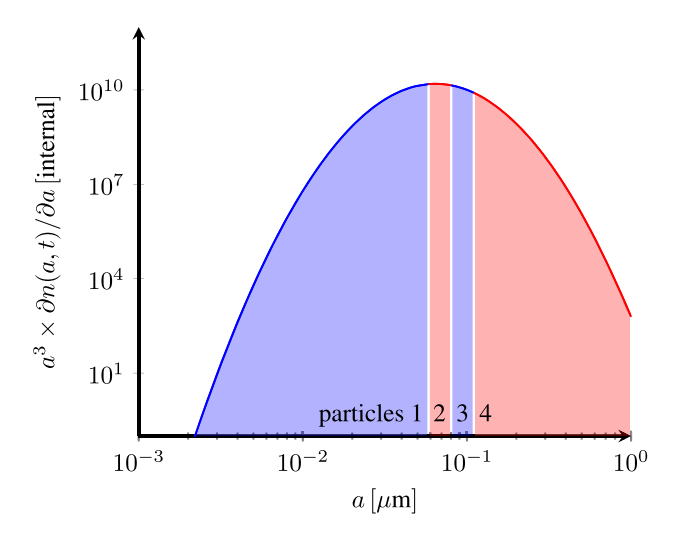


Figure 17. Schematic demonstrating the possible creation of multiple dust particles from an initial grain-size distribution. In this example, we divide the grain-size distribution corresponding to dust from AGB stars (given by equation 72) into $N_d = 4$ contiguous, equal-mass segments (shaded regions), each of which is assigned to one new dust particle. Here, the vertical axis shows the differential mass density $a^3 \times \partial n/\partial a$. Alternatively, setting $N_d = 1$ would create one dust particle covering the full grain-size distribution, an approach used in Section 5.

total dust mass is the sum of dust masses contributed by individual chemical elements, and these dust elemental yields are a function of a star's mass and metallicity. Dust yields for AGB stars (Zhukovska et al. 2008; Ventura et al. 2012; Nanni et al. 2013; Schneider et al. 2014), SNe II (Todini & Ferrara 2001; Bianchi & Schneider 2007; Nozawa et al. 2007, 2010; Gall, Hjorth & Andersen 2011; Temim & Dwek 2013; Gall et al. 2014; Marassi et al. 2015), and SNe Ia (Nozawa et al. 2011) have been studied in detail. Dust formation can also be characterized in terms of condensation efficiency, the fraction of metals returned that exist in solid dust grains, with the remainder of metals occupying the gas phase. Below, we outline the dust yields that we adopt in calculating dust mass return from stellar populations.

For AGB stars, we interpolate the results from Schneider et al. (2014), which predicts dust yields for stars in the mass range of $1-8\,\rm M_\odot$ and metallicity range of $0.001 \le Z \le 0.008$. These yields are calculated for four grain types: carbon, silicate, SiC, and iron. We use these yields to determine the yields on an element-by-element basis for C, O, Mg, Si, and Fe, which are tracked in our dust model. Paralleling Zhukovska & Henning (2013), we assume that silicate grains are 50 per cent Mg_2SiO_4 , 30 per cent $MgSiO_3$, and 20 per cent Fe_2SiO_4 to set the element-by-element dust mass return and thus condensation efficiencies.

For SNe II, we adopt dust yields from Nozawa et al. (2010), which presents the mass of dust formed for each of the elements tracked in our model (C, O, Mg, Si, and Fe) in the core-collapse of a SN IIb with mass $18\,\mathrm{M}_{\odot}$ and metallicity Z=0.02. We assume that these results hold for core-collapse SNe of all types, noting that the condensation efficiency of this SN IIb is similar to that predicted for SNe IIP (Nozawa et al. 2003, 2010). Because Nozawa et al. (2010) models only one SN IIb, we assume that the mass of dust formed from a core-collapse SN scales linearly with progenitor mass. Future work could explore more detailed models of SN dust condensation as a function of different progenitor masses (e.g. Bianchi & Schneider 2007; Nozawa et al. 2007).

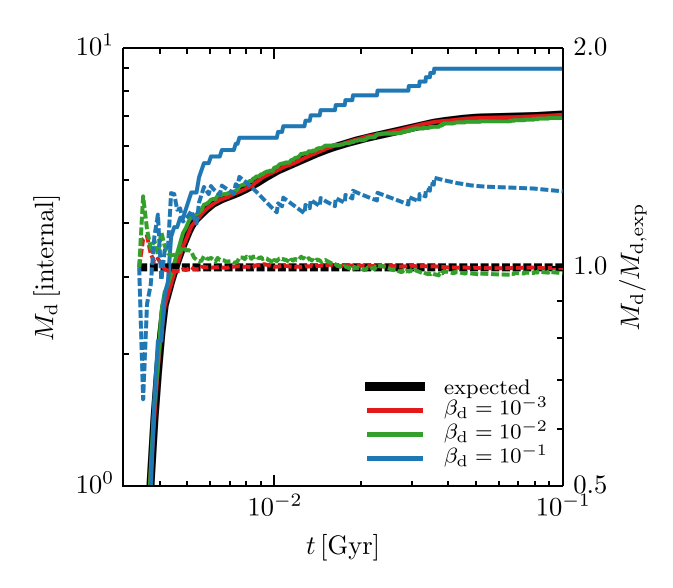


Figure 18. Cumulative mass of dust stochastically produced by a group of star particles born at t=0 Gyr. Solid coloured lines show dust mass as a function of time (left axis) for three choices of β_d , the ratio between a spawned dust particle's mass and the initial mass of a star particle. The solid black line marks the cumulative amount of dust expected to form using the dust yields, equivalent to the limit $\beta_d \to 0$. Dashed lines show the ratios between the simulated dust mass profiles and the expected dust mass profile (right axis). Smaller values of β_d lead to less stochastic behaviour, at the expense of spawning more dust particles.

For SNe Ia, we assume that the condensation efficiency of individual elements is the same as for SNe II, noting that dust grains produced by SNe Ia share a similar elemental distribution as dust grains formed in core-collapse SNe (Nozawa et al. 2011). However, because SNe Ia form fewer metals than SNe II in a stellar population and are not thought to be major contributors of dust formation (Nozawa et al. 2011), the choice of SNe Ia condensation efficiencies does not strongly impact our results.

While there may be stochastic deviations from these dust yields as individual dust particles are spawned, our procedure gives the correct IMF-averaged dust yields in expectation. As discussed at the start of Section 3, when a dust particle is spawned, we compute the fraction of its total mass given by individual chemical elements. These fractions are then updated when the dust particle accretes mass from or returns mass to the ISM according to the procedure outlined in Section 3.2.

Fig. 18 demonstrates the stochastic formation of dust for a group of 512 star particles, all assumed to be born at t = 0 Gyr with solar metallicity and subject to a Chabrier (2003) IMF over the mass range of $0.1-100 \,\mathrm{M}_{\odot}$. For the purposes of this test, dust particles are not subject to any grain-size evolution in the ISM and thus do not gain or lose mass after creation. We compare the expected mass of dust that would be obtained by continually enriching surrounding gas with the mass of dust obtained via the stochastic spawning of dust particles. We vary the parameter β_d , the ratio between a dust particle's mass and a star particle's initial mass. As β_d decreases, the mass of stochastically spawned dust particles more closely follows the expected dust mass. However, this improved accuracy comes at the expense of needing to spawn more, lower-mass dust particles compared to larger values of β_d . The optimal value of β_d for a particular simulation should be determined by balancing the need for accurate dust mass return with the need for computational efficiency.

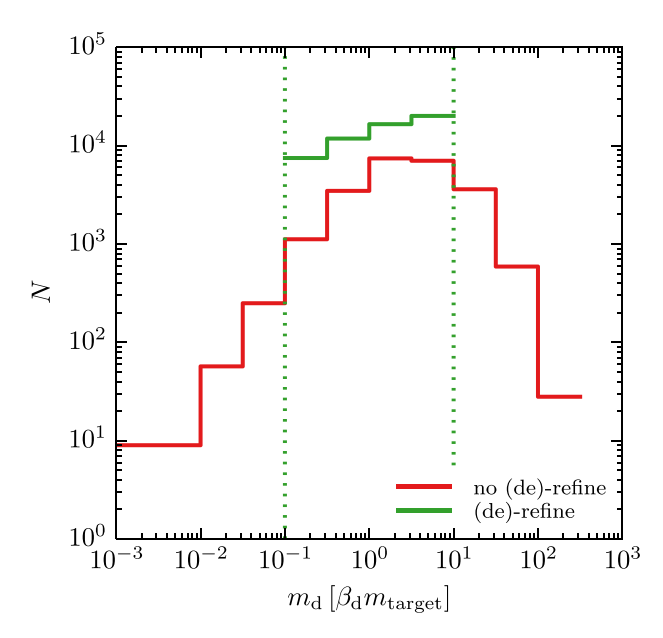


Figure 19. Number of dust particles as a function of dust mass at t = 1.5 Gyr for the isolated disc galaxy presented in Section 5. Distributions are shown for the medium resolution full physics run with (de)-refinement (green) and a run without (de)-refinement (red). Dust masses are shown in units of β_d m_{target} , where $\beta_d = 0.1$ and m_{target} is the fixed target gas cell mass. Vertical dotted lines show the minimum and maximum dust particle masses allowed by the (de)-refinement scheme. Without (de)-refinement, the distribution of dust particle masses develops tails at low and high mass.

4.4 Dust refinement and de-refinement

In some circumstances, it may be desirable to constrain the mass of individual dust particles. For example, a dust particle that undergoes rapid accretion may become much more massive than dust particles newly spawned from stars, while a dust particle in hot gas could see a significant fraction of its mass thermally sputtered. Here, we outline algorithms that can be used to reduce the spread in dust particle masses.

Large dust particles can be refined by splitting them in two whenever their mass exceeds some threshold value $m_{\rm d}^{\rm max}$. While the grain-size distribution can be divided between these two new particles in various ways, it is simplest to divide it equally so that each new particle has half of the number of grains and slope in every bin. The two new dust particles are displaced in opposite directions from the old dust particle's position along a randomly chosen axis by a distance of 0.025h, where h is the smoothing length enclosing neighbouring gas cells computed via equation (10). The new particles keep the same dust velocity so that momentum is conserved. This procedure has no communication overhead but increases the dust particle count, adding computational cost.

De-refinement of dust particles works in a similar way. If the mass of a dust particle falls below $m_{\rm d}^{\rm min}$, we search for its nearest dust particle neighbour with mass above $m_{\rm d}^{\rm min}$. A new dust particle with mass equal to sum of the two particles' masses is placed at the centre of mass, given a new velocity to conserve momentum, and assigned a grain-size distribution obtained by adding the particles' individual distributions. In principle, the neighbour lookup could require communication between processors.

We implement these schemes for dust refinement and derefinement in AREPO, ensuring no significant variation among dust particle masses. Fig. 19 shows the dust particle mass distributions that arise at t = 1.5 Gyr in the medium-resolution isolated galaxy

simulations detailed in Section 5. We contrast runs with and without (de)-refinement. Both runs employ $\beta_d = 0.1$, meaning dust particles are created with mass one-tenth of their star particle's initial mass. Initial star particle masses are close to $m_{\rm target}$, the mean gas cell mass adopted as a target mass when (de)-refining gas cells (Vogelsberger et al. 2012). The isolated galaxy run with dust (de)-refinement limits dust particle masses to be between $m_{\rm d}^{\rm min} = 0.01 \, m_{\rm target}$ and $m_{\rm d}^{\rm max} = m_{\rm target}$. However, in the run without (de)-refinement some dust particles reach masses more than an order of magnitude beyond these mass limits. In this run, the tails in the dust particle mass distribution become wider with time and are undesirable.

4.5 Dust-dust neighbour searches

When dust particles search for neighbouring gas cells, smoothing lengths enclose a weighted number of gas cells (e.g. see equation 10). However, we also need to perform searches for neighbouring dust particles: dust density estimates are needed for shattering and coagulation. Because dust particle masses can vary more strongly than gas cell masses, even with dust (de)-refinement turned on, we calculate dust-dust smoothing lengths by enclosing a desired amount of dust mass rather than a desired number of neighbours. This avoids circumstances where a dust particle with many low-mass dust neighbours calculates a small smoothing length and estimates a dust density despite little dust mass enclosed in the kernel.

To be precise, we iteratively solve for dust–dust smoothing lengths by forcing the kernel to enclose total dust mass in the range $(64\pm16)\times(\beta_{\rm d}m_{\rm target})$, where $\beta_{\rm d}m_{\rm target}$ is the typical mass of dust particles when produced by stars and $\beta_{\rm d}=0.1$ is our fiducial value. Using this smoothing length, we then perform dust density estimates with the usual kernel-weighting scheme (see equation 12).

When de-refinement is active, we also require the smoothing length to enclose a dust neighbour with mass above $m_{\rm d}^{\rm min}$, the minimum allowable dust mass. This way, a dust particle in need of de-refinement can follow the procedures in Section 4.4 and be derefined into its high-mass neighbour. If necessary, we temporarily allow the kernel's enclosed dust mass to exceed the upper bound in the previous paragraph in order to find a high-mass dust neighbour.

5 ISOLATED DISC GALAXY SIMULATIONS

As a first application of our dust model, we simulate the formation and dust content of an isolated disc galaxy.

5.1 Initial conditions

The initial matter distribution consists of slowly rotating gas superimposed on a collisionless dark matter halo following a Hernquist (1990) profile. Initially, the halo has a mass of $10^{12} \,\mathrm{M}_{\odot}$ with a 10 per cent gas fraction. We set the dimensionless spin parameter to $\lambda = 0.05$ with a concentration c = 6. To start, the number of gas cells and dark matter particles is 8×10^6 for each component and 16×10^6 in total. We run this test with cooling and star formation, but without any feedback processes. The grain-size evolution calculations are performed using the piecewise linear discretization with N = 16 bins covering the size range from $a_{\min} = 0.001 \,\mu\text{m}$ to $a_{\text{max}} = 1 \,\mu\text{m}$. Dust particles are stochastically created with mass equal to 10 per cent of a star particle's initial mass (i.e. $\beta_d = 0.1$), refined when the particle mass exceeds the target gas cell mass (i.e. $m_{\rm d}^{\rm max}=m_{\rm target}$), and de-refined when the particle mass is less than 1 per cent of the target gas cell mass (i.e. $m_d^{\min} = 0.01 m_{\text{target}}$). In this test, we only create $N_d = 1$ dust particle per spawn event and do not sub-divide the grain-size distribution across multiple particles. For the grain-size evolution time-step constraint detailed in Section 3.8, we adopt $\chi=0.1$. We perform grain-size evolution updates using the sub-cycling parameter $\lambda=2$, meaning that dust particle dynamical time-steps are only required to resolve twice the grain-size evolution time-step.

We study the evolution of this isolated disc galaxy using three dust models, each adding progressively more grain-size physics as summarized in Table 1. The first, 'production only,' creates dust particles using the stochastic prescription from Section 4 but does not include any grain-size evolution (i.e. a dust particle's grain-size distribution is set upon creation and is fixed). The second, 'no shattering/coagulation,' includes dust production and also allows grains to undergo number-conserving size evolution processes like accretion (Section 3.3), thermal sputtering (Section 3.4), and SN destruction (Section 3.5). Finally, the 'full physics' model adds shattering (Section 3.6) and coagulation (Section 3.7). This latter model thus includes all of the grain-size physics detailed in Section 3.

In all of these models, dust is dynamically coupled to the gas through the drag force detailed in Section 2. However, typical drag stopping time-scales (e.g. equation 14) are short compared to the simulation duration, and dust and gas are not significantly decoupled. The results we present below are largely unchanged in the limit where stopping time-scale $t_s \rightarrow 0$ and drag acts instantaneously to set a dust particle's velocity equal to the local gas velocity. However, dust and gas may be more decoupled in future galaxy simulations including feedback or when studying smaller portions of the ISM.

Furthermore, to improve the performance of our code, we simplify the integral in equation (58) used during shattering and coagulation to determine the total cross-section for collisions between grains in two different bins. We ignore grain-size distribution bin slopes when calculating $I^{k,j}(t)$ (i.e. we assume that $s_k(t) = s_j(t) = 0$) and instead only use the numbers of grains $N_k(t)$ and $N_j(t)$ in the bins. This reduces considerably the number of floating-point operations needed to evaluate these integrals, and we have verified that in this isolated galaxy application this change has no significant effect on our results.

5.2 Predicted dust population

Fig. 20 shows the time evolution of the full physics model, presenting face-on and edge-on projections of dust surface density, dust-to-gas ratio, and dust-to-metal ratio. We note that numerical convergence properties of the dust model across different resolutions are discussed in Appendix B. The panels illustrate the formation of a disc galaxy whose dust mass increases with time. The dust surface density shows a clear radial gradient, with a peak central value at t = 1.5 Gyr of roughly 10^9 M_{\odot} kpc⁻². It is important to note that we use no stellar feedback, and so no winds are driven from the disc that could reduce star formation (and in turn dust formation) or produce dust outflows. Thus, our dust surface densities should not be compared to observations of Milky Way-like systems. Similarly, dust-to-gas ratios decrease with radius from the galactic centre but lie above the approximate 10^{-2} value associated with the Milky Way (Draine et al. 2007).

The absence of feedback strongly affects the normalization in dust-to-gas and dust-to-metal ratios, since gas is overconsumed and dust is overproduced. The dust-to-metal ratio is defined as the ratio of dust mass to total (dust plus gas-phase) metal mass and is near unity for this run without feedback. In our current model, dust particles are not removed when nearby gas cells stochastically

convert to star particles. As a result, star formation in our model reduces the supply of ISM gas-phase metals but not dust. However, the depletion of dust via star formation, known as astration, is not the only physical process that can reduce ISM dust mass. In Appendix C, we compare the time-scales for astration and the destruction of dust in SN shocks, two processes that scale with dust-to-gas ratio and star formation rate. Dust loss via astration is expected to be sub-dominant compared with SN destruction. In our full physics model that includes SN dust destruction, the dust-to-metal ratio only changes by a few per cent when incorporating an estimate of the astration rate. The dust content of the production only run is more strongly affected when we include a model for astration, producing a dust mass and dust-to-metal ratio lower by about a factor of 4 at t = 1 Gyr. However, we argue in Appendix C that the production only run with an astration model is not physically realistic: it includes astration but neglects the SN dust destruction process that is expected to dominate dust mass-loss in the ISM. Furthermore, it neglects the ability for dust grains to gain mass and offset the effects of astration and SN dust destruction. Although astration is expected to be sub-dominant to other dust destruction processes, we plan to directly model this process in future work.

To assess the impact of grain-size evolution, Fig. 21 shows the dust surface density, dust-to-gas ratio, and dust-to-metal ratio in the isolated disc galaxy at t=1 Gyr using the different dust physics models listed in Table 1. In all three models, dust surface density, dust-to-gas ratio, and dust-to-metal ratio decrease as a function of radial distance from the disc centre. However, the no shattering/coagulation and full physics runs show higher dust surface density, dust-to-gas ratio, and dust-to-metal ratio than the production only run, which lacks grain-size evolution. Overall, the results in Fig. 21 suggest that accretion increases dust mass more quickly than sputtering and SN destruction decrease dust mass. We note that the normalization in dust-to-metal ratio is strongly affected by the lack of feedback and overconsumption of gas (and gas-phase metals) into stars.

Fig. 22 shows the time evolution of dust and stellar mass using the three grain-size evolution models. Because the presence of dust affects gas dynamics and star formation only slightly, we display the stellar mass evolution for just one model. Stellar mass increases rapidly at early times – reaching roughly $10^{10}\,\mathrm{M}_{\odot}$ after about 200 Myr – before slowing. As suggested by the visuals in Fig. 21, the three grain-size models show similar qualitative behaviour, characterized by a sharp rise in dust mass over the first half Gyr.

The production-only model with no grain-size evolution is easiest to understand. In this model, dust particle masses never change, and dust mass closely traces stellar mass, albeit with a lower normalization owing to an effective dust yield for mass return from stars. The no shattering/coagulation model with accretion, thermal sputtering, and SN destruction produces about three times as much dust as in the production-only run. The amount of dust gained by allowing grains to grow and accrete gas-phase metals thus exceeds the amount of dust destroyed by thermal sputtering and SN shocks. This trend is likely to persist in runs with feedback, given that reduced star formation rates will lead to reduced SN destruction.

The final, full physics model variation increases the dust mass by about 50 per cent at t=1.5 Gyr compared to the no shattering/coagulation run. As we show later in Fig. 23, the presence of the shattering process in the full physics model efficiently shifts grains to smaller sizes. Thus, by shattering big grains, this model increases the total grain surface area. Since the grain growth mechanism in Section 3.3 specifies a form of da/dt dependent on gas quantities

2876 R. McKinnon et al.

Table 1. Description of the grain-size physics included in the three dust models used in isolated galaxy simulations. Each model adds successively more physics: the 'production only' run solely produces dust particles and includes no grain-size evolution, the 'no shattering/coagulation' run includes all number-conserving processes, and the 'full physics' run includes both number-conserving and mass-conserving processes.

Name	Grain-size physics
Production only No shattering/coagulation Full physics	No grain-size evolution Grain growth, thermal sputtering, SN shock-driven destruction Grain growth, thermal sputtering, SN shock-driven destruction, shattering, coagulation

but independent of grain size *a*, the radii of grains of different sizes end up growing at the same rate. As a result, a population of small grains gains mass more quickly than a population of large grains with the same total mass. Because stars tend to produce large grains (see Section 4.2), grains in the no shattering/coagulation model do not gain mass as quickly as in the full physics model with shattering.

While the various models predict similar total dust mass evolution, they differ in how this mass is distributed among grains. Although dust particles spawned by stars have grain-size distributions initialized in the same manner, these models have different components evolving the grain-size distribution. Fig. 23 shows the total grain-size distribution predicted for the isolated galaxy under these three models at t=1 Gyr, obtained by summing over all dust particles. We multiply this grain-size distribution $(\partial n/\partial a)$ by the mass of a grain of size a in order to compare the mass contributed by grains of different sizes. The two models without shattering and coagulation are most similar: switching from the production only model lacking grain-size evolution to the no shattering/coagulation model including grain growth shifts grains to larger sizes, producing an increase in mass contained in grains with size $a \gtrsim 0.4 \, \mu m$.

The full physics model is qualitatively different from the two previous models. The inclusion of shattering shifts grains to smaller sizes, strongly enhancing the amount of mass in grains with $a \lesssim 0.03~\mu m$. Thus, although the dust models predict similar total dust masses in Fig. 22, the distribution of this mass into various size grains significantly differs. We caution that the absence of feedback in these runs leads to an overproduction of dust, and inflated dust densities could shatter grains more rapidly than expected (see equation 55). We note that the grain size at which the distribution starts to rise is set implicitly by our model due to the shattering velocity scale.

Figs. 22 and 23 focused on galaxy-integrated dust-mass and grain-size distribution, but we can also study predictions of our dust models locally within the galaxy. Radial profiles of dust surface density and dust-to-gas ratio for the three different dust models at t = 1 Gyr are shown in Fig. 24. The full physics model, which produced the most amount of dust overall, shows the highest dust surface density at essentially all radii. However, all three runs show similar profiles: a relatively constant surface density near the galactic centre and a rapid fall off at larger radii.

In the left-hand panel of Fig. 25, we show the median grain size as a function of radial distance for the three dust models at t=1 Gyr. We assign dust particles to a series of two-dimensional radial bins, sum the total grain-size distribution within each radial bin, and then use these size distributions to compute median grain sizes as well as 32nd and 68th percentiles. In the production-only run lacking grain-size evolution, dust particles' grain-size distributions are frozen in time. As a result, the median grain size for this run shows essentially no radial variation. The profile is not exactly flat because dust particles created by AGB stars and SNe II have different initial grain-size distributions, and so not every individual

dust particle has the same median grain size. The runs with grainsize evolution show more variation than the production-only run.

Both the no shattering/coagulation and full physics runs show a decline in median grain size with radius. Fig. 22 illustrates that these runs increase total dust mass above the production-only run lacking grain-size physics. For the no shattering/coagulation run, this suggests that accretion, which increases dust mass, dominates thermal sputtering and SN-based destruction, which reduce dust mass. The radial-size profile for this no shattering/coagulation run in Fig. 25 is consistent with a strong accretion mechanism: since accretion is strongest in regions of high gas density and metallicity (see equation 49), we expect grain sizes to be highest near the galactic centre. While the median grain size in the no shattering/coagulation run decreases by one order of magnitude out to 2 kpc, from roughly $0.1 \,\mu\mathrm{m}$ to $0.01 \,\mu\mathrm{m}$, the full physics model shows a shallower decline. Median grain sizes in the full physics model are lower overall and decrease from about $0.004 \,\mu\mathrm{m}$ to $0.002 \,\mu\mathrm{m}$ over this same region. Grain sizes in the full physics run are subject to a wider variety of processes: for example, both accretion and coagulation are expected to affect how grains grow (Hirashita 2012). However, even these simple radial size profiles, which smooth over angular variations within the disc, suggest that median grain sizes are not uniform in the galaxy.

For more detail, the right panel of Fig. 25 shows the grain-size distribution in the full physics model at 1 Gyr in three, kpc-wide radial intervals about the galactic centre. There are two main trends to note. First, the relative abundance of small grains ($a \lesssim 0.01 \, \mu \text{m}$) to large grains ($a \gtrsim 0.1 \, \mu \text{m}$) decreases with radius. This is intuitive, since the abundance of small grains likely results from shattering, and shattering is strongest at low radii, where densities are highest. Secondly, among the population of small grains – which dominate the overall grain count – the peak in the mass-size distribution in Fig. 25 shifts slightly to smaller sizes with larger radial distance. This is similar to the negative slope seen in the left-hand panel of Fig. 25 and is possibly a consequence of small grains accreting mass from gas more quickly near the galactic centre, pushing small grain radii somewhat higher. However, coagulation can also play a role in shifting central grains to larger sizes (e.g. Hirashita 2012).

We expect the overall cycle between shattering and accretion to proceed as follows. Regions of high-gas and dust-density shatter grains more quickly (increasing the ratio of small to large grains), but these small grains then grow in size more quickly (increasing the median size for small grains and overall dust mass). This cycle continues itself over time, and so dust in the central region of the galaxy changes more rapidly than in the outskirts.

Tracking the grain-size distribution locally within the galaxy also allows us to generate mock extinction curves, with grains of different sizes along a line-of-sight contributing different opacities. We refer the reader to Appendix D for the full details of how these extinction curves are constructed. Here, we note that, in addition to dust particles' grain-size distributions, these extinction curves depend on parameters like the extinction efficiency $Q_{\text{ext}}(a,\lambda)$, the

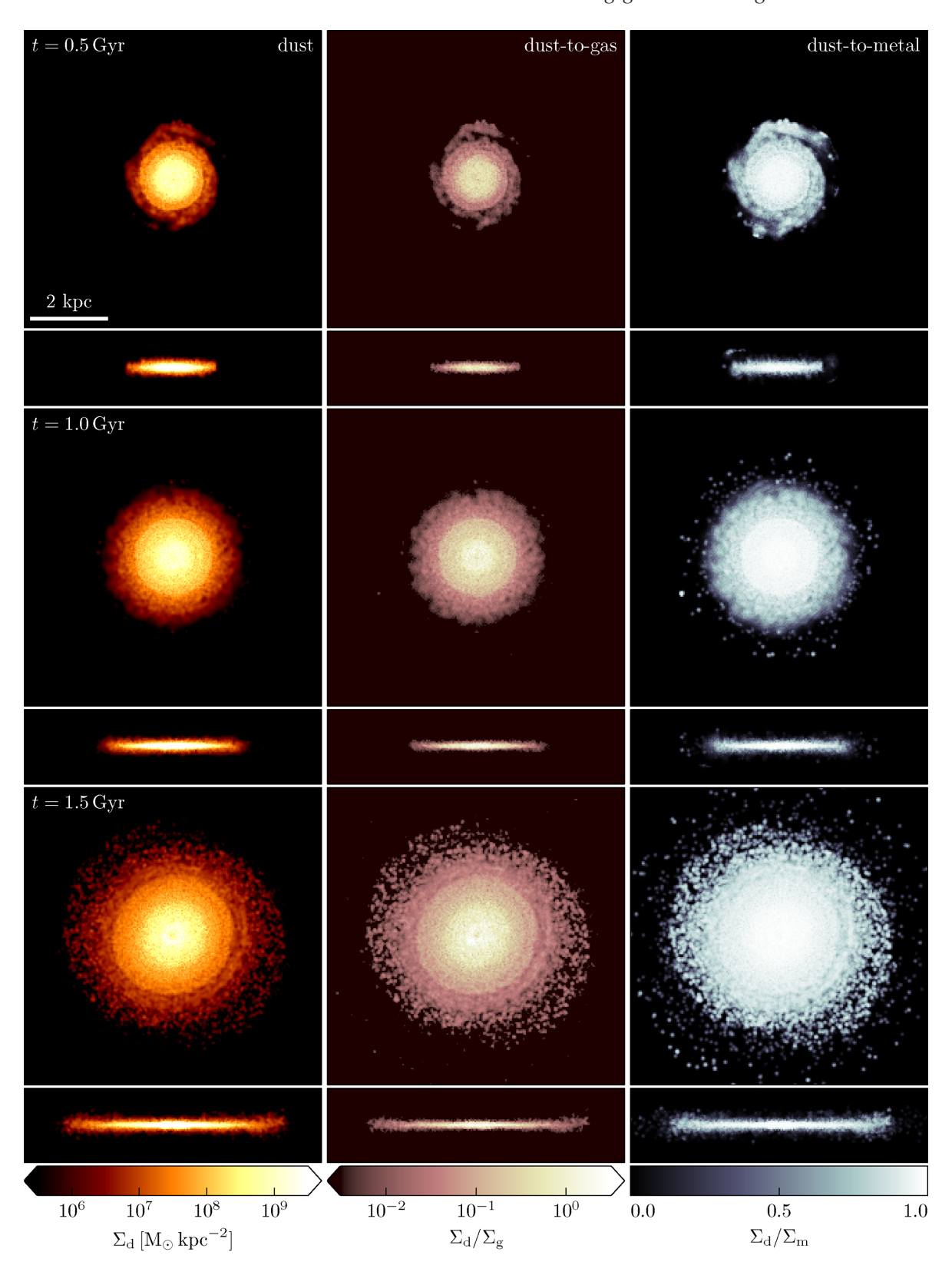


Figure 20. Evolution of face-on and edge-on projected dust surface density (left), dust-to-gas ratio (centre), and dust-to-metal ratio (right) for the full grain physics run at t = 0.5, 1, and 1.5 Gyr. Dust surface density, dust-to-gas ratio, and dust-to-metal ratio decrease with radius. This simulation lacks feedback, overconsuming gas and overproducing dust.

dimensionless ratio of extinction cross-section to geometric cross-section for grains of size a at wavelength λ . The dust-mass opacity

at wavelength λ , $\kappa_{\rm ext}(a,\lambda)$, can also be written in terms of the extinction efficiency via $\kappa_{\rm ext}(a,\lambda) = 3Q_{\rm ext}(a,\lambda)/(4a\rho_{\rm gr})$. In this work,

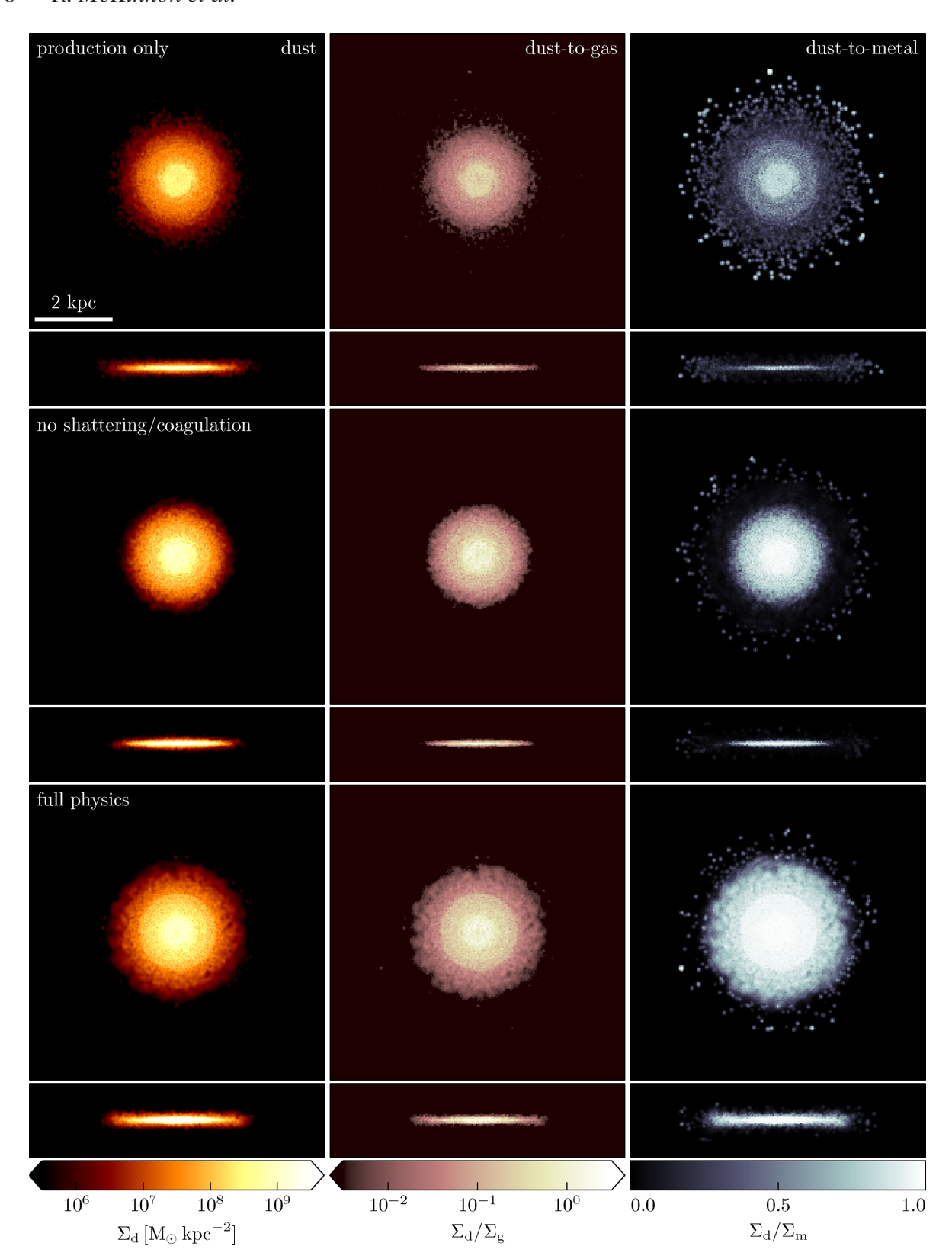


Figure 21. Projections of dust surface density (left), dust-to-gas ratio (centre), and dust-to-metal ratio (right) at t = 1 Gyr for three grain physics models: the run with only dust production and no grain-size evolution (top), the model with all number-conserving grain processes (accretion, sputtering, and SN destruction) but lacking shattering and coagulation (middle), and the full physics model (bottom).

we use tabulated grain extinction efficiencies from Draine & Lee (1984) and Laor & Draine (1993). These papers present separate

extinction efficiencies for silicate and graphite grains, $Q_{\rm ext}^{\rm sil}(a,\lambda)$ and $Q_{\rm ext}^{\rm gra}(a,\lambda)$, respectively, which can be converted into dust-mass

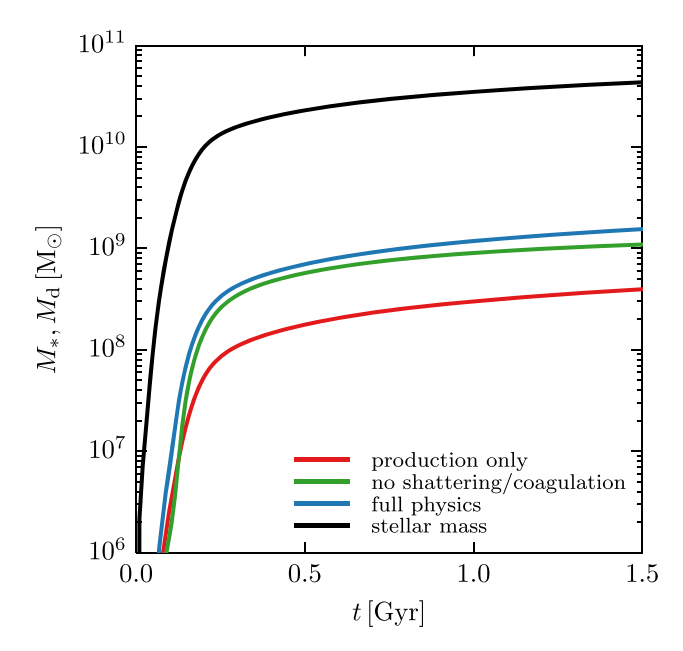


Figure 22. Time evolution of the isolated galaxy's dust mass, computed for models with various dust physics (coloured lines). Stellar mass evolution is nearly identical across these dust model variations and for readability, we plot the stellar mass from only one of these runs (black line). Dust mass is shown for the model with dust production but without grain-size evolution (red), the model including solely number-conserving grain processes like accretion, thermal sputtering, and SN destruction (green), and the full grain physics model including shattering and coagulation (blue). The full physics model produces the largest dust mass.

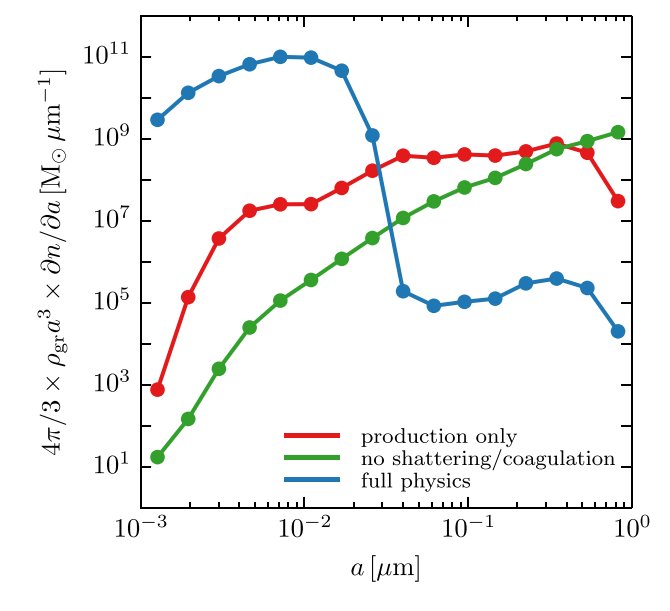


Figure 23. Distribution of dust mass among grains of different sizes predicted for the isolated galaxy at t=1 Gyr by the same models presented in Fig. 22. The grain-size distribution $(\partial n/\partial a)$, with units of inverse length) is summed over all dust particles in the galaxy, and the vertical axis plots this total grain-size distribution weighted by the masses of grains of different sizes. Integrating these profiles gives the total dust masses predicted for the galaxy. The model with shattering is qualitatively different, shifting dust mass to smaller grain sizes, although its total dust mass from Fig. 22 is similar to those of the other models.

opacities $\kappa_{\rm ext}^{\rm sil}$ and $\kappa_{\rm ext}^{\rm gra}$. To calculate extinction curves, we compute an effective dust-mass opacity using the following approximation. Letting $f_{\rm gra}$ be the fraction of total dust mass in the isolated galaxy contributed by carbon, the effective dust-mass opacity is estimated as $\kappa_{\rm ext}(a,\lambda)=f_{\rm gra}\kappa_{\rm ext}^{\rm gra}(a,\lambda)+(1-f_{\rm gra})\kappa_{\rm ext}^{\rm sil}(a,\lambda)$. This dust-mass opacity is what enters into extinction curve calculations via equation (D4).

Fig. 26 presents a synthetic extinction curve at t=1 Gyr for each dust model. Curves are shown over the full wavelength range for which there are tabulated extinction efficiencies $(10^{-3} \, \mu \text{m} \leq \lambda \leq 10^3 \, \mu \text{m})$ and over the UV and optical region $(0.1 \mu \text{m} \leq \lambda \leq 1 \, \mu \text{m})$, plotted in terms of inverse wavelength as is customary). Extinction is computed using a line of sight directed towards the galactic centre from a point 5 kpc above and 5 kpc radially outside the disc. We compare with the observed Galactic extinction curve from Fitzpatrick & Massa (2007), as compiled by Hou et al. (2017).

All three dust models predict qualitatively similar extinction curves for $\lambda\gtrsim 10~\mu m$, wavelengths that are much larger than typical grain sizes. In this far-IR regime, extinction falls off according to a $A(\lambda) \varpropto \lambda^{-2}$ power law. At shorter wavelengths, the production-only and no shattering/coagulation runs lacking shattering and containing larger grains yield qualitatively different extinction than the full physics model. For example, extinction for the production-only and no shattering/coagulation models – which from Fig. 23 predict much of the total dust exists in large grains – is nearly flat for $\lambda\lesssim 1~\mu m$. In particular, there is essentially no change in extinction from the optical to the UV, as observed in the Galaxy.

The full physics model, on the other hand, contains many more small grains and so predicts more features in the extinction curve at small wavelength, like a 2175 Å bump. Extinction peaks in the UV near $\lambda\approx 0.1~\mu m$, and the full physics run predicts more than an order of magnitude more UV extinction than the production-only and no shattering/coagulation runs with large grains. The full physics model does show an increase in steepness from optical to UV, albeit one that rises more steeply than observed in the Galaxy. This steepness is likely influenced by the lack of feedback, since the overproduction of dust leads to high dust densities and thus overly rapid shattering. An excess of small grains could exacerbate the rise in UV extinction, motivating future work with this dust model coupled to feedback methods.

5.3 Comparison to other models

We can compare the predictions for our isolated disc galaxy with several other works that model grain dynamics or size evolution.

For example, recently Aoyama et al. (2017) performed SPH simulations of an isolated galaxy with total mass $1.3 \times 10^{12} \,\mathrm{M}_{\odot}$, where dust evolution calculations take place on each gas particle using a simplified two-size grain distribution (i.e. grains are classified as either small, roughly 0.005 μm, or large, roughly 0.1μm). Because there are no separate dust particles, this model implicitly assumes dust and gas are perfectly coupled and omits a drag force. At t = 1 Gyr, Aoyama et al. (2017) predict that the mass surface density of small grains is highest in the galactic centre, a result also suggested by the right-hand panel of Fig. 25. In contrast, the two models disagree about whether most dust mass at t = 1 Gyr is locked in small or large grains: Aoyama et al. (2017) find that the total mass ratio of small to large grains is roughly 0.2, while our results in Fig. 23 suggest this ratio is well above unity. However, Aoyama et al. (2017) include a model for thermal stellar feedback, which suppresses the dust mass in their galaxy compared to ours.

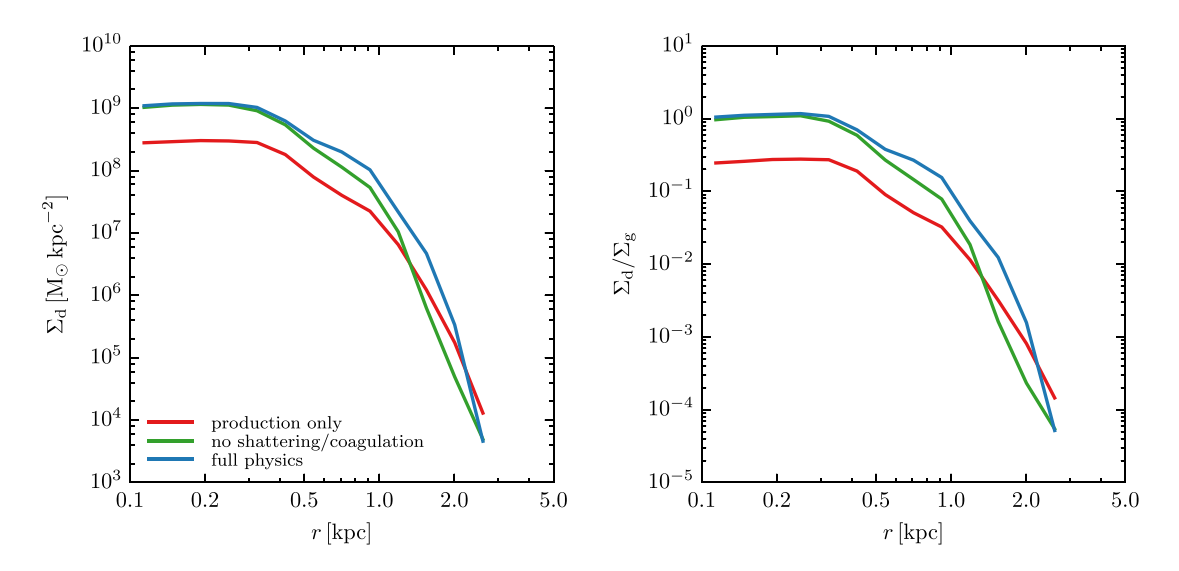


Figure 24. Profiles of dust surface density (left) and dust-to-gas ratio (right) as a function of two-dimensional radial distance from the spin axis at t = 1 Gyr for the runs shown in Fig. 21.

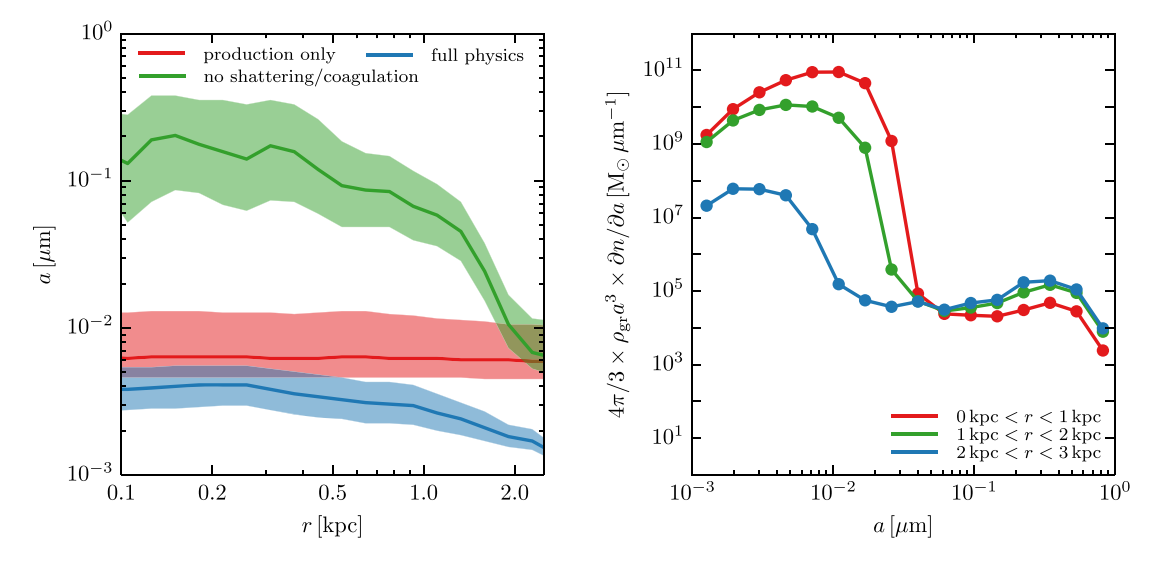


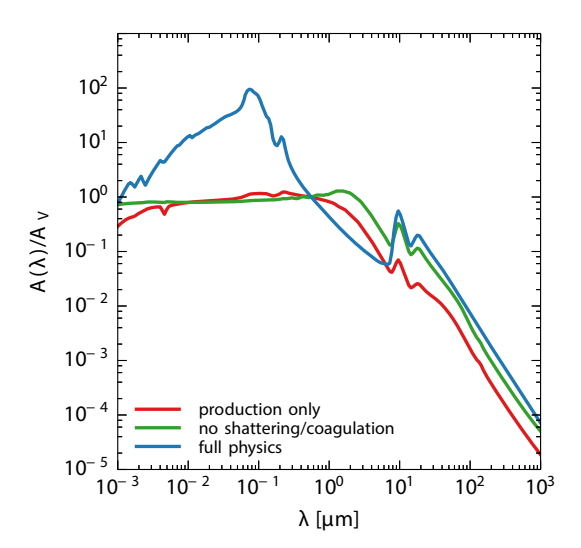
Figure 25. Left-hand panel: grain size versus two-dimensional radial distance for the three dust models at t = 1 Gyr. Solid lines show median grain size, while shaded regions extend to 32nd and 68th percentiles. In each radial bin, these statistics are calculated using the total grain-size distribution obtained by summing over size distributions for constituent dust particles. Right-hand panel: grain-size distribution of dust in different radial slices at t = 1 Gyr in the full physics model. The prefactor multiplying the grain-size distribution $(\partial n/\partial a)$ means that integrating these profiles yields the total dust mass in each radial slice.

This lowers their dust surface densities, in turn slowing the rate of shattering. In the future, a fairer comparison of small-to-large grain mass ratio requires us to couple our dust model to a feedback implementation.

The two-size grain approximation used in Aoyama et al. (2017) has been extended by Hou et al. (2017) to account for carbonaceous and silicate dust grains. This is necessary to predict galactic extinction curves, since carbonaceous and silicate grains have different extinction cross-sections. Reddening caused by different grain species can be important not only for extinction in galaxies but also in the circumgalactic medium (Hirashita & Lin 2018). In Hou et al. (2017), the relative abundance of small-to-large grains increases with time and grows most rapidly in the central region of the galaxy. At t=1 Gyr, the right-hand panel of Fig. 25 also predicts this small-to-large abundance ratio to peak in the galactic centre. The presence of small grains creates more pronounced extinction

curve features, like the 2175 Å bump and the UV slope. The lack of feedback and abundance of small grains in our runs yields a full physics extinction curve in Fig. 26 that rises more quickly from the optical to the UV than observed. However, Hou et al. (2017) demonstrate that at t=1 Gyr this UV slope is correlated with the small-to-large abundance ratio: regions in the galaxy with decreased small-to-large abundance ratio also see decreased the UV slope. A lower rate of shattering in our model would produce fewer small grains and a slope in the UV more in line with observations.

Separately, the two-size grain approximation has also been applied in one-zone models of galaxy evolution, which lack spatial resolution and instead solve for galaxy-integrated quantities (Hirashita 2015; Hou et al. 2016). Other one-zone models evolve the full grain-size distribution, which is more computationally expensive but tracks the range of sizes grains may have (Hirashita & Yan 2009; Asano et al. 2013b). For example, Asano et al. (2013b) run



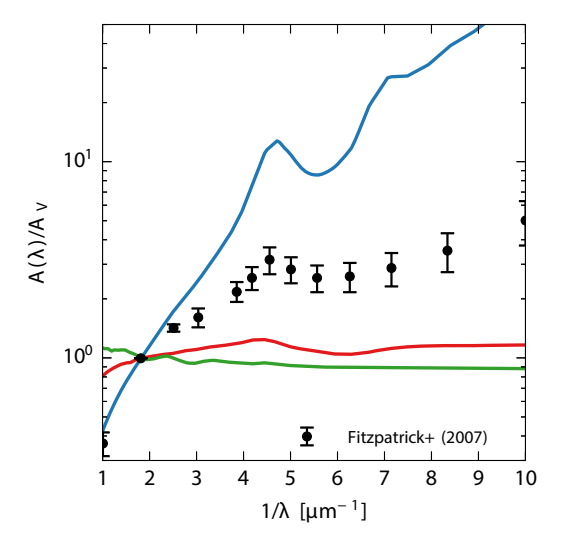


Figure 26. Predicted extinction as a function of wavelength at t = 1 Gyr for the dust models from Figs 22 and 23. Extinction curves are shown for the full wavelength range $10^{-3} \mu m \le \lambda \le 10^3 \mu m$ (left) and for the zoomed in the range of $0.1 \mu m \le \lambda \le 1 \mu m$ (right), with the latter plotted in terms of inverse wavelength. Extinction is calculated along a line-of-sight pointing to the centre of the galaxy from 5 kpc above and 5 kpc radially outside and is normalized by extinction in the V band, A_V . The full dust physics run is the only one to show a 2175 Å bump and a rise in extinction in the UV. Observations of the Galactic extinction curves are shown in black (Fitzpatrick & Massa 2007).

their one-zone model with and without shattering, finding that at $t=1\,\mathrm{Gyr}$, the inclusion of shattering increases the abundance of grains with $a\lesssim 0.01\,\mathrm{\mu m}$ by orders of magnitude. The grain-size distributions at $t=0.1\,\mathrm{and}\,1\,\mathrm{Gyr}$ are unaffected by the inclusion of coagulation. Only at much larger times ($t\approx 10\,\mathrm{Gyr}$) does coagulation materially affect the grain-size distribution, shifting grain mass to larger sizes. However, even at late times the effect of shattering is more significant than that of coagulation. These predictions from Asano et al. (2013b) parallel our grain-size distribution findings in Fig. 23, that at $t=1\,\mathrm{Gyr}$ shattering is more efficient than coagulation and that the galaxy-wide grain-size distribution forms many more small grains than stars produce.

Another class of model has been developed by Bekki (2015), coupling dust particles to gas in SPH simulations through a drag law but neglecting grain-size evolution. All dust grains share the same fixed size (roughly $0.1\mu m$), limiting the ability to construct extinction curves that capture the range of grain sizes that exist in the ISM. However, these dust particles are coupled to a scheme modelling radiation pressure from stellar sources, and simulations in Bekki (2015) predict that radiation pressure can increase the vertical extent of dust in the disc while reducing radial gradients in the dust distribution. As we work to couple our dust dynamics and size evolution model to more forces like radiation pressure, we will be in position to test these dynamical predictions and additionally investigate their impact on the grain-size distribution and extinction.

6 CONCLUSIONS

We have implemented a novel scheme to track the dynamical motion and grain-size evolution of interstellar dust grains in the movingmesh code AREPO.

Simulation dust particles represent ensembles of grains of different sizes and are characterized by individual grain-size distributions that are evolved in time. Each grain-size distribution is discretized using a piecewise linear method and updated according to a variety of physical processes. Processes like accretion, sputtering, and destruction from supernova shocks conserve grain number but shift

mass between dust and gas phases, while dust-dust collisional processes like shattering and coagulation conserve total grain mass but not grain number. We demonstrate that the piecewise linear discretization is second-order accurate in the number of grain-size bins. The dynamical drag force for each particle is calculated based on its internal grain-size distribution to couple gas and dust motions.

The drag force implementation is based on a second-order semiimplicit scheme that makes use of analytic properties of the drag force and alleviates the need for small time-steps when dust and gas are strongly coupled; i.e. when the stopping time-scale governing drag is short. The drag force acting on dust grains depends on local gas properties, and our methods benefit from the accurate treatment of hydrodynamics in AREPO. For example, in simulating gas and dust dynamics in a Sod shock tube test, dust particle velocities do not suffer from spurious post-shock velocity ringing seen in some SPH methods.

The actual production of dust particles is coupled to the stellar evolution scheme of our galaxy formation model. We implement dust mass return during stellar evolution using a stochastic procedure that probabilistically spawns dust particles from star particles. When spawning new dust particles, we adopt dust elemental yields according to theoretical models of mass return from AGB stars and SNe. Similarly, initial grain-size distributions for dust particles are set according to theoretical predictions for grain populations formed during stellar evolution. Newly created dust particles are then subjected to the aforementioned physical processes shaping their grain-size distributions.

Processes like shattering, coagulation, sputtering, and dust growth can lead to rather significant changes in the number of dust particles and their masses. This can lead, for example, to very heavy dust particles or many low-mass particles, which is computationally disadvantageous. We have therefore also implemented refinement and de-refinement schemes for dust particles, to keep the mass distribution of dust particles within predefined limits. Furthermore, we have also implemented time-step sub-cycling for the dust time-steps to avoid too many small dust-dominated time-steps. While our model currently neglects astration, the consumption of

ISM dust during star formation, we use a time-scale argument to show that SN destruction of dust is expected to dominate astration as a sink of ISM dust mass.

To demonstrate the simultaneous application of dust dynamics, grain-size evolution, and dust particle creation, we simulate an isolated disc galaxy with cooling and star formation but no feedback and study the relative strengths of various grain-size processes. For example, a model without grain-size evolution and a model with full grain-size physics produce galactic dust masses differing by a factor of four and qualitatively very different grain-size distributions. The inclusion of shattering is particularly efficient at shifting large dust grains to smaller sizes. Using the simulated spatial distribution of grains, we produce sample extinction curves, with small grains in the full physics run producing an increase in extinction towards the UV.

Our framework for simulating dust and gas mixtures can readily be extended to account for other dynamical processes relevant in galaxy formation, like magnetohydrodynamics, radiation pressure, and thermochemical processes. Ultimately, our model represents a step towards a more comprehensive treatment of dust dynamics and grain-size evolution in galaxy formation.

ACKNOWLEDGEMENTS

Our anonymous referee provided valuable feedback that helped improve this manuscript. We thank Hiroyuki Hirashita for providing us with the tabulated form of grain velocities calculated over an extended grain-size range and used in Hirashita & Yan (2009). We also thank Takaya Nozawa for making available the tabulated versions of the SN grain-size distributions presented in Nozawa et al. (2007) and the SN dust destruction efficiencies used in Asano et al. (2013b). Finally, we are grateful to Volker Springel for sharing access to AREPO.

The simulations were performed on the joint MIT-Harvard computing cluster supported by MKI and FAS. RM acknowledges support from the DOE CSGF under grant number DE-FG02-97ER25308. MV acknowledges support through an MIT RSC award and the support of the Alfred P. Sloan Foundation. PT acknowledges support from NASA through Hubble Fellowship grant *HST*-HF2-51341.001-A awarded by STScI, which is operated under contract NAS5-26555. RK acknowledges support from NASA through Einstein Postdoctoral Fellowship grant number PF7-180163 awarded by the *Chandra* X-ray Center, which is operated by the Smithsonian Astrophysical Observatory for NASA under contract NAS8-03060.

REFERENCES

Agertz O., Kravtsov A. V., 2015, ApJ, 804, 18

Aoyama S., Hou K.-C., Shimizu I., Hirashita H., Todoroki K., Choi J.-H., Nagamine K., 2017, MNRAS, 466, 105

Aoyama S., Hou K.-C., Hirashita H., Nagamine K., Shimizu I., 2018, preprint (arXiv:1802.04027)

Asano R. S., Takeuchi T. T., Hirashita H., Inoue A. K., 2013a, Earth, Planets, and Space, 65, 213

Asano R. S., Takeuchi T. T., Hirashita H., Nozawa T., 2013b, MNRAS, 432, 637

Baines M. J., Williams I. P., Asebiomo A. S., 1965, MNRAS, 130, 63

Bakes E. L. O., Tielens A. G. G. M., 1994, ApJ, 427, 822

Balsara D. S., Tilley D. A., Rettig T., Brittain S. D., 2009, MNRAS, 397, 24

Barlow M. J., 1978, MNRAS, 183, 367

Barranco J. A., 2009, ApJ, 691, 907

Bekki K., 2015, MNRAS, 449, 1625

Bianchi S., Schneider R., 2007, MNRAS, 378, 973

Bocchio M., Marassi S., Schneider R., Bianchi S., Limongi M., Chieffi A., 2016, A&A, 587, A157

Booth R. A., Clarke C. J., 2016, MNRAS, 458, 2676

Booth R. A., Sijacki D., Clarke C. J., 2015, MNRAS, 452, 3932

Burke J. R., Silk J., 1974, ApJ, 190, 1

Cazaux S., Tielens A. G. G. M., 2004, ApJ, 604, 222

Chaabouni H., Bergeron H., Baouche S., Dulieu F., Matar E., Congiu E., Gavilan L., Lemaire J. L., 2012, A&A, 538, A128

Chabrier G., 2003, PASP, 115, 763

Chen L.-H., Hirashita H., Hou K.-C., Aoyama S., Shimizu I., Nagamine K., 2018, MNRAS, 474, 1545

Chokshi A., Tielens A. G. G. M., Hollenbach D., 1993, ApJ, 407, 806

Corbelli E. et al., 2012, A&A, 542, A32

Cortese L. et al., 2012, A&A, 540, A52

Costa T., Rosdahl J., Sijacki D., Haehnelt M. G., 2018, MNRAS, 473, 4197 Cuzzi J. N., Hogan R. C., 2003, Icarus, 164, 127

Cuzzi J. N., Dobrovolskis A. R., Champney J. M., 1993, Icarus, 106, 102

de Bennassuti M., Schneider R., Valiante R., Salvadori S., 2014, MNRAS, 445, 3039

De Rossi M. E., Bower R. G., Font A. S., Schaye J., Theuns T., 2017, MNRAS, 472, 3354

Dominik C., Tielens A. G. G. M., 1997, ApJ, 480, 647

Draine B. T., 1990, in Blitz L., ed., ASP Conf. Ser. Vol. 12, The Evolution of the Interstellar Medium, Astron. Soc. Pac., San Francisco, p. 193

Draine B. T., 2003, ARA&A, 41, 241

Draine B. T., Fraisse A. A., 2009, ApJ, 696, 1

Draine B. T., Lee H. M., 1984, ApJ, 285, 89

Draine B. T., Salpeter E. E., 1979, ApJ, 231, 77

Draine B. T., Sutin B., 1987, ApJ, 320, 803

Draine B. T. et al., 2007, ApJ, 663, 866

Dubovskii P. B., Galkin V. A., Stewart I. W., 1992, J. Phys. A: Math. Gen., 25, 4737

Dwek E., 1998, ApJ, 501, 643

Dwek E., Arendt R. G., 1992, ARA&A, 30, 11

Dwek E. et al., 2008, ApJ, 676, 1029

Epstein P. S., 1924, Phys. Rev., 23, 710

Ferrara A., Ferrini F., Barsella B., Franco J., 1991, ApJ, 381, 137

Ferrarotti A. S., Gail H.-P., 2006, A&A, 447, 553

Feuerbacher B., Willis R. F., Fitton B., 1973, ApJ, 181, 101

Filbet F., Laurençot P., 2004, SIAM J. Sci. Comput., 25, 2004

Fitzpatrick E. L., Massa D., 2007, ApJ, 663, 320

Fournier N., Laurençot P., 2005, Commun. Math. Phys., 256, 589

Gall C., Hjorth J., Andersen A. C., 2011, A&AR, 19, 43

Gall C. et al., 2014, Nature, 511, 326

Goodson M. D., Luebbers I., Heitsch F., Frazer C. C., 2016, MNRAS, 462, 2777

Grassi T., Krstic P., Merlin E., Buonomo U., Piovan L., Chiosi C., 2011, A&A, 533, A123

Hernquist L., 1990, ApJ, 356, 359

Hirashita H., 2010, MNRAS, 407, L49

Hirashita H., 2012, MNRAS, 422, 1263

Hirashita H., 2015, MNRAS, 447, 2937

Hirashita H., Kuo T.-M., 2011, MNRAS, 416, 1340

Hirashita H., Li Z.-Y., 2013, MNRAS, 434, L70

Hirashita H., Lin C.-Y., 2018, preprint (arXiv:1804.00848)

Hirashita H., Voshchinnikov N. V., 2014, MNRAS, 437, 1636

Hirashita H., Yan H., 2009, MNRAS, 394, 1061

Hirashita H., Nozawa T., Villaume A., Srinivasan S., 2015, MNRAS, 454, 1620

Hjorth J., Gall C., Michałowski M. J., 2014, ApJ, 782, L23

Hollenbach D., Salpeter E. E., 1971, ApJ, 163, 155

Hopkins P. F., Lee H., 2016, MNRAS, 456, 4174

Hopkins P. F., Kereš D., Oñorbe J., Faucher-Giguère C.-A., Quataert E., Murray N., Bullock J. S., 2014, MNRAS, 445, 581

Hou K.-C., Hirashita H., Michałowski M. J., 2016, PASJ, 68, 94

Hou K.-C., Hirashita H., Nagamine K., Aoyama S., Shimizu I., 2017, MNRAS, 469, 870

```
Hutchison M. A., Price D. J., Laibe G., 2018, MNRAS, 476, 2186
```

Ishibashi W., Fabian A. C., 2015, MNRAS, 451, 93

Johansen A., Klahr H., Henning T., 2006, ApJ, 636, 1121

Jones A. P., Tielens A. G. G. M., Hollenbach D. J., 1996, ApJ, 469, 740

Khandai N., Di Matteo T., Croft R., Wilkins S., Feng Y., Tucker E., DeGraf C., Liu M.-S., 2015, MNRAS, 450, 1349

Kozasa T., Nozawa T., Tominaga N., Umeda H., Maeda K., Nomoto K., 2009, in Henning T., Grün E., Steinacker J., eds, ASP Conf. Ser.: Cosmic Dust – Near and Far, Astron. Soc. Pac., San Francisco, Vol. 414, p. 43

Krivitsky D. S., 1995, J. Phys. A: Math. Gen., 28, 2025

Kwok S., 1975, ApJ, 198, 583

Laibe G., Price D. J., 2011, MNRAS, 418, 1491

Laibe G., Price D. J., 2012a, MNRAS, 420, 2345

Laibe G., Price D. J., 2012b, MNRAS, 420, 2365

Laibe G., Price D. J., 2014a, MNRAS, 444, 1940

Laibe G., Price D. J., 2014b, MNRAS, 440, 2136

Laibe G., Price D. J., 2014c, MNRAS, 440, 2147

Landau L. D., Lifshitz E. M., 1959, Fluid Mech., Pergamon Press, Oxford

Laor A., Draine B. T., 1993, ApJ, 402, 441

Laporte N. et al., 2017, ApJ, 837, L21

Lazarian A., Yan H., 2002, ApJ, 566, L105

Lee M. H., 2001, J. Phys. A: Math. Gen., 34, 10219

Lee H., Hopkins P. F., Squire J., 2017, MNRAS, 469, 3532

Leitch-Devlin M. A., Williams D. A., 1985, MNRAS, 213, 295

Liffman K., Clayton D. D., 1989, ApJ, 340, 853

Lloyd S., 1982, IEEE Trans. Inf. Theor., 28, 129

Lorén-Aguilar P., Bate M. R., 2014, MNRAS, 443, 927

Lorén-Aguilar P., Bate M. R., 2015, MNRAS, 454, 4114

Marassi S., Schneider R., Limongi M., Chieffi A., Bocchio M., Bianchi S., 2015. MNRAS, 454, 4250

Markiewicz W. J., Mizuno H., Voelk H. J., 1991, A&A, 242, 286

Mathews W. G., Brighenti F., 1999, ApJ, 526, 114

Mathis J. S., 1990, ARA&A, 28, 37

Mathis J. S., 1998, ApJ, 497, 824

Mathis J. S., Rumpl W., Nordsieck K. H., 1977, ApJ, 217, 425

Mattsson L., 2016, Planet. Space Sci., 133, 107

McGee S. L., Balogh M. L., 2010, MNRAS, 405, 2069

McKee C., 1989, in Allamandola L. J., Tielens A. G. G. M., eds., Proc. IAU Symp., Kluwer Academic Publishers, Dordrecht, Vol. 135. p. 431

McKinnon R., Torrey P., Vogelsberger M., 2016, MNRAS, 457, 3775

McKinnon R., Torrey P., Vogelsberger M., Hayward C. C., Marinacci F., 2017, MNRAS, 468, 1505

Michałowski M. J., Murphy E. J., Hjorth J., Watson D., Gall C., Dunlop J. S., 2010, A&A, 522, A15

Miniati F., 2010, J. Comput. Phys., 229, 3916

Monaghan J. J., 1997, J. Comput. Phys., 138, 801

Monaghan J. J., Kocharyan A., 1995, Comput. Phys. Commun., 87, 225

Murray N., Quataert E., Thompson T. A., 2005, ApJ, 618, 569

Nanni A., Bressan A., Marigo P., Girardi L., 2013, MNRAS, 434, 2390

Nath B. B., Laskar T., Shull J. M., 2008, ApJ, 682, 1055

Novak G. S., Ostriker J. P., Ciotti L., 2012, MNRAS, 427, 2734

Nozawa T., Kozasa T., Umeda H., Maeda K., Nomoto K., 2003, ApJ, 598, 785

Nozawa T., Kozasa T., Habe A., 2006, ApJ, 648, 435

Nozawa T., Kozasa T., Habe A., Dwek E., Umeda H., Tominaga N., Maeda K., Nomoto K., 2007, ApJ, 666, 955

Nozawa T., Kozasa T., Tominaga N., Maeda K., Umeda H., Nomoto K., Krause O., 2010, ApJ, 713, 356

Nozawa T., Maeda K., Kozasa T., Tanaka M., Nomoto K., Umeda H., 2011, ApJ, 736, 45

O'Donnell J. E., Mathis J. S., 1997, ApJ, 479, 806

Ormel C. W., Cuzzi J. N., 2007, A&A, 466, 413

Ormel C. W., Paszun D., Dominik C., Tielens A. G. G. M., 2009, A&A, 502, 845

Ostriker J., Silk J., 1973, ApJ, 184, L113

Paardekooper S.-J., Mellema G., 2006, A&A, 453, 1129

Paruta P., Hendrix T., Keppens R., 2016, Astron. Computi., 16, 155

Pilbratt G. L. et al., 2010, A&A, 518, L1

Planck Collaboration et al., 2014, A&A, 571, A11

Popping G., Somerville R. S., Galametz M., 2017, MNRAS, 471, 3152

Price D. J., Laibe G., 2015, MNRAS, 451, 813

Price D. J. et al., 2017, preprint (arXiv:1702.03930)

Rémy-Ruyer A. et al., 2014, A&A, 563, A31

Rosdahl J., Schaye J., Teyssier R., Agertz O., 2015, MNRAS, 451, 34

Roškar R., Teyssier R., Agertz O., Wetzstein M., Moore B., 2014, MNRAS, 444, 2837

Saito T., 2002, J. Comput. Phys., 176, 129

Saito T., Marumoto M., Takayama K., 2003, Shock Waves, 13, 299

Schaye J. et al., 2015, MNRAS, 446, 521

Schneider R., Valiante R., Ventura P., dell'Agli F., Di Criscienzo M., Hirashita H., Kemper F., 2014, MNRAS, 442, 1440

Sedov L. I., 1959, Similarity and Dimensional Methods in Mechanics, Academic Press, New York

Silvia D. W., Smith B. D., Shull J. M., 2010, ApJ, 715, 1575

Silvia D. W., Smith B. D., Shull J. M., 2012, ApJ, 748, 12

Skibba R. A. et al., 2011, ApJ, 738, 89

Smoluchowski M. V., 1916, Z. Phys., 17, 557

Sod G. A., 1978, J. Comput. Phys., 27, 1

Springel V., 2010, MNRAS, 401, 791

Springel V., Hernquist L., 2003, MNRAS, 339, 289

Stepinski T. F., Valageas P., 1996, A&A, 309, 301

Temim T., Dwek E., 2013, ApJ, 774, 8

Thompson T. A., Fabian A. C., Quataert E., Murray N., 2015, MNRAS, 449, 147

Tielens A. G. G. M., 2005, The Physics and Chemistry of the Interstellar Medium, Cambridge University Press, Cambridge

Todini P., Ferrara A., 2001, MNRAS, 325, 726

Torrey P., Cox T. J., Kewley L., Hernquist L., 2012, ApJ, 746, 108

Torrey P. et al., 2018, MNRAS, 477, L16

Torrey P. et al., 2017, preprint (arXiv:1711.05261)

Tricco T. S., Price D. J., Laibe G., 2017, MNRAS, 471, L52

Tsai J. C., Mathews W. G., 1995, ApJ, 448, 84

Ventura P. et al., 2012, MNRAS, 420, 1442

Vigil R. D., Ziff R. M., 1989, J. Colloid Interface Sci., 133, 257 Voelk H. J., Jones F. C., Morfill G. E., Roeser S., 1980, A&A, 85, 316

Vogelsberger M., Sijacki D., Kereš D., Springel V., Hernquist L., 2012,

MNRAS, 425, 3024 Vogelsberger M., Genel S., Sijacki D., Torrey P., Springel V., Hernquist L.,

Vogelsberger M., Genel S., Sijacki D., Torrey P., Springel V., Hernquist L., 2013, MNRAS, 436, 3031

Vogelsberger M. et al., 2014a, Nature, 509, 177

Vogelsberger M. et al., 2014b, MNRAS, 444, 1518

Vogelsberger M. et al., 2018, MNRAS, 474, 2073

Watson D., Christensen L., Knudsen K. K., Richard J., Gallazzi A., Michałowski M. J., 2015, Nature, 519, 327

Weidenschilling S. J., 1977, MNRAS, 180, 57

Weingartner J. C., Draine B. T., 2001a, ApJ, 548, 296

Weingartner J. C., Draine B. T., 2001b, ApJS, 134, 263

Yahil A., Ostriker J. P., 1973, ApJ, 185, 787

Yamasawa D., Habe A., Kozasa T., Nozawa T., Hirashita H., Umeda H., Nomoto K., 2011, ApJ, 735, 44

Yan H., Lazarian A., Draine B. T., 2004, ApJ, 616, 895

Yasuda Y., Kozasa T., 2012, ApJ, 745, 159

Zahid H. J., Torrey P., Kudritzki R. P., Kewley L. J., Davé R., Geller M. J., 2013, MNRAS, 436, 1852

Zhukovska S., Henning T., 2013, A&A, 555, A99

Zhukovska S., Gail H.-P., Trieloff M., 2008, A&A, 479, 453

Zhukovska S., Dobbs C., Jenkins E. B., Klessen R. S., 2016, ApJ, 831, 147

APPENDIX A: DISCRETIZATION OF SHATTERING INTEGRALS

This section converts the analytic shattering framework presented in Section 3.6 into one capable of handling a piecewise linear grain-size distribution. Namely, we show how equation (57) can be derived from equation (55).

To start, multiply equation (55) by V_d^2 , apply equation (54) to convert mass densities into number densities, and rewrite integrals using the partition of $[a_{\min}, a_{\max}]$, so that

$$V_{d} \frac{d}{dt} \left[m(a) \frac{\partial n(a,t)}{\partial a} da \right] = -m(a)^{2} \frac{\partial n(a,t)}{\partial a} da \sum_{k=0}^{N-1} \int_{a_{k}^{c}}^{a_{k+1}^{c}} \alpha(a,a_{1}) m(a_{1}) \frac{\partial n(a_{1},t)}{\partial a_{1}} da_{1}$$

$$+ \frac{1}{2} \sum_{k=0}^{N-1} \sum_{j=0}^{N-1} da \int_{a_{k}^{c}}^{a_{k+1}^{c}} \int_{a_{j}^{c}}^{a_{j+1}^{c}} \alpha(a_{1},a_{2}) m(a_{1}) m(a_{2}) \frac{\partial n(a_{1},t)}{\partial a_{1}} \frac{\partial n(a_{2},t)}{\partial a_{2}} m_{\text{shat}}(a,a_{1},a_{2}) da_{2} da_{1}.$$
(A1)

Integrating a over the interval $[a_i^e, a_{i+1}^e]$ and substituting in the piecewise linear grain-size distribution from equation (31), we find that the mass of grains in bin i, M_i , evolves as

$$V_{d} \frac{dM_{i}}{dt} = \int_{a_{i}^{c}}^{a_{i+1}^{c}} -m(a)^{2} \left(\frac{N_{i}(t)}{a_{i+1}^{e} - a_{i}^{e}} + s_{i}(t)(a - a_{i}^{c})\right) \sum_{k=0}^{N-1} \int_{a_{k}^{c}}^{a_{k+1}^{e}} \alpha(a, a_{1})m(a_{1}) \left(\frac{N_{k}(t)}{a_{k+1}^{e} - a_{k}^{e}} + s_{k}(t)(a_{1} - a_{k}^{c})\right) da_{1} da$$

$$+ \frac{1}{2} \int_{a_{i}^{e}}^{a_{i+1}^{e}} \sum_{k=0}^{N-1} \sum_{j=0}^{N-1} \int_{a_{k}^{e}}^{a_{k+1}^{e}} \int_{a_{j}^{e}}^{a_{j+1}^{e}} \left[\alpha(a_{1}, a_{2})m(a_{1})m(a_{2}) \left(\frac{N_{k}(t)}{a_{k+1}^{e} - a_{k}^{e}} + s_{k}(t)(a_{1} - a_{k}^{c})\right) \right] da_{1} da$$

$$\times \left(\frac{N_{j}(t)}{a_{j+1}^{e} - a_{j}^{e}} + s_{j}(t)(a_{2} - a_{j}^{c})\right) m_{\text{shat}}(a, a_{1}, a_{2}) da_{1} da. \tag{A2}$$

Substituting for α using equation (56) and rearranging, this can be simplified as

$$V_{d} \frac{dM_{i}}{dt} = \sum_{k=0}^{N-1} \int_{a_{i}^{c}}^{a_{i+1}^{c}} \int_{a_{k}^{c}}^{a_{k+1}^{c}} \left[-\pi(a+a_{1})^{2} v_{\text{rel}}(a, a_{1}) \mathbb{1}_{v_{\text{rel}} > v_{\text{shat}}}(a, a_{1}) m(a) \left(\frac{N_{i}(t)}{a_{i+1}^{c} - a_{i}^{c}} + s_{i}(t)(a - a_{i}^{c}) \right) \right] da_{1} da$$

$$\times \left(\frac{N_{k}(t)}{a_{k+1}^{c} - a_{k}^{c}} + s_{k}(t)(a_{1} - a_{k}^{c}) \right) da_{1} da$$

$$+ \frac{1}{2} \sum_{k=0}^{N-1} \sum_{j=0}^{N-1} \int_{a_{i}^{c}}^{a_{i+1}^{c}} \int_{a_{k}^{c}}^{a_{k+1}^{c}} \int_{a_{j}^{c}}^{a_{j+1}^{c}} \left[\pi(a_{1} + a_{2})^{2} v_{\text{rel}}(a_{1}, a_{2}) \mathbb{1}_{v_{\text{rel}} > v_{\text{shat}}}(a_{1}, a_{2}) \left(\frac{N_{k}(t)}{a_{k+1}^{c} - a_{k}^{c}} + s_{k}(t)(a_{1} - a_{k}^{c}) \right) da_{1} da$$

$$\times \left(\frac{N_{j}(t)}{a_{j+1}^{c} - a_{j}^{c}} + s_{j}(t)(a_{2} - a_{j}^{c}) \right) m_{\text{shat}}(a, a_{1}, a_{2}) da_{2} da_{1} da.$$
(A3)

Apart from the terms $v_{\text{rel}}(a_1, a_2)$ and $m_{\text{shat}}(a, a_1, a_2)$, equation (A3) only involves integrals of two-dimensional polynomials. We wish to evaluate this integral analytically so that we can explicitly update the mass in each bin using the piecewise linear grain-size distribution [i.e. the set of known $N_i(t)$ and $s_i(t)$ values]. We make two simplifying assumptions.

First, we assume that all grains in the same bin share the same speed. As a result, the relative velocity between two grains in bins k and j can be simplified as $v_{\rm rel}(a_1, a_2) \approx v_{\rm rel}(a_k^{\rm c}, a_j^{\rm c})$, independent of the integration variables a_1 and a_2 . Following Hirashita & Yan (2009) and Asano et al. (2013b), we adopt relative grain velocities from Yan et al. (2004), who calculated grain speeds as a function of grain size for various ISM phases, assuming a turbulent, magnetized fluid. Given our intent to use this dust model in cosmological simulations, we recognize that we will not resolve some of the phases studied by Yan et al. (2004), such as the DC1 and DC2 phases with T = 10 K and $n_{\rm H} = 10^4$ cm⁻³.

The current galaxy formation model in AREPO employs the Springel & Hernquist (2003) multiphase ISM model, which adopts a hybrid mixture of hot and cold components. We define the effective relative velocity $v_{\rm rel}^{\rm eff}(a_1,a_2) \equiv x v_{\rm rel}^{\rm CNM}(a_k^c,a_j^c) + (1-x)v_{\rm rel}^{\rm WIM}(a_k^c,a_j^c)$, where x is a kernel-smoothed estimate of the cold cloud mass fraction (see section 3 in Springel & Hernquist 2003) in neighbouring gas cells and $v_{\rm rel}^{\rm CNM}$ and $v_{\rm rel}^{\rm WIM}$ are the relative velocities computed for the CNM and WIM phases, respectively, using Yan et al. (2004). As we do not track detailed grain chemistry, the grain velocities for the CNM and WIM are averaged over the curves calculated in Yan et al. (2004) for silicate and graphite grains. This is a minor assumption, since the silicate and graphite curves are qualitatively similar. We use this form of $v_{\rm rel}^{\rm eff}$ in equation (A3). A more realistic ISM model would allow us to probe grain velocities in the variety of phases studied in Yan et al. (2004).

Secondly, we assume that the mass of grains produced with radius a by shattering grains of sizes a_1 and a_2 depends only on the bins involved in the collision. That is, for grains of sizes a_1 and a_2 in bins k and j, we adopt $m_{\text{shat}}(a, a_1, a_2) \approx m_{\text{shat}}(a, a_k^c, a_j^c)$. This assumption is reasonable given the physical uncertainties in grain–grain collisions, and the exact mass distribution of shattered grains is not expected to strongly affect shattering calculations (Jones et al. 1996; Hirashita & Yan 2009). Performing the second integral in equation (A3) over a, we express the mass of grains injected into bin i from a collision of grains with sizes a_k^c and a_j^c , the mid-points of bins k and j, as

$$m_{\text{shat}}^{k,j}(i) \equiv \int_{a^c}^{a_{i+1}^c} m_{\text{shat}}(a, a_k^c, a_j^c) \, \mathrm{d}a \approx \int_{a^c}^{a_{i+1}^c} m_{\text{shat}}(a, a_1, a_2) \, \mathrm{d}a.$$
 (A4)

In practice, we compute $m_{\rm shat}^{k,j}(i)$ by following the steps in section 2.3 of Hirashita & Yan (2009), which depend on $v_{\rm rel}(a_k^{\rm c},a_j^{\rm c})$. In dividing shattered grain mass among different bins, these calculations assume that shattered grains obey the new size distribution $\partial n/\partial a \propto a^{-3.3}$ (Jones et al. 1996).

Using these steps, we can approximate the integrals in equation (A3) and bring them to the form presented in equation (57).

APPENDIX B: CONVERGENCE STUDY OF ISOLATED DISC GALAXIES

We analyse the convergence properties of our full physics dust model using simulations at three different resolutions. In these runs, dark matter and gas each initially have 1.25×10^5 , 10^6 , and 8×10^6 resolution elements. Fig. B1 shows the isolated galaxy's total dust mass as a function of time as well as the galaxy-integrated grain-size distribution at 1 Gyr. The largest deviation in dust mass is at early times, with the highest resolution run producing dust more quickly than the other runs. However, this trend is largely being driven by the underlying star formation rate: the star formation rate increases slightly with resolution at fixed time. This translates into a small spread in dust mass in the early stages of the galaxy's formation, before grain-size processes have had much time to act. Beyond 1 Gyr, the dust mass profiles show improved convergence, and, by 1.5 Gyr, the dust masses differ by less than 0.1 dex across these resolutions. The grain-size distributions show similar qualitative features, with an abundance of small grains and a drop off in the mass contained in large grains. However, the radius at which the size distribution falls off does vary: the low resolution simulation predicts this feature at $a \approx 0.01 \, \mu m$, while the high-resolution run predicts $a \approx 0.03 \, \mu m$. The medium resolution run is more similar to the high-resolution one than the low-resolution one, suggesting the profiles are converging, but more simulations would be needed to fully investigate this.

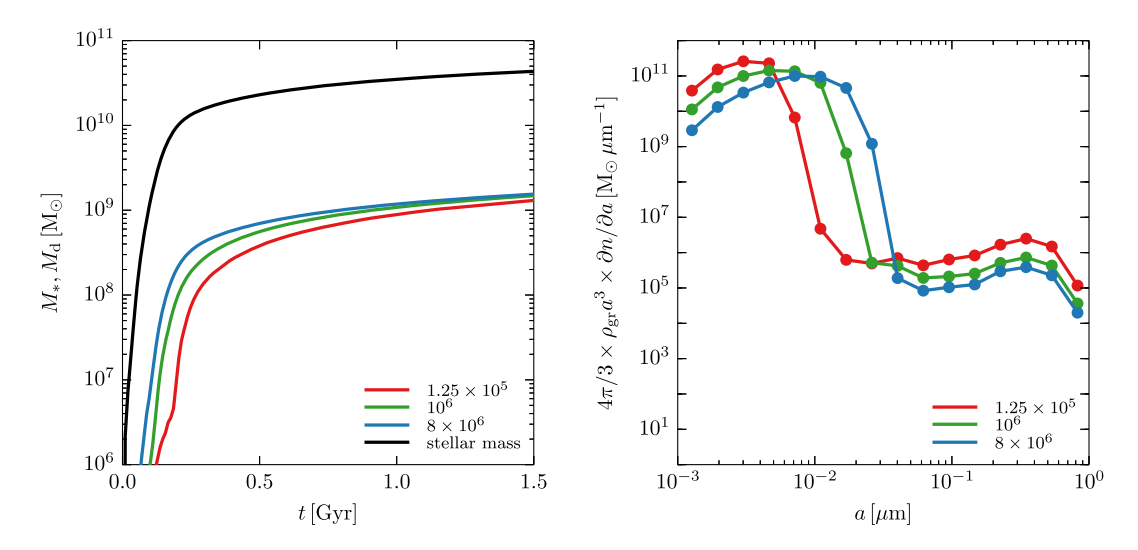


Figure B1. Properties of the full physics isolated disc galaxy simulated at three resolutions, with initial gas cell counts 1.25×10^5 (red), 10^6 (green), and 8×10^6 (blue). The left-hand panel shows total dust mass versus time, while the right-hand panel shows the total grain-size distribution at 1 Gyr, when the galaxy dust masses differ by about 0.1 dex. For comparison with the dust mass evolution, we also show the total stellar mass for the high-resolution simulation (black).

APPENDIX C: COMPARISON OF SN DESTRUCTION AND ASTRATION TIME-SCALES

Physically, dust in the ISM is depleted during star formation, a process known as astration. In our model used in Section 5, star particles form stochastically from gas cells, which contain gas and gas-phase metals. Notably, dust is not treated as a component of gas cells but instead using simulation particles. As a result, when gas cells convert to stars, the ISM supply of gas and gas-phase metals is reduced, but the supply of dust is unchanged. In this section, we quantify the expected rate of astration of dust and compare it to the rate at which dust is depleted through other means (e.g. SN destruction).

We can estimate the rate at which dust mass is lost due to astration following equation (3) in Hjorth, Gall & Michałowski (2014), giving $(dM_d/dt)_{astr} = -D \times dM_*/dt$, where M_d denotes dust mass in some region of the ISM, D is the local dust-to-gas ratio and dM_*/dt is the local star formation rate. This rate assumes that when stars form, dust and gas are depleted according to their relative abundance.

Similarly, the rate of dust destruction in SN shocks is estimated from equations 2 and 5 in McKee (1989) as $(dM_d/dt)_{dest} = -M_d/t_{SNR}$. Here, t_{SNR} is a time-scale given by the ratio of local ISM gas mass M_g to the rate at which gas mass is shocked by SNe, which depends on the local SN II rate R_{SN} . This time-scale is calculated using $1/t_{SNR} = \epsilon M_{cl} f_{SN} R_{SN}/M_g$. This expression relies on several parameters (with typical values estimated in sections 3 and 4 in McKee 1989): $\epsilon \approx 0.4$ denotes a grain destruction efficiency factor, $f_{SN} \approx 0.34$ reduces the nominal SN rate to account for inefficiencies in correlated SN blasts, and M_{cl} is the mass of gas shocked by an SN. This latter value is estimated by McKee (1989) as being in the range $M_{cl} \approx 2460-6800 \, M_{\odot}$. Since we are interested in whether astration can be important relative to SN destruction, we will assume $M_{cl} \approx 2460 \, M_{\odot}$. This places the SN shock time-scale t_{SNR} at the upper end of its expected range and adopts a weak rate of SN dust destruction. For our Chabrier (2003), IMF with mass range from 0.1 to $100 \, M_{\odot}$ and SN II cut-off at $6 \, M_{\odot}$, roughly 26.4 per cent

of stellar mass that forms exists as SNe II. Additionally, the average SN II mass is calculated as roughly $15.2 \,\mathrm{M}_{\odot}$. If we assume that SNe II immediately die after being formed, then we can estimate the SN II rate R_{SN} from the star-formation rate as

$$R_{\rm SN} pprox \left(\frac{0.264}{15.2 \,\mathrm{M}_\odot} \right) \frac{\mathrm{d}M_*}{\mathrm{d}t}.$$
 (C1)

Using all of these values and noting that M_d/M_g is the dust-to-gas ratio D, we can write the rate of dust loss due to SN destruction as a function of star-formation rate and in turn the expected astration rate via

$$\left(\frac{\mathrm{d}M_{\mathrm{d}}}{\mathrm{d}t}\right)_{\mathrm{dest}} \approx -5.8D\frac{\mathrm{d}M_{*}}{\mathrm{d}t} = 5.8\left(\frac{\mathrm{d}M_{\mathrm{d}}}{\mathrm{d}t}\right)_{\mathrm{astr}}.$$
 (C2)

That is, the rate of dust loss due to SN destruction is expected to be roughly five times greater than the rate of dust loss from astration.

To test whether dust mass-loss from astration is important, we rerun the isolated discs presented in Section 5 using the medium resolution initial conditions and a stronger SN destruction mechanism. Since both astration and SN dust destruction rates scale with the product of dust-to-gas ratio and star formation rate, we can use a larger SN destruction rate to indirectly model the effects of astration, which is not otherwise included in our simulations. To be precise, in these tests we calculate the SN destruction rate as usual and add an extra dust destruction rate equal to δ times the SN destruction rate to model astration. (In the production only model that does not include SN destruction of dust, we calculate what the SN destruction rate would be and use this to estimate the astration rate.) The calculations in equation (C2) suggest $\delta = 1/5.8 \approx 0.17$. Given that these physical time-scales have some uncertainty and our desire to assess the maximum impact astration could have, we actually employ $\delta = 0.25$. This can be considered an upper bound on the strength of astration relative to SN destruction.

We acknowledge that this prescription does not perfectly model astration, since dust destruction via SNe does not directly transfer metal mass from dust to newly formed stars but instead star-forming gas. Additionally, SNe dust destruction affects grain sizes by shifting them to smaller values. However, given that the factor by which SN dust destruction is enhanced is only 25 per cent and not a factor of several or more, this enhancement should not significantly affect grain-size distributions.

Using these tests, we can estimate the impact astration would have on dust content in our isolated discs. For the full physics model, the run without (with) astration predicts a t=1 Gyr dust mass of $1.1\times10^8\,\mathrm{M}_\odot$ ($1.1\times10^8\,\mathrm{M}_\odot$) and dust-to-metal ratio in the star-forming disc of 0.96 (0.93). In this model, astration is sub-dominant to SN dust destruction in shaping the overall dust mass and shifts the dust-to-metal ratio down by a few per cent. This is not surprising, given that the astration rate is several times lower than the SN destruction rate – and the fact that, overall, dust mass experiences a net increase in the ISM over time. The production only run lacking grain-size evolution does experience a stronger effect: without (with) astration, the t=1 Gyr dust mass and dust-to-metal ratio are $2.8\times10^8\,\mathrm{M}_\odot$ ($5.8\times10^7\,\mathrm{M}_\odot$) and 0.48 (0.14), respectively. However, we note that the production only run lacks SN destruction. While astration is sub-dominant to SN dust destruction, if the latter is not included, then astration can reduce dust masses and dust-to-metal ratios by roughly a factor of 4. This production-only set-up should not be taken as physically plausible: since SN dust destruction dominates astration, the former should be included in any model accounting for the latter. In our full physics model where SN destruction is already present, the addition of astration affects results less strongly than SN destruction. None the less, for completeness we intend to model astration directly in future work.

APPENDIX D: GENERATING EXTINCTION CURVES

The optical depth at wavelength λ contributed by grains with sizes in the interval [a, a + da] along a path \mathcal{P} is given by

$$\tau(a,\lambda) da = \int_{\mathcal{P}} \pi a^2 Q_{\text{ext}}(a,\lambda) n_{\text{d}}(\mathbf{r},a) da ds, \tag{D1}$$

where $n_d(\mathbf{r}, a) \times da$ is the number density of grains with sizes in [a, a + da] at position \mathbf{r} , calculated by interpolating over the grain-size distributions of nearby dust particles. The extinction efficiency $Q_{\text{ext}}(a, \lambda) = Q_{\text{abs}}(a, \lambda) + Q_{\text{sca}}(a, \lambda)$ is the ratio of extinction cross-section to geometric cross-section, πa^2 , and includes absorption and scattering contributions. Extinction efficiencies also vary depending on whether grains are assumed to be silicate or graphite. We adopt extinction efficiencies for silicate and graphite grains from Draine & Lee (1984) and Laor & Draine (1993), interpolating to our grain-size bins as necessary.

We can rewrite equation (D1) in terms of $\kappa_{\rm ext}(a,\lambda) = 3Q_{\rm ext}(a,\lambda)/(4a\rho_{\rm gr})$, the dust mass opacity at wavelength λ and grain size a. This produces

$$\tau(a,\lambda) da = \int_{\mathcal{P}} \frac{4\pi}{3} a^3 \rho_{\text{gr}} \kappa_{\text{ext}}(a,\lambda) n_{\text{d}}(\boldsymbol{r},a) da ds.$$
 (D2)

The magnitude of the extinction along this line of sight is then obtained by integrating over the grain-size distribution, yielding

$$A(\lambda) = 2.5 \log_{10}(e) \int_{a_{\min}}^{a_{\max}} \tau(a, \lambda) \, \mathrm{d}a = 2.5 \log_{10}(e) \frac{4\pi}{3} \rho_{\mathrm{gr}} \int_{a_{\min}}^{a_{\max}} a^3 \kappa_{\mathrm{ext}}(a, \lambda) \int_{\mathcal{P}} n_{\mathrm{d}}(\mathbf{r}, a) \, \mathrm{d}s \, \mathrm{d}a. \tag{D3}$$

If we break the grain-size integral into the sum of integrals over the N grain-size bins and approximate grain sizes with the mid-points of the N bins, we can discretize this as

$$A(\lambda) = 2.5 \log_{10}(e) \frac{4\pi}{3} \rho_{gr} \sum_{i=0}^{N-1} a_i^{c3} \kappa_{ext}(a_i^c, \lambda) (a_{i+1}^e - a_i^e) \int_{\mathcal{P}} n_{d}(\mathbf{r}, a_i^c) ds.$$
 (D4)

This paper has been typeset from a TFX/LATFX file prepared by the author.